Development of Integrative Optofluidic Laser Systems for Biological/Biochemical Applications

by

Qiushu Chen

A dissertation submitted in partial fulfillment
of the requirements for the degree of
Doctor of Philosophy
(Biomedical Engineering)
in the University of Michigan
2017

Doctoral Committee:
      Professor Xudong Fan, Chair
      Associate Professor Jianping Fu
      Professor L. Jay Guo
      Professor Shuichi Takayama
      Professor Nils G. Walter

Qiushu Chen

qschen@umich.edu

ORCID iD: 0000-0001-7650-932X

ACKNOWLEDGEMENTS

TABLE OF CONTENTS

LIST OF FIGURES

LIST OF TABLES

ABSTRACT

The optofluidic laser is an emerging technology that integrates the microcavity, microfluidic channel, and gain medium in liquid. Further integration with biomaterials results in the optofluidic biolaser, which can emit laser light with the modulation from biological/biochemical conditions. Due to the coherent and nonlinear nature of laser emission, optofluidic biolasers are promising in ultra-sensitive biological/biochemical detections. However, the practical significance of biolasers is still under debate and a large gap still exists in the literature in reference to their application in clinical settings.

This thesis outlines the development of integrative, optofluidic laser systems that incorporate biological/biochemical materials with different optical microcavity configurations, showing unique laser characteristics and revealing the potential for the use of lasers in practical biological/biochemical analyses.

First, optofluidic lasers utilizing Förster resonant energy transfer (FRET) were examined. Optofluidic FRET lasers that incorporated fluorescent proteins, DNA tetrahedra, and polymer-coated aqueous quantum dots in the liquid gain were experimentally demonstrated with capillary-based optofluidic ring resonators. Experiments show that the laser mechanism can provide up to 100-fold enhancement to the FRET signal and that molecular configurations and molecular interactions can significantly tune the laser performance through FRET. Highly sensitive, laser-based detection schemes for molecular interactions and novel bio-controlled lasers are, thus, promising.

Second, optofluidic lasers with a single molecular layer of gain were obtained. Through surface functionalization, gain molecules were concentrated at the solid-liquid interface of a ring resonator to form a single molecular layer. A pure laser signal was generated free of fluorescence background. This scheme significantly lowers the analyte concentration required for laser operation and is an analog to surface-based fluorescence detection technologies, pointing to a new direction for laser-based analyses.

Finally, integrative optofluidic laser systems that included biological cells as an active component were studied. A FRET laser was investigated with fluorescent protein FRET pairs located inside living cells. For quantitative and statistical cell laser studies, an integrated microwell array platform was developed that features automated and high throughput cell lasing detection, which has been only rarely achieved in any previous cell lasing detection schemes. Using this integrative platform, heterogeneous cell lasing performance was observed among different cell subpopulations within one insect cell line, Sf9, when stained by a DNA-specific dye, SYTO9. This observation suggests the potential of using lasing performance to detect cellular conditions such as nucleus status.

CHAPTER 1: **Introduction**

1.1 **Optofluidic biolasers**

A laser is a light emitting device that generates coherent optical output through a process of optical amplification based on stimulated emission. The light emitted by a laser can have high spatial coherence and temporal coherence. As a result, laser light can have many specific characteristics including high focusability, small spatial divergence, good monochromaticity, and ultra-short temporal duration. Since its invention in the 1960s, the laser has become an indispensable tool in modern industries, basic science research, and modern medicine.[1]

A new class of laser, the biolaser, has started to emerge in the past decade.[2] It is characterized by the incorporation of biomaterials, ranging from molecules such as proteins[3,4] and DNAs[5-7] to macroscale structures such as cells[4] and tissues[8,9], into a laser system. Biomaterials can serve as laser gain media and/or form the optical cavity that provides optical feedback. They can also constitute passive optical components that tune the laser output by modulating the system's effective refractive index. Since biomaterials and bio-events often occur in an aqueous environment, research in biolasers has greatly benefited from optofluidic dye lasers, which integrate microfluidic channels, microcavities, and gain medium in liquid. Indeed, the study of optofluidic dye lasers has greatly inspired and contributed to the development of biolasers. Thus, the term "optofluidic biolaser" is often used interchangeably with "biolaser".

The significance of the integration of biomaterials with lasers has three aspects. First, it provides a novel biochemical sensing platform based on laser emission. The nonlinear and

coherent nature of laser emission enables unprecedented detection sensitivity as well as novel detection aspects such as lasing threshold and lasing mode pattern, shedding light on the development of next generation bio-detection tools. Second, biomaterials exhibit unique properties and make bioengineering technologies available for the design and control of laser systems, which benefit the development of novel photonic devices. Finally, biolasers open a field of study in bio-inspired photonics, which is of fundamental research interest and can deepen our understanding of nature-formed photonic structures as well as photon energy transfer in biological systems.[10,11]

Currently, the study of biolasers primarily falls into the following three categories:

(1) Innovative use of biomaterials as the gain medium

A variety of naturally existing materials have been used as the gain medium, including fluorescent proteins,[3,4] luciferin,[12] chlorophyll[11], and vitamine.[13,14] Studies employing these materials not only increase the prevalence of their choice as gain materials in a laser system but also increase understanding of their photophysical characteristics.

(2) Novel cavity design for improved optical performance, adaptivity, and biocompatibility

High Q factor and single-mode operation are always desired for an optical cavity serving a sensing purpose.[15-17] Miniaturized lasers that can operate in an aqueous environment with a submicron feature size are also of great research interest, as they might be used as imaging probes in novel microscopy.[18] Efforts have also been made to demonstrate all-biocompatible laser systems by fabricating the laser cavity using biocompatible materials. For example, lasers have been achieved with silk-based distributed feedback cavities and ring resonators formed by biodegradable polymer beads, protein beads, and starch granules.[19-22]

(3) Application of biolasers in practical detections at different hierarchical levels, from molecules to cells and tissues

Sun *et. al.* demonstrated the first laser-based detection *in vitro* distinguishing DNA single-nucleotide-polymorphism (SNP) species using molecule beacons with an enhanced sensitivity 100X that of fluorescence.[7] Lasers have also been achieved which incorporate cells and tissues as an active part of the laser system,[4,8,23] further advancing the technology for *in vivo* detections.

Although holding the promise of unprecedented sensitivity, multiplexing capability, and novel applications not previously realized, biolasers are still facing a significant gap preventing practical applications and requiring thorough research from diverse perspectives. An in-depth knowledge of the light-matter interaction in the biolaser process and an interdisciplinary investigation of biolaser systems are highly desired for the development of physiologically relevant biolaser-based analyses.

In this thesis, we propose novel optofluidic biolaser systems that integrate modern technologies, including molecular biology, biochemistry, and microfluidics, and aim to advance biolasers for practical applications.

1.2 **Physics of optofluidic biolasers**

A laser system consists of three fundamental components: a pump (energy source), an optical cavity (optical feedback), and a gain medium. This is also true for a biolaser. Here, a brief overview of the relevant laser physics is provided in the context of a biolaser system. This overview is important for understanding and appreciating biolaser technology and will be widely applied in the theoretical analysis of the experimental observations in later chapters.

1.2.1 Gain medium

Laser gain results from the stimulated emission of electronic or molecular transitions to a lower energy state from a higher energy state. Gain medium is prepared by an excitation pump to populate in the high energy state. A variety of materials have been explored as gain medium in traditional laser schemes, such as ion-doped crystals and glasses, gases, semiconductors, and dyes. For biolasers, dyes in an aqueous solution are most widely adopted and are often excited optically by a pump laser. Each dye has its own characteristic absorption and emission spectrum that is closely related to its energy levels. A typical dye energy level scheme is shown in Fig. 1.1, where the energy bands associated with the electronic levels S_0 and S_1 result from the rotation and vibration of the dye molecules. For simplicity, triplet states are not shown in the diagram. Based on this simplified diagram, a dye is usually modeled as a 4-level system for laser operation as noted by 0 to 3 in the middle of Fig. 1.1. State 1 and State 3 have very short lifetimes due to fast, non-radiative decay. Thus, only State 2 and State 0, denoted as the excited state and the ground state, are usually discussed in a simplified laser model (Fig. 1.1, right). Energy can be released from the excited state either through a radiative pathway (emitting a photon) or a non-radiative pathway (e.g., collision; not shown in the diagram). Fluorescence quantum yield of a dye describes the ratio of its radiative decay rate over the total decay rate from an excited electronic state in the absence of a resonant optical field. Potential laser gain medium should have strong emission (σ_e) and small absorption (σ_a) at the laser wavelength as well as high excitation efficiency. This energy diagram is also applicable to other gain materials, such as fluorescent biomaterials (including fluorescent proteins, chlorophyll, and vitamin riboflavin) and semiconductor quantum dots in a biolaser system with none or minor modifications.
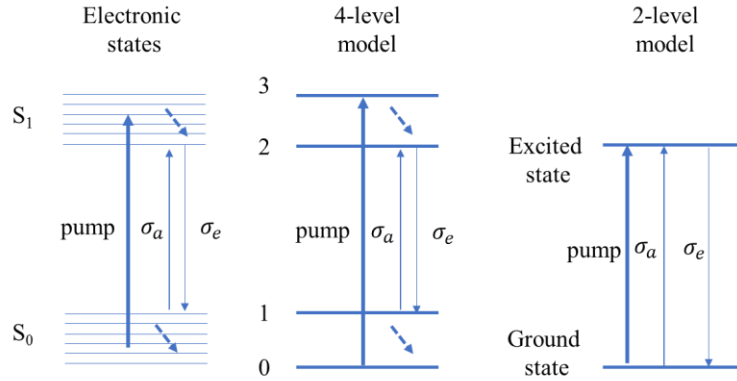
Figure 1.1 Diagrams of dye energy levels associated with laser emission

1.2.2 Optical cavity

Optical cavities trap photons at resonant modes and enable multiple rounds of interaction between a photon and the gain medium before the photon escapes from the cavity. In this process, stimulated emission results in photon accumulation in the resonance mode; optical amplification is thus achieved through the optical feedback provided by the cavity. Optical cavities are usually characterized by their Q factor, which describes the photon trapping capability of the cavity. $Q = 2\pi \frac{energy\ stored}{energy\ dissipated\ per\ cycle}$. The spatial distribution of the optical mode also matters. Sufficient spatial overlap of the optical mode and gain medium is essential for laser emission.

Various types of microcavities have been explored for optofluidic biolasers, including Fabry-Pérot (FP) cavities, whispering gallery mode (WGM)-based ring resonators, and distributed feedback cavities. Different cavity configurations have unique features that are intentionally utilized depending on the particular application. For example, capillary-based ring resonators usually have ultra-high Q factors (up to 10^7) and are intrinsically compatible with liquid samples. FP cavities, though they have relative low Q factors (up to 10^4-10^5), offer whole-body interaction between the optical modes and the gain medium and are easy to integrate with cells and tissues.

1.2.3 Threshold condition of laser

The pump intensity must be above a certain threshold level for a laser to occur. The gain should be equal to the loss at lasing threshold. In a biolaser, the loss mechanism includes molecule absorption, the intrinsic loss of an optical cavity as characterized by Q, and extra scattering loss when biomaterials are present. In the simplified 2-level model, the threshold condition can be written as

$$\zeta \Delta N \sigma_e(\lambda) = \zeta \sigma_a(\lambda) N + \frac{2\pi m}{\lambda Q} \qquad (1.1)$$

where ζ is the fraction of mode energy coupling with the gain medium, ΔN is the concentration of dye molecules in the excited state, $\sigma_e(\lambda)$ and $\sigma_a(\lambda)$ are defined, respectively, as the emission and absorption cross section at the lasing wavelength. m is the effective refractive index, Q the quality factor that takes into account the intrinsic cavity loss and the scattering of the biomaterials. It can be further derived that:

$$\gamma_{th} = \frac{\Delta N}{N} = \frac{\sigma_a(\lambda)}{\sigma_e(\lambda)} \left(1 + \frac{2\pi m}{\lambda \zeta N Q \sigma_a(\lambda)}\right) \qquad (1.2)$$

where γ_{th} denotes the threshold ratio of the excited molecule population for laser to occur.

This formula has been readily adapted to analyze a variety of dye laser systems. It successfully explains the concentration dependency of the lasing envelop and the Q driven lasing wavelength shift, and it can also be used to estimate the effective Q factor of the lasing system in many optofluidic laser systems.[24,25] This formula sets the basis for many laser-based detection schemes since it relates the lasing threshold to the gain concentration. It should be noted that for different cavity designs, the fraction of modes that interacts with gain medium and the corresponding Q factor should be carefully decided.

1.2.4 Rate equations

Rate equations describe the time evolution of the dye molecule energy level populations and the photon density of the laser cavity mode. In a two-level model, the rate equations are as follows:

$$\frac{dn_1}{dt} = R_{pump} + (n_0\sigma_a - n_1\sigma_e)q\frac{c}{m} - \frac{n1}{\tau_1} \qquad (1.3)$$

$$\frac{dq}{dt} = \frac{\zeta c}{m}(n_1\sigma_e - n_0\sigma_a)q + \frac{\zeta c}{mV}n_1\sigma_e - \frac{q}{\tau_q} \qquad (1.4)$$

Where n_1/n_0 denotes the dye concentration at excited/ground state and q is the photon density of the lasing mode. R_{pump} is the excitation rate and is dependent on the pump intensity. σ_e/σ_a is defined as the emission/absorption cross-section of the dye at the lasing wavelength. τ_1 is the fluorescence lifetime of the dye; and τ_q is the lifetime of the laser mode that is dependent on the cavity loss. Finally, c is the speed of light, m is the refractive index, ζ is the fraction of mode energy coupled with dyes and V is the mode volume. The first term in Eq. (1.4) accounts for the stimulated emission and absorption. The second term accounts for the spontaneous emission into the laser mode that is crucial for the initiation of the laser oscillation.

The coupled differential equations can be numerically solved, thus, predicting the laser performance given experimental conditions. Also, it provides a way to account for coupled systems where multiple dyes and laser modes are involved.

1.2.5 Lasing emission versus fluorescence

From the discussion thus far, it is clear that laser emission relies on fluorophores that emit photons upon excitation, just as fluorescence. The difference is that in a laser system, fluorophores are placed in a high Q, optical cavity. A portion of the fluorescence is confined by the cavity and experiences amplification of stimulated emission each time it travels through the

gain medium. The resulting laser emission has distinct spatial, spectral, and temporal features different from fluorescence since it is modulated by the optical cavity. As shown in Fig. 1.2, the threshold behavior and non-linearity near threshold makes laser emission promising as a detection signal that has high sensitivity, high signal-to-noise ratio, and can easily be digitized. The narrow linewidth of laser emission also shows great potential in multiplex detection. Additionally, the coherent nature of laser emission offers rich physics that is not available in non-coherent fluorescence light.
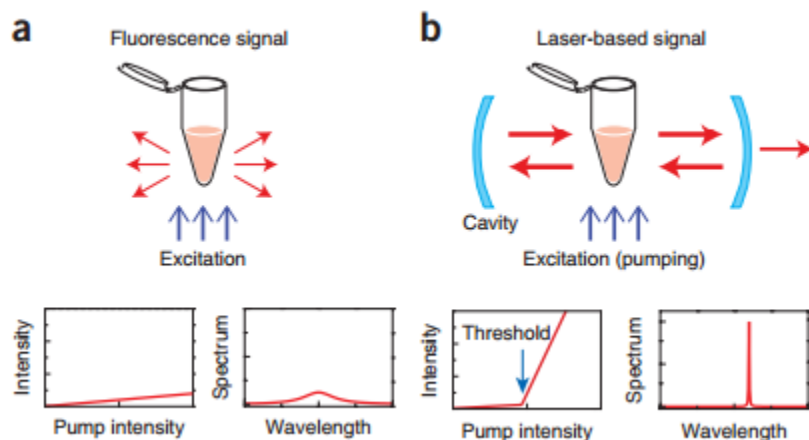
Figure 1.2 Comparison of fluorescence and laser emission. Adapted from Ref.2 with permission.

1.3 Thesis outline

In this thesis, novel integrative biolaser systems are demonstrated with the aim to strengthen the fundamental understanding of biolasers and offer practical tools for laser-based biological/biochemical analyses.

In Chapter 2, fluorescence resonance energy transfer (FRET) is integrated into the laser system. Different biochemical/biological molecules are explored in the FRET laser scheme, showing the high sensitivity of laser emission to FRET efficiencies. In Chapter 3, an optofluidic biolaser based on a single layer of gain molecules is demonstrated, paving the way for surface-

based laser detections. In Chapter 4, biolaser systems incorporating biological cells are investigated. Cell-based FRET lasers are explored, and an integrated microwell array platform is proposed for high throughput and automated detection of lasing signal from cell populations, showing the potential of laser approach in cell analyses. Chapter 5 covers a brief summary as well as an outlook for future work directions.

CHAPTER 2: **Optofluidic FRET biolasers**

2.1 **Introduction**

In this chapter, three different works demonstrating the integration of fluorescence resonance energy transfer and the optofluidic biolaser are presented. Capillary-based optofluidic ring resonators are used, given their high Q factors and inherent capillary microfluidics. It is shown that FRET laser signal can be achieved with fluorescent proteins, dye-labeled DNA tetrahedra, and aqueous quantum dots. These studies show that laser signal is capable of quantifying FRET efficiency with enhanced sensitivity in different sensing schemes and that bio-tuning of laser performance is possible.

2.1.1 Förster resonant energy transfer

Förster resonance energy transfer (FRET) describes an energy transfer mechanism between two chromophores, where the excitation energy of a donor chromophore is non-radiatively transferred to a proximal ground-state acceptor chromophore. The term "fluorescence resonance energy transfer" is more commonly used in scientific literature and corresponds to the case when both chromophores are fluorescent. FRET is a dipole-dipole coupling process. The energy transfer efficiency, E, defined as

$$E = \frac{k_{FRET}}{k_{FRET}+k_f+\sum k_i}$$

(2.1)
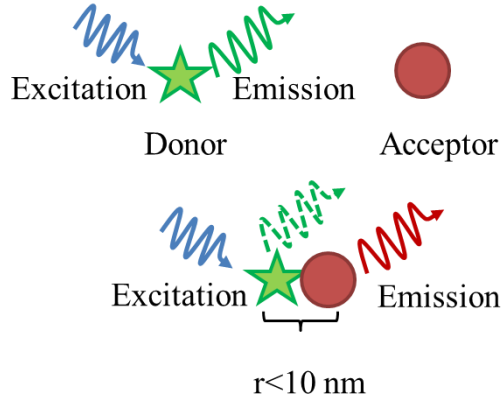
Figure 2.1 Illustration of FRET

(where k_{FRET} is the rate of FRET, k_f the radiative decay rate, and k_i are the rate constants of any other non-radiative decay mechanisms), depends on three parameters: (1) the distance between the donor and the acceptor, (2) the spectral overlap of the donor emission spectrum and the acceptor absorption spectrum, (3) the relative orientation of their dipole moments toward each other. The dependency can be explicitly expressed by

$$E = \frac{1}{1+(r/R_0)^6} \qquad (2.2)$$

where r is the distance between the donor and the acceptor and R_0 is the Förster distance of the specified pair of donor and acceptor dependent on parameters (2) and (3). R_0 denotes the distance between donor and acceptor at which the energy transfer efficiency is 50%.

$$R_0^6 = \frac{9ln10}{128\pi^5 N_A} \frac{\kappa^2 Q_D}{n^4} J \qquad (2.3)$$

where Q_D is the intrinsic fluorescence quantum yield of the donor, n is the refractive index of the medium, N_A is the Avogadro's number, κ^2 is the dipole orientation factor, and J describes the spectral overlap between the donor and the acceptor and is calculated as

11

$$J = \int f_D(\lambda)\varepsilon_A(\lambda)\lambda^4 d\lambda \hspace{3cm} (\,2.4\,)$$

where f_D is the normalized donor emission, ε_A is the acceptor extinction coefficient. $\kappa^2 = \frac{2}{3}$ is often used when both fluorophores are freely rotating and can be considered as isotopically oriented. Typically, the Förster distance R_0 is in the range of 2-10 nm.

FRET is widely exploited as a spectroscopic ruler that can be used to determine distances in the range of about 10 nm by quantifying the energy transfer efficiency. This range is biologically relevant, since biological macro-molecules such as proteins and polysaccharide, and cellular structures such as cell membranes, have a similar feature size. As a result, the applications of FRET in life science, especially in cell biology and molecular biology, have flourished since the 1990s.[26-29] By labeling different domains within a single molecule or different molecules that bind to each other with the donor and acceptor respectively, FRET can provide information regarding intra-molecule and inter-molecule interaction. FRET is also useful in cell membrane dynamics studies, including membrane raft and electric potential monitoring.[30] In these applications, the FRET efficiency is usually determined by measuring the radiometric fluorescence emission of the donor and acceptor fluorophore. Another general method is to measure the fluorescence lifetime of the donor fluorophore, since the donor fluorescence lifetime will significantly drop if FRET occurs.[31] FRET can provide co-localization information with a resolution far beyond the diffraction limit and also enables real time, *in situ* monitoring of biophysical processes.

2.1.2 FRET lasers

FRET is usually indicated by a change of fluorescence intensity or fluorescence lifetime. However, fluorescence signal usually suffers from a low signal to noise ratio. Small changes in FRET efficiency are usually buried in the noise. For example, in ensemble studies, if only a

small portion of the whole population undergoes dynamic changes, the small variance might not be caught by fluorescence signal. The emergence of biolasers inspires the idea that FRET pairs can be put in microcavities and generate laser signal for FRET efficiency detection, resulting in a high signal to noise ratio.

FRET lasers were first investigated in bulk solution dye lasers and solid state lasers for increasing pump efficiency and reducing absorption loss in the laser emission band.[32-35] With FRET, laser emission from the acceptor emission band can be achieved when the pump is at donor's absorption wavelength. Donor laser emission can coexist with acceptor laser emission but with attenuated intensity. This provides an alternative excitation scheme for laser operation other than direct excitation and offers versatility and tunability to a laser system.

The ratio of donor/acceptor laser emission can be used to derive FRET efficiency, similar to fluorescence-based detection.[36,37] Experimental demonstration of FRET lasers as a biochemical sensing signal has recently been reported. In 2012, Zhang et. al. demonstrated FRET laser sensing of ionic concentration by conjugating the FRET pair Cy3 and Cy5 to a DNA Holliday junction.[6] The Holliday junction can be tuned reversibly by Mg^{2+} concentration, which results in varying FRET efficiency between Cy3 and Cy5. Corresponding laser emission ratios proved to have a much higher sensitivity when compared to traditional fluorescence signal. This debut of FRET biolasers inspires further exploration in other detection scenarios.

2.1.3 Capillary-based optofluidic ring resonators

In order to achieve laser signal, the gain must exceed loss in the system. For bio-applications, limitations in gain concentration and relative low quantum yield of bio-compatible gain molecules impose the need for low system loss, in other words, high Q factors of the microcavities.

The capillary-based optofluidic ring resonator (OFRR) is an ideal platform for the demonstration of lasers with fluidic gain medium.[38] A thin-walled glass capillary serves as the optical cavity in this scheme, with wall thickness usually around 2 µm and a diameter of about 70 – 100 µm. The cross section of the capillary supports high Q whispering gallery modes up to 10^7 by total internal reflection whether the refractive index of the liquid inside is higher or lower than that of the capillary wall. For bio-applications, this is especially important since aqueous solutions have a lower refractive index than the glass. Thus, total internal reflection happens at the outer boundary of the capillary wall. A thin wall guarantees mode penetration into the liquid core for sufficient light-matter interaction. Sample volumes as small as a few µL are sufficient for the system. The thin-walled capillary can be fabricated by pulling a thick-wall preform at levitated temperature.
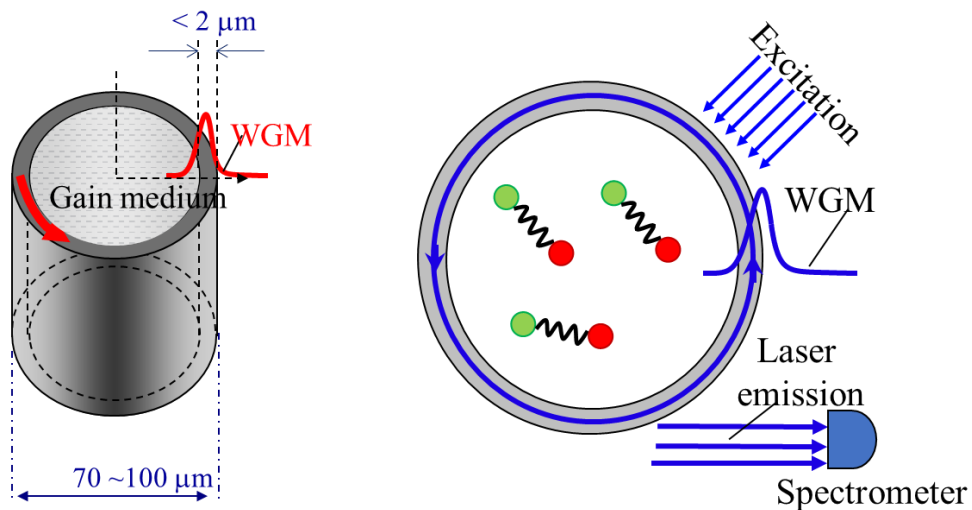
Figure 2.2 The capillary-based optofluidic ring resonator

2.2 Highly sensitive protein FRET laser

Protein-protein interactions play a central role in cellular signaling.[39,40] Monitoring and modulating protein interactions provides important mechanistic insight into cellular processes and is essential for developing pharmacological intervention in disease states. Currently, investigations of protein interactions commonly employ FRET between two genetically encoded fluorescent proteins to extract information about intermolecular and intramolecular changes in proteins.[26] However, conventional fluorescence-based FRET detection suffers severely from small changes in FRET signal (usually only a few percent) in the donor and acceptor emission brought about by weak protein-protein or protein-drug interactions. Enhancement of the FRET response is highly desirable, as it would provide much more detailed information about protein interactions that otherwise cannot be resolved using conventional FRET detection.

An optofluidic protein FRET laser is promising for highly sensitive intra-cavity detection of protein interactions. The optofluidic laser employs stimulated laser emission as the sensing signal. When FRET takes place inside the laser cavity, a small change in FRET induced by protein interactions will be optically amplified by the optofluidic laser, thus resulting in a drastic increase in the FRET signal. As the first step towards fully implementing intra-cavity detection of protein interaction, optofluidic laser emission is obtained from genetically encoded fluorescent proteins in this section. The gene transfection method allows for synthesis of a protein FRET pair linked by a length-tunable peptide, thus providing a highly versatile platform to precisely control the FRET efficiency for systematical investigation of protein interactions.[41] Detailed studies presented below show that the optofluidic laser characteristics could be drastically modulated by the energy transfer between the protein pair, thus significantly enhancing the FRET signal.

2.2.1 Experimental
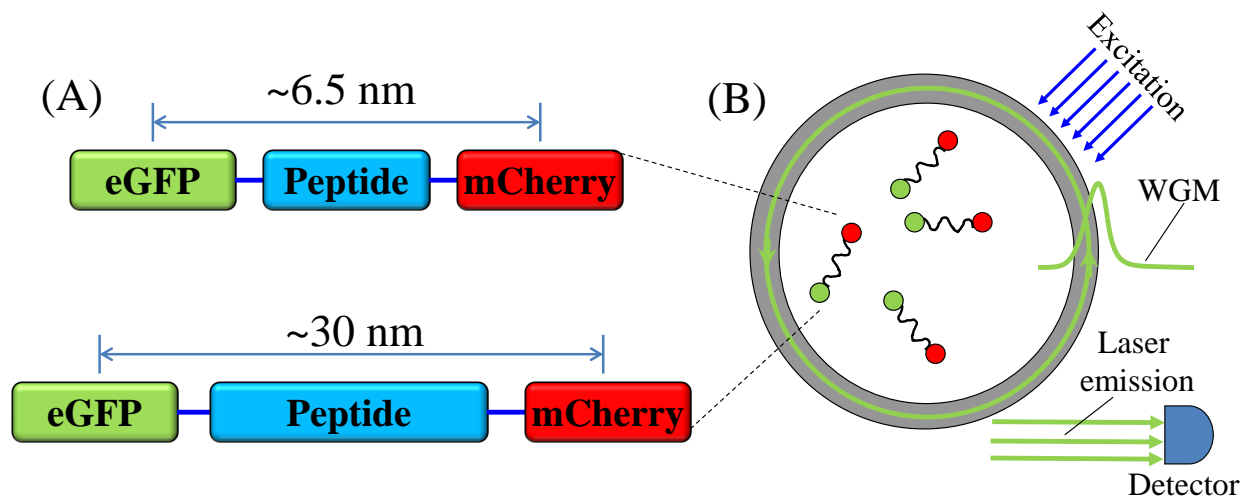
Figure 2.3 (A) Two types of genetically encoded fluorescent protein pairs (eGFP as the donor and mCherry as the acceptor) used in the experiment. eGFP and mCherry were linked by a peptide, whose length could be adjusted during synthesis. (B) The optofluidic ring resonator (OFRR) provides the optical feedback for fluorescent proteins to lase upon external optical excitation with a 5-ns pulsed optical parametric oscillator.

FRET protein pair design.

Two kinds of genetically encoded proteins were used to demonstrate the FRET-modified laser characteristics in this study (Fig. 2.3(A)). The short-linked FRET pair is connected by a short peptide (6-residue protease site and 3-residue Gly-Ser-Gly), making the distance between eGFP (with A206K mutation to minimize dimerization) and mCherry approximately 6.5 nm. The long-linked pair is connected by a length-tunable ER/K α-helix.[41] For the current work, the length was 30 nm. The Förster distance between eGFP and mCherry is about 4.7 nm.

Expression and purification of the protein FRET pair.

Insect cell line Sf9 (a clone originally established from ovarian tissue of the insect *Spodoptera frugiperda*) was used to produce the genetically encoded fluorescent protein pairs. Sf9 cells were transiently transfected with the pBiex1 vector with insertion of a genetic construct encoding either one of the two types of the FRET pairs. Both constructs had a FLAG tag. Cells

were lysed three days post-transfection in HEPES Lysis Buffer (0.5% IGEPAL, 4 mM MgCl2, 200 mM NaCl, 7% Sucrose, 20 mM HEPES, pH 7.5, 5 mM DTT, 50 μg/mL PMSF, 5 μg/mL aprotinin, 5 μg/mL leupeptin). Lysates were clarified by ultracentrifugation (45,000xg, 4°C, 45 min) and bound to Anti-FLAG M2 Affinity gel (Sigma-Aldrich). Gel was washed with HEPES Wash Buffer (150 mM KCl, 20 mM HEPES, pH 7.5, 5 mM MgCl2) and eluted using FLAG peptide. Evaporation was utilized to condense the resulting protein solution to the desirable concentration. FluoroMax-4 spectrofluorometer (Horiba Scientific) was used to characterize the protein pairs. 100 μL 20 nM protein pair was placed in a cuvette. 484 nm and 587 nm light were used to excite the eGFP and mCherry, respectively. The emission of eGFP and mCherry was then collected and analyzed.

The optics system.

To achieve protein lasers, capillary-based OFRR was used (Fig. 2.3(B)). The OFRR had an outer diameter of 90 μm and a wall thickness below 2 μm. During the experiment, ~10 μM solution of the protein pair was withdrawn into the capillary by a syringe pump at a flow rate of 1 μL/min. The solution was excited by a pulsed optical parametric oscillator (OPO) with a pulse duration of about 5 ns and a repetition rate of 20 Hz. Emission of the solution was collected by a multimode optical fiber and sent to a spectrometer for analysis.

2.2.2 Results

The protein pairs used in the experiments were first characterized through fluorescence. Fig. 2.4(A) shows the mCherry emission when the protein pairs were excited within the mCherry absorption band (587 nm). Virtually identical spectra between the long- and short-linked protein pairs suggest that mCherry emission is not affected by its distance from the eGFP (donor). In contrast, when the protein pairs were excited within eGFP absorption band (484 nm), decrease in

the emission of eGFP and concomitant increase in mCherry emission was observed for the short-linked protein pair, as compared to the long-linked protein pair. The energy transfer efficiency E of approximately 17% between eGFP and mCherry is obtained according to:

$$E = 1 - \frac{I_{D,FRET}}{I_{D,0}}. \qquad (2.5)$$

$I_{D,FRET}$ and $I_{D,0}$ are the donor emission in the presence and absence of FRET, respectively. The experimentally measured energy transfer efficiency agrees well with the estimation obtained by using Eq. (2.2), with the Förster distance R_0=4.7 nm and the distance between eGFP and mCherry r=6.5 nm.

A control experiment was carried out before investigating the FRET effect on the protein laser emission. Previously, in Fig. 2.4(A) it is showed that the fluorescence from mCherry was not affected by its distance from eGFP when the protein pairs were excited directly within the
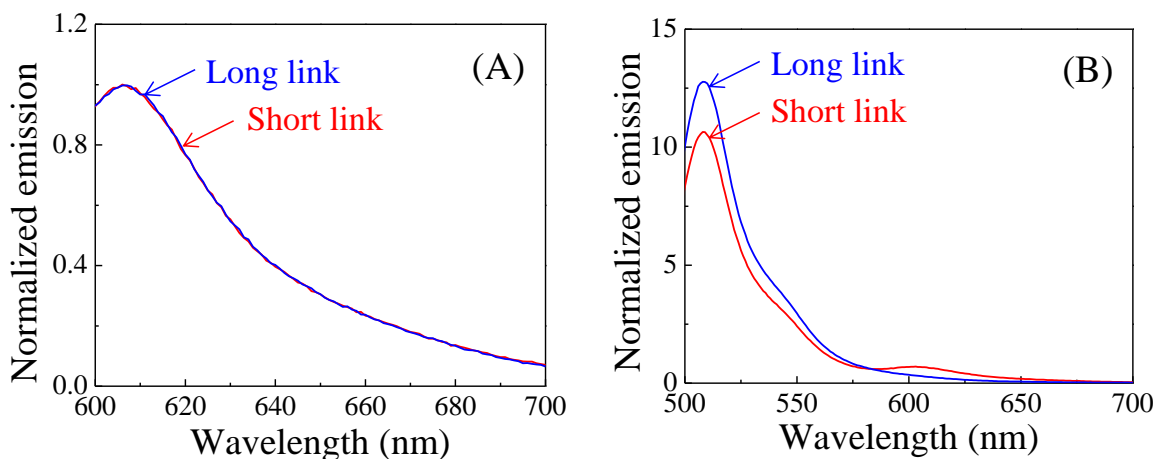
Figure 2.4 (A) The mCherry fluorescence emission spectra for the long- and short-linked protein pairs normalized to their respective emission peaks. Excitation wavelength was 587 nm so that only the acceptor was excited. (B) The donor and acceptor spectra for the long- and short-linked protein pairs normalized to their respective acceptor emission peaks in (A). Excitation wavelength was 484 nm so that only the donor was excited. FRET efficiency is approximately 17% based on Eq. (2.5). The spectra were obtained using FluoroMax-4 spectrofluorometer (Horiba Scientific).
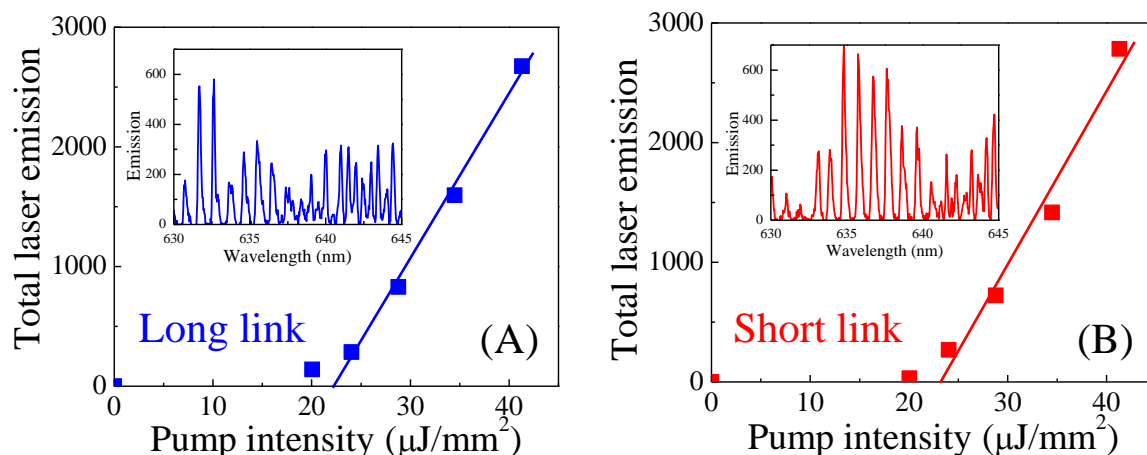
Figure 2.5 Spectrally integrated mCherry lasing emission vs. pump intensity for (A) long- and (B) short-linked protein pairs. Spectral integration takes place between 621 nm and 655 nm. The excitation wavelength was 588 nm from the OPO so that only mCherry was excited. The lasing threshold is approximately 22.4 and 23.2 $\mu J/mm^2$ for long- and short-linked protein pairs, respectively. Solid curves are the linear fit above the respective lasing threshold. The insets show part of the mCherry lasing spectra for long- and short-linked protein pairs when pumped at 41 $\mu J/mm^2$.

mCherry absorption band (far from that of eGFP). Likewise, Figure 2.5 compares the laser emission from mCherry for both long- and short-linked protein pairs when they were excited with the OPO at 588 nm, at which wavelength only mCherry was excited. Nearly identical lasing threshold curves with the same lasing thresholds and laser efficiencies (the slope above the lasing threshold) were obtained, suggesting that both long- and short-linked protein samples were identical with respect to mCherry. Additionally, since eGFP and mCherry in each sample had the exact molar ratio (1:1), the result in Fig. 2.5 further indicates that both long- and short-linked samples were identical, except the distance between eGFP and mCherry.

Figure 2.6 investigates the FRET effect on the eGFP lasing characteristics. Fig. 2.6(A) compares the eGFP laser emission threshold curve between the long- and short-linked protein pairs. For the long-linked pair, the distance between eGFP and mCherry (~30 nm) is much larger than their Förster distance (4.7 nm). Therefore, the FRET effect of mCherry on eGFP is
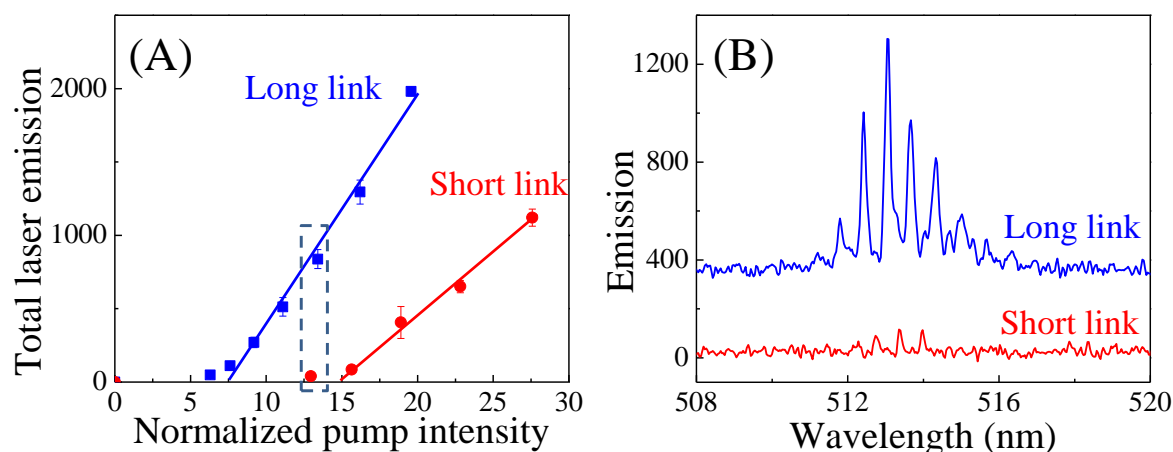
Figure 2.6 (A) Spectrally integrated eGFP lasing emission vs. pump intensity normalized to their respective mCherry lasing threshold for long- and short-linked protein pairs. Spectral integration takes place between 508 nm and 542 nm. Error bars are obtained by five measurements. (B) eGFP laser emission spectrum for long- and short-linked protein pairs when pumped at 300 $\mu J/mm^2$ (corresponding to the boxed data points in (A)). Curves are vertically shifted for clarity. The excitation wavelength was 488 nm from the OPO.

negligible and strong eGFP laser emission emerged in the experiment. In contrast, for the short-linked protein pair (~6.5 nm), the energy transfer efficiency is about 17%. Though small, this is sufficient to cause drastic changes in the eGPF laser characteristics with 2x increase in the lasing threshold and 2x reduction in the lasing efficiency. In a typical FRET measurement, the donor emission reduction can be used as the sensing signal. Fig. 2.6(A) shows that 5-25x reduction in the eGFP laser emission can be obtained when the pump ranges from 12.5 to 22.5. One example with 25x reduction is shown in Fig. 2.6(B). Note that even a larger reduction ratio can be achieved when the pump is between 7.5 and 12.5. In this case, the eGFP lasing is completely quenched for the short-linked protein pair and only fluorescence exists the intensity of which is usually over 100x smaller than the laser emission.

2.2.3 Discussion and outlook

In summary, in this work, laser emission from eGFP and mCherry using optofluidic lasers was demonstrated. The results show that the donor (eGFP) laser emission can be strongly affected by the presence of the acceptor in proximity. Up to 25x reduction in the donor emission

was observed using the optofluidic laser intra-cavity detection method, as compared to only 17% in the conventional FRET.

This work provides two new approaches to quantifying the protein interaction sensitively. The first one is through analyzing the FRET signal typically used in protein interaction analysis but amplified by the optofluidic laser. The second one utilizes the lasing threshold unique to the optofluidic laser and unavailable in the conventional FRET analysis. In both approaches, a series of protein donor and acceptor pairs with well-defined distances (such as those used in our current work) can be used as the calibrator. Meanwhile, a rigorous theoretical model can be established to aid quantitative analysis of protein interactions.

There are a few drawbacks of our approach that need to be overcome. While the analysis time for the first approach is as fast as the conventional FRET analysis, the second approach is time-consuming, as it requires acquisition of emission spectra at different levels of excitation. This issue can be mitigated with robotic systems for autonomous measurement. The other challenge relates to the protein concentration. In the current work, ~10 μM of protein is needed, which is 10-100 higher than that for conventional FRET analysis. However, due to the excellent microfluidic design, the total protein mass used in our method is the same as or even lower than that in conventional FRET analysis. In addition, it needs to be emphasized that in protein-protein or protein-drug analysis, what is of paramount importance is not to detect protein of trace quantities (like in typical biosensing) but to discern the small difference or change in those interactions.

In the future, protein FRET pairs whose distance can be modulated by the presence of drug molecules can be used to demonstrate FRET laser. The significantly enhanced FRET signal will help differentiation the efficacy of drug molecules, which is difficult to accomplish with the

current FRET technology due to small FRET signal caused by drug molecules. This work also inspires translation of the optofluidic laser intra-cavity detection technology into living cells. Combination of bio-functional protein FRET pairs and the cell laser, will open a door to a broad range of applications in protein interaction studies, cellular signaling, and drug discovery.

2.3 FRET laser with tunable gain control using DNA tetrahedron

With the unparalleled ability of programmable hybridization through unique base pair recognition, DNA holds great promise as a powerful material for construction of a wide range of highly uniform and well defined nanostructures.[42-46] In particular, DNA tetrahedral nanostructures[47-49] have received intense interest due to its synthesis simplicity, mechanical rigidity, structural stability, and modification versatility. Based on these unique features of DNA tetrahedra, there have been a variety of applications including sensors,[50,51] logic gates,[52] fluorescent nanotags,[53] and nanocages for protein encapsulation and drug delivery.[54,55] The size and geometry of DNA tetrahedra are also highly tunable and can be readily adjusted by varying the length and conformation of edge strands.[56] Hence, it is possible to design dynamic tetrahedral nanostructures that can finely manipulate optical and electrical interactions of functional molecules anchored on DNA tetrahedra.[52]

Indeed, DNA nanostructures offer versatile ways for anchoring of (bio)molecules and nanoparticles with high addressability and a nanoscale resolution of 6 nm. By exploiting such a property, Kuzyk *et al.* employed a DNA origami structure to precisely assemble gold nanoparticles into chiral plasmonic nanostructures with tailored optical response.[57] More recently, Acuna *et al.* designed a plasmonic nanoantenna structure that site-specifically attached gold nanoparticles to form hotspots for fluorescence enhancement.[58] Likewise, DNA tetrahedra provide an ideal platform for precise anchoring of metal nanoparticles for optical applications.[59,60]

Here we demonstrate that tetrahedral DNA nanostructures could be employed for precise controlling and finely tuning the gain of an optofluidic laser.[3,61-66] The laser gain is one of the most important parameters, which determines many other laser characteristics such as

lasing threshold, efficiency, and output power.[67] Combination of the aforementioned biological nano-engineering concept and the optofluidic laser takes advantage of the self-recognition and self-assembly capabilities of biomolecules with sub-nanometer accuracy, and well-defined structures and stoichiometry, thus enabling precise control over and tuning of the laser characteristics at the molecular level.

The gain medium of the optofluidic laser shown in this work consisted of a fluorescence resonance energy transfer (FRET) pair, Cy3 (donor) and Cy5 (acceptor), attached to the vertex of the DNA tetrahedron (Figure 2.7(A) and (B)). Cy3 acts as antenna to collect the excitation light and then transfers the energy through FRET for Cy5 to lase. Optimization of the Cy3 and Cy5 arrangement on the DNA tetrahedron resulted in significant improvement in lasing characteristics with 4-fold reduction in the lasing threshold and 28-fold increase in the lasing efficiency.

2.3.1 Experimental

DNA tetrahedron preparation and characterization.

Two types of DNA tetrahedral were used. 1Cy3-3Cy5 has 1 Cy3 molecule and 3 Cy5 molecules attached to each tetrahedron, whereas 3Cy3-1Cy5 has 3 Cy3 molecules and 1 Cy5 molecule attached to each tetrahedron. Each type of tetrahedron was formed by mixing four 32-base single-stranded DNA (Table 2.1) in a stoichiometric ratio (1 μM) in $1\times$ TM-Mg buffer (20 mM Tris-HCl, 20 mM MgCl$_2$, adjusting pH to 8.0 by acetic acid). After the formation of the tetrahedral nanostructure, each arm has 10 bases with a length of 3.4 nm. The solution was heated to 95°C for 8 min and then quickly cooled to 4 °C. The prepared DNA tetrahedra were concentrated using a 100 kD Centricon spin-filter (Millipore). The formation of DNA tetrahedrons was characterized and confirmed with native 10% polyacrylamide gel (PAGE) run

Name	Sequence（5'-3'）
LA1	cy3-TAAGTCTGAAAATTACAGCTTACGCCATAGTA
LA2	cy5-TAAGTCTGAAAATTACAGCTTACGCCATAGTA
LB	cy5-TATCACCAGGAAAGCTGTAATAGGTCCAATAC
LC	cy3-CCTGGTGATAATACGTGGGAAATACTATGGCG
LD1	cy3-TTCAGACTTAATTCCCACGTAAGTATTGGACC
LD2	cy5-TTCAGACTTAATTCCCACGTAAGTATTGGACC

Table 2.1 DNA strands used in the experiment. LA2, LB, LC, LD2 are for 1Cy3-3Cy5, the left tetrahedron in Fig. 2.7(A). LA1, LB, LC, LD1 are for 3Cy3-1Cy5, the right tetrahedron in Fig. 2.7(A).
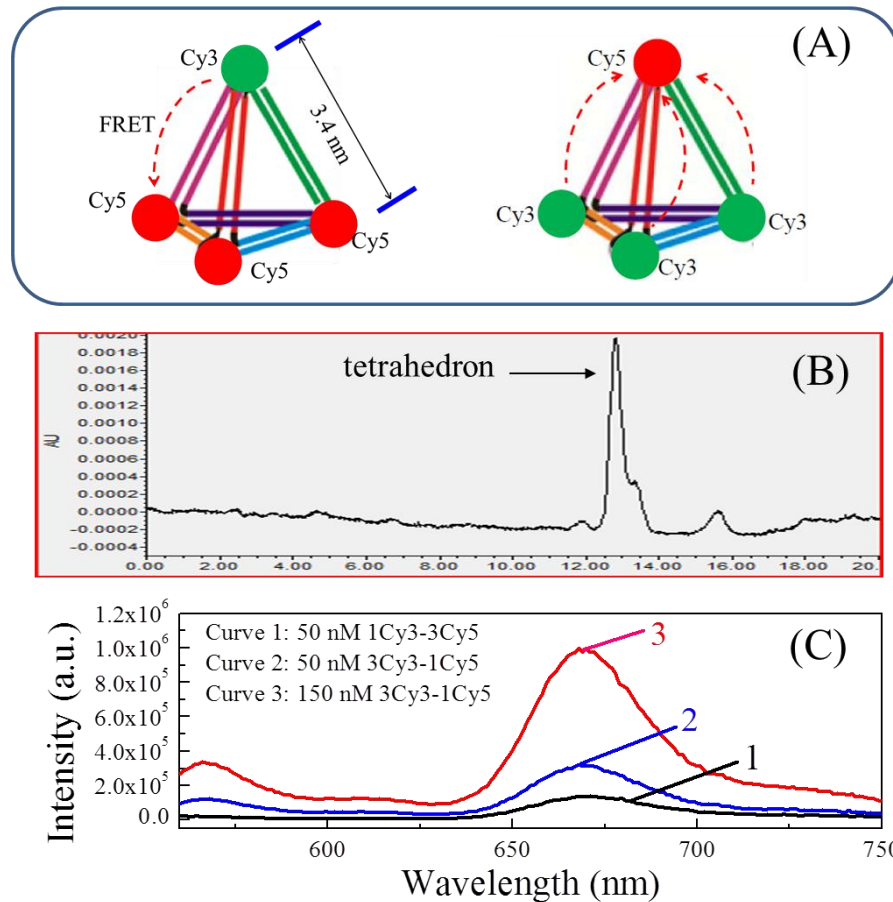
Figure 2.7 (A) DNA tetrahedra used in the optofluidic FRET laser by mixing four 32-base single-stranded DNA listed in Table 2.1. Left: 1Cy3-3Cy5, molar ratio between Cy3 (donor) and Cy5 (acceptor) was 1:3. Right: 3Cy3-1Cy5, molar ratio between Cy3 (donor) and Cy5 (acceptor) was 3:1. (B) Confirmation of the purified DNA tetrahedra with HPLC. The peak with the arrow corresponds to the formed DNA tetrahedra. (C) Fluorescent analysis of DNA tetrahedra labeled with the Cy3-Cy5 FRET pair (λ_{ex} = 555 nm). Curve 1 is for 50 nM of 1Cy3-3Cy5, whereas Curve 2 and 3 are for 50 nM and 150 nM of 3Cy3-1Cy5, respectively.

at 4 °C and stained with SYBR Gold (see Figure 2.7(B)). Fluorescence tests were carried out using an Edinburgh Instruments F900 spectrofluorometer (see Figure 2.7(C)), which clearly showed the presence of FRET between Cy3 and Cy5. Furthermore, comparison of Curve 2 and 3 with Curve 1 suggests that the tetrahedra with multiple donors (3Cy3-1Cy5) have higher acceptor excitation (and hence emission) than those with multiple acceptors (1Cy3-3Cy5).

Laser detection

During the experiment, we used 15 μM of the 1Cy3-3Cy5 tetrahedron and 45 μM of the 3Cy3-1Cy5 tetrahedron, which ensured that both samples had the same concentration of the lasing medium (Cy5), thus eliminating the concentration dependence in lasing parameters such as the lasing threshold[25,68] and allowing us to compare the two laser systems directly. The sample in 1x TM-Mg buffer was withdrawn into an OFRR capillary by a syringe pump. The solution was excited by a pulsed optical parametric oscillator (OPO, 5 ns pulse width and 20 Hz repetition rate) within the Cy3 (donor) absorption band (518 nm). Cy5 (acceptor) was subsequently excited to lase through the FRET process, whose laser emission was collected by a multimode optical fiber and sent to a spectrometer for analysis.

2.3.2 Results

The experiment results show that DNA tetrahedra with different donor-to-acceptor ratios have different laser characteristics in the optofluidic laser system. The performance of the optofluidic laser is significantly improved by optimization of donor/acceptor arrangement. Figure 2.8 shows the lasing spectrum of both 1Cy3-3Cy5 and 3Cy3-1Cy5 when pumped near or well above the threshold. Laser modes are observed in the wavelength range within the acceptor (Cy5) emission band. Note that the longest lasing wavelength for the 3Cy3-1Cy5 system is around 740 nm, red-shifted from that for the 1Cy3-3Cy5 system. This red-shift is strong
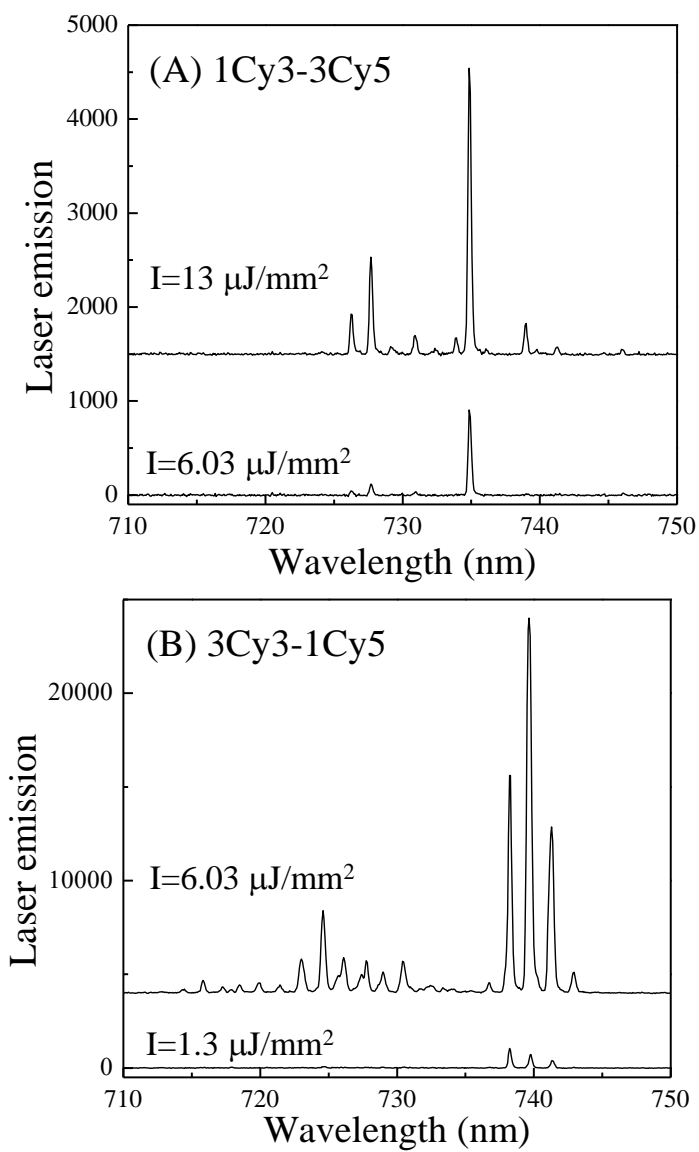
Figure 2.8 Optofluidic laser spectra from Cy5 for 1Cy3-3Cy5 (A) and 3Cy3-1Cy5 (B) at different pump energy densities. Concentration was 15 µM and 45 µM for (A) and (B), respectively. Other conditions such as buffer, temperature, and flow rate remained the same.

evidence that the 3Cy3-1Cy5 system has a larger gain.[68,69] Indeed, such difference in the gain is quantitatively reflected in the lasing threshold of the 3Cy3-1Cy5 system, as shown in Figure 2.9, which is 3.8 times lower than that of the 1Cy3-3Cy5 system (1.18 μJ/mm^2 vs. 4.5 μJ/mm^2). Furthermore, according to Figure 2.9, the lasing differential efficiency (slope of laser emission vs. pump intensity) is 28-fold enhanced in the 3Cy3-1Cy5 system, in comparison with that in the 1Cy3-3Cy5 system, suggesting that efficient photon conversion can be achieved by simply re-arranging the molar ratio between the donor and the acceptor.
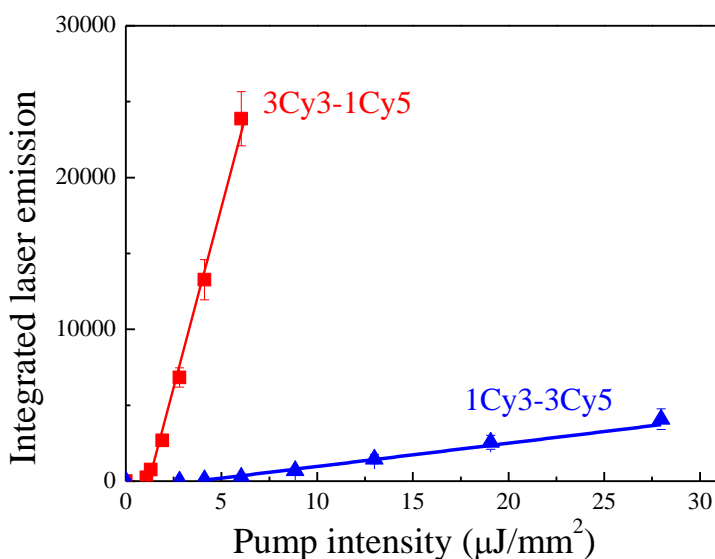
Figure 2.9 Spectrally integrated laser emission as a function of pump intensity for 1Cy3-3Cy5 and 3Cy3-1Cy5 lasers. The lasing threshold was 4.5 μJ/mm^2 and 1.18 μJ/mm^2 for 1Cy3-3Cy5 and 3Cy3-1Cy5, respectively. The laser differential efficiency was 174 mm^2/μJ and 4770 mm^2/μJ for 1Cy3-3Cy5 and 3Cy3-1Cy5, respectively. Solid lines are the linear fit above the lasing threshold. Spectral integration takes place between 683 nm and 756 nm. Error bars are obtained with 5 measurements.

2.3.3 Theoretical analysis and discussion

Theoretical analysis is performed to account for the drastic difference between the two tetrahedron configurations. The excitation of the laser gain medium (*i.e.*, Cy5) comes from the

excitation of the donor (Cy3), which later transfers to the acceptor (Cy5) via FRET. The rate equations for the 1Cy3-3Cy5 system can be approximately expressed as:

$$\frac{dn_{Cy3,1}}{dt} = R_p - k_{Cy3} \cdot n_{Cy3,1} - 3k_{FRET} \cdot n_{Cy3,1} \qquad (2.6)$$

$$\frac{dn_{Cy5,1}}{dt} = k_{FRET} \cdot n_{Cy3,1} - k_{Cy5} \cdot n_{Cy5,1} \qquad (2.7)$$

where $n_{Cy3,1}$ and $n_{Cy5,1}$ are the fraction of Cy3 and Cy5 molecules in the excited state, respectively. k_{Cy3} and k_{Cy5} are the decay rate for Cy3 and Cy5 at the excited state, respectively. k_{FRET} is the energy transfer rate. R_p is the excitation rate for Cy3, *i.e.*:

$$R_p \propto n_{Cy3,total} \cdot \sigma_{Cy3} \cdot I_p, \qquad (2.8)$$

where $n_{Cy3,total}$, σ_{Cy3}, and I_p are the total number of Cy3 molecules, the Cy3 absorption cross section, and the external pump light intensity, respectively. Under the steady-state approximation, the excitation of Cy5 is:

$$n_{Cy5,1} \propto \frac{E}{3} \cdot n_{Tetrahedron} \cdot \sigma_{Cy3} \cdot I_p, \qquad (2.9)$$

where $n_{Tetrahedron}$ is the number of tetrahedra. E is the FRET efficiency:

$$E = \frac{3R_0^6}{r^6 + 3R_0^6}, \qquad (2.10)$$

where R_0 is the Förster distance for Cy3 and Cy5. r is the distance between Cy3 and Cy5. Similarly, the excitation of Cy5 in the 3Cy3-1Cy5 system is given by:

$$n_{Cy5,1} \propto 3E' \cdot n_{Tetrahedron} \cdot \sigma_{Cy3} \cdot I_p, \qquad (2.11)$$

where

$$E' = \frac{R_0^6}{r^6 + R_0^6}. \qquad (2.12)$$

Given R_0=6 nm and the r=3.4 nm in our current system, E and E' are calculated to be 99% and 97%, respectively, for 1Cy3-3Cy5 and 3Cy3-1Cy5. Since the lasing threshold is directly related to the fraction of gain medium molecules (Cy5) in the excited state, the lasing threshold for 3Cy3-1Cy5 is thus calculated to be 8.8 times lower than for 1Cy3-3Cy5, qualitatively agreeing with the experimental results. The quantitative discrepancy between the experiment result and theoretical analysis might result from the optical loss in the Cy5 emission caused by extra Cy3 absorption in 3Cy3-1Cy5, as it has 9 times more Cy3.[25,70]

The experiment observation and the theoretical study presented above introduce two ways of laser gain control in an optofluidic laser. The first method utilizes the DNA scaffold technique to explore the ratio of the donor to the acceptor for different gain characteristics. When an acceptor is surrounded by multiple donors in proximity, high excitation efficiency of the acceptor can be achieved in comparison with the case where only one donor is available. More generally, a hierarchy structure can be used for even higher excitation efficiency, where the acceptor is excited via FRET from multiple intermediate molecules, each of which is in turn excited via FRET from multiple donors. The second method is to adjust the distance between donor and acceptor through flexible or reconfigurable DNA structures to control the FRET efficiency and hence the gain medium excitation efficiency. In the DNA tetrahedron case, the length of the tetrahedron edge can finely be tuned by varying the number of base pairs and/or conformational change of the embedded functional domain.[52] These two methods can work in tandem to provide better control over the laser characteristics.t

In conclusion, DNA tetrahedra were used to control the optofluidic laser through FRET acceptor/donor arrangement. This work synergizes flexible, programmable, and cell-permeable DNA tetrahedron nanostructures and the optofluidic laser technology, which has high sensitivity

and handles nano-liter sized sample volumes with ease. Therefore, a broad range of applications can be explored in the area of novel photonic devices, bio-nanotechnologies, biochemical sensing, and biomedical research.

2.4 **Quantum dot FRET laser**

Semiconductor colloidal quantum dots (QDs) are another type of fluorophore that possess unique photo-physical properties such as color tunability by size, high brightness, and good photostability that are of great importance for the development of the optofluidic laser technology.[71-74] In particular, due to high light absorption capability in the blue and UV region, QDs can collect the excitation light more efficiently, resulting in a significantly lower lasing threshold.[74] More recently, optofluidic lasers using biocompatible QDs in an aqueous environment have been demonstrated, paving the way to actual biochemical applications with optofluidic QD lasers.[72,74] In addition to directly acting as the gain medium, QDs have the potential to work as the donor in a FRET laser. In fact, in the context of traditional fluorescence based detection, QDs have been extensively studied as the donor[75-80] or acceptor[28] in a FRET pair for various biosensing applications. QDs are especially well suited as donors due to their broad absorption bands, tunable emission bands for controllable spectral overlap with acceptors, and large Stokes shifts for suppression of direct excitation of acceptors.[81,82] However, despite extensive studies of QDs in fluorescence based FRET, up to date the performance of QDs in an optofluidic FRET laser has rarely been explored.[37]

In this work, an optofluidic QD FRET laser using commercial water-soluble QDs (donor) and dye molecules (acceptor) was developed and studied as a model system. It is showed that QDs can assist acceptor dye lasing with an excitation wavelength far from the dye absorption band thanks to FRET. The efficiency of our QD FRET laser in comparison with the directly excited dye laser was also investigated. The limiting factors of the FRET laser performance are revealed to be the FRET energy transfer rate and the non-radiative Auger recombination. This study has two implications. Firstly, to the best of our knowledge, it is the first demonstration of a

FRET laser using aqueous QDs as the donor. The integration of optofluidic laser technology with QD FRET that is conceptually demonstrated here has great potential in building ultra-sensitive, versatile, and robust platforms for biochemical sensing applications. QDs, with their unique photo-physical properties, are expected to improve the performance of optofluidic FRET lasers and bridge the gap between laboratory technology and real applications. Secondly, the role of QDs in a FRET laser is of general scientific interest. The optofluidic QD FRET laser studies can also be instrumental in understanding the photo-physical properties of QDs as the laser gain medium and as the FRET donor, and in revealing their similarity to and dissimilarity from organic dyes in FRET processes. The knowledge obtained will be important for us to take advantage of QDs and overcome their limitations.

2.4.1 Experimental

Conjugation of Qdots with acceptor dye Cy5

Water-soluble QDot 655 (Invitrogen) and Cy5 were chosen to be the FRET donor and acceptor in this work. QDot 655 has an organic PEG coating that has active amino groups on the surface. Its emission peak is centered at 655 nm, which has significant overlap with the Cy5 absorption band. Cy5 was purchased from Sigma-Aldrich, which has NHS ester that can react with amines for labeling (Cy5 NHS ester). In addition, Cy5 labeled on a DNA (Cy5-DNA) was purchased from Integrated DNA Technologies, which served as a negative control in our studies. The reason to use Cy5-DNA, instead of pure Cy5, is that Cy5-DNA can dissolve in PBS buffer much more efficiently than pure Cy5.

The covalent immobilization method was used to link Cy5 NHS ester to the QD surface, which, along with the sample characterization, is described as follows. After changing the buffer of QDot 655 from original borate buffer to PBS with 100K Amicon Ultra-0.5 centrifugal filter,
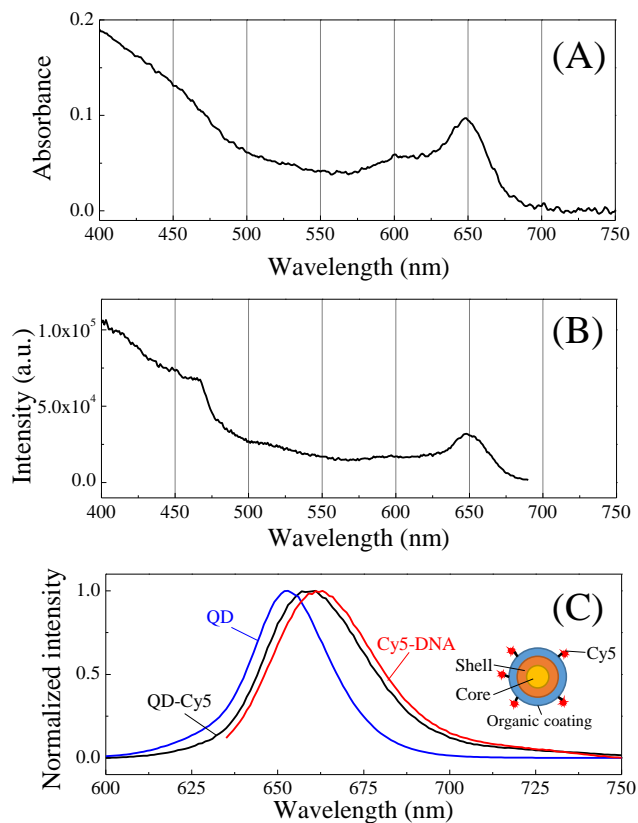
Figure 2.10 Characterization of the Cy5-conjugated QD sample. (A) 1 mm absorbance of 10X diluted sample. (B) Photoluminescence excitation spectrum of the same sample as in (A). Emission was collected at 720 nm. (C) Normalized emission spectra of pure QD, QD-Cy5 conjugation, and Cy5. Inset: a QD-Cy5 conjugate.

100 µL 6.25 µM QDot 655 was mixed with 150 µg Cy5 NHS ester and incubated for 1 hr. Then the mixture was filtered with a resin column that separates free Cy5 NHS ester from QD-Cy5 conjugation. Multiple tests were performed to characterize the resulting sample.

Characterization of the Qdot-Cy5 conjugation

According to the absorption test with NanoDrop 2000c UV-Vis spectrophotometer (Fig. 2.10(A)), the concentration of QD and Cy5 was calculated to be 3.3 µM and 29 µM, respectively, corresponding to a labeling ratio of 9 (*i.e.*, 9 Cy5 molecules covalently linked to one QD on

average). The existence of FRET in the QD-Cy5 conjugation was verified by photoluminescence excitation (PLE) conducted with FluoroMax-4 spectrofluorometer, in which emission intensity at 720 nm from Cy5 was monitored while scanning the excitation wavelength from 400 nm to 690 nm. A similar pattern was observed in the PLE spectrum compared to the absorption spectrum, as shown in Fig. 2.10(B), indicating that photons absorbed by QDs can be transferred to Cy5 emission through FRET. Emission spectrum in Fig. 2.10(C) further shows a peak centered around 665 nm, red-shifted from original QD peak at 655 nm, which is due to the combination of contribution from QDs and Cy5 when excited at 430 nm where Cy5 has negligible absorption. Further clues for FRET can be derived from lifetime measurements. The measured lifetime of the original QDot 655 sample is 34.6 ns. In the conjugate sample, QDot 655 lifetime is significantly reduced to 4.4 ns, indicating the existence of the fast FRET energy transfer decay channel. A FRET efficiency of 87% can be calculated from the reduced lifetime of QDs in the conjugate sample.

Optical system

For optofluidic laser studies, we used the capillary-based OFRR as the platform. A typical confocal setup was used to excite the sample and collect emission light. A pulsed OPO laser (pulse width: 5 ns, repetition rate: 20 Hz) was used as the excitation source. Pump intensity was adjusted by a continuously variable neutral density filter. The laser beam was focused on the OFRR using a 20 mm lens. The emission light was collected through the same lens and sent to the spectrometer (Horiba iHR550) for analysis.

2.4.2 Results

FRET modulated lasing from Qdot-Cy5 conjugate

As a control experiment, we first ran a 30 μM Cy5-DNA sample in PBS buffer in the system and studied its lasing performance, which had almost the same Cy5 concentration as in the QD-Cy5 conjugate sample. When excited at 450 nm, no lasing could be observed within the system excitation power capability (up to 550 $\mu J/mm^2$). As exemplified in the red curve in Fig. 2.11(A), only featureless emission spectrum is observed. In contrast, when the QD-Cy5 conjugate sample was flowed through the same capillary immediately after the experiments with the Cy5-DNA, Cy5 lasing peaks emerged around 730 nm (Fig. 2.11(A), black curves) with excitation at the same wavelength (450 nm). The measured linewidth of the lasing peaks was 0.32 nm, much sharper than fluorescence emission. This linewidth is limited by the resolution of our spectrometer (0.05 nm with 600 g/mm grating) and by the fact that each peak may contain multiple lasing modes that have slightly different lasing wavelengths. The red shift of the lasing peak relative to the fluorescence emission peak of Cy5 is typical for dye lasers,[38] caused by the self-absorption of Cy5 and additional absorption of QDs. Fig. 2.11(B) plots the Cy5 laser output as a function of pump intensity. A threshold pump intensity of 14 $\mu J/mm^2$ is derived by fitting the lasing output above threshold. Beyond the threshold, the Cy5 lasing emission increases linearly with the increased pump intensity, but levels off when the pump intensity is above 100 $\mu J/mm^2$, which indicates saturation in excitation. From these measurements, it can be concluded that through conjugation with QDs, which has strong absorption around 450 nm, Cy5 lasing emission can be achieved via FRET.
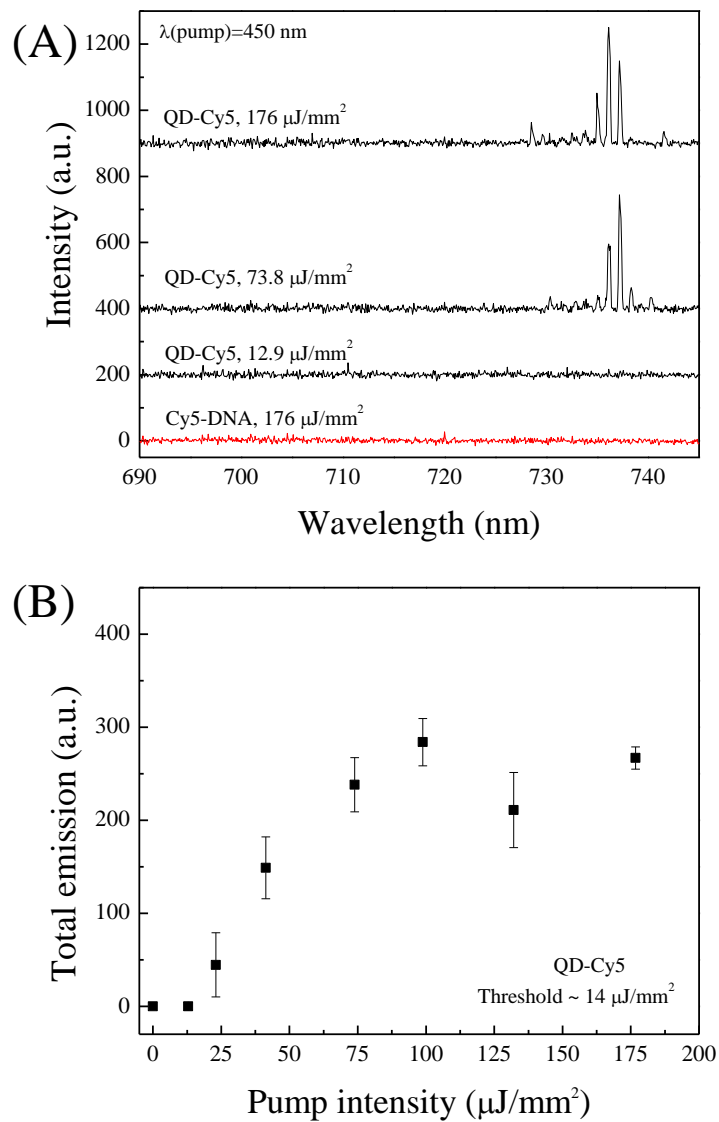
Figure 2.11 (A) Emission spectra of QD-Cy5 and Cy5 when pumped at 450 nm. Spectra are vertically shifted for clarity. (B) Spectrally integrated emission versus pump intensity for QD-Cy5 when pumped at 450 nm. Spectral integration takes place in the range of 730-740 nm. The lasing threshold for QD-Cy5 is approximately 14 $\mu J/mm^2$. Each data point was collected upon single pulse excitation in order to minimize photo-bleaching. Error bars are obtained with 3 measurements. Concentration of Cy5 in QD-Cy5 in (A) and (B) was 29 μM.
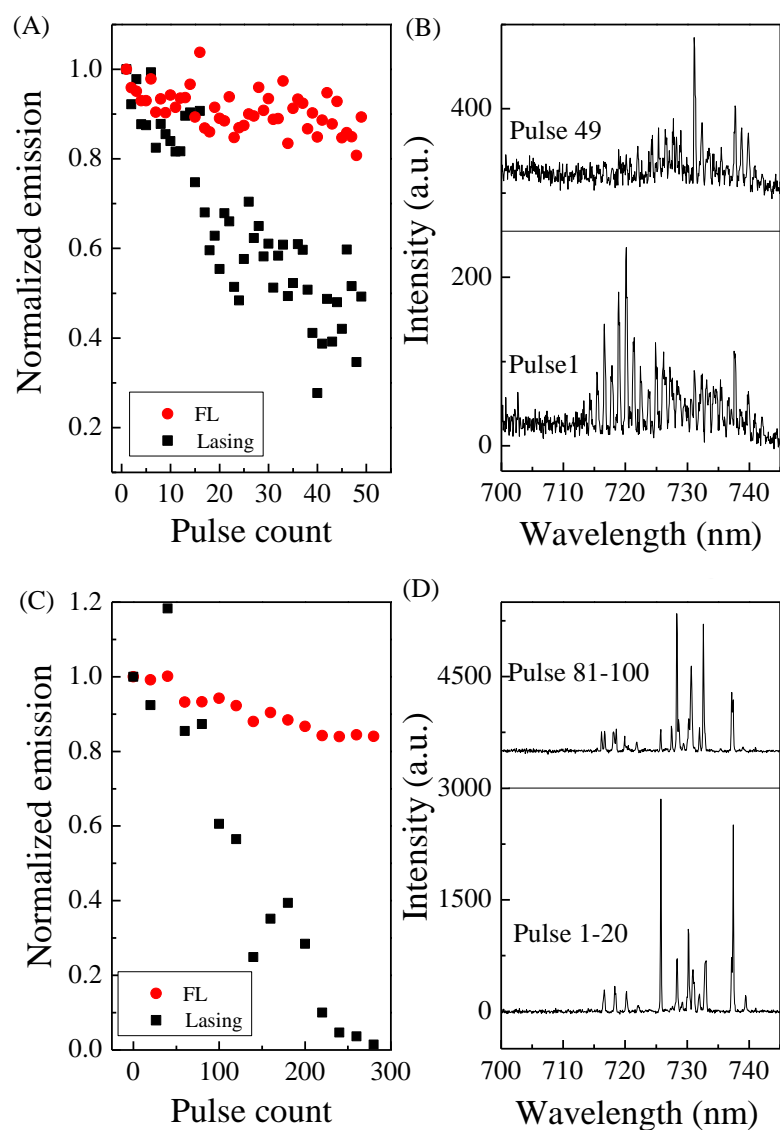
Figure 2.12 QD-Cy5 FRET lasing stability study. (A) Normalized spectrally integrated emission for Cy5 fluorescence (675 – 705 nm) and Cy5 lasing (710 – 740 nm) under 176 μJ/mm^2 excitation. Each data point represents the normalized emission under excitation of a single pulse. (B) The corresponding Cy5 laser emission spectrum for the 1st and 49th excitation pulse. (C) Normalized spectrally integrated emission for Cy5 fluorescence (690 – 700 nm) and Cy5 lasing (710 – 740 nm) under 36.7 μJ/mm^2 excitation. Each data point represents the normalized emission under excitation of 20 pulses. (D) The corresponding Cy5 laser emission spectrum for the sum of 1st-20th pulses and the sum of 81st-100th excitation pulses.

Photostability of the Qdot-Cy5 conjugate

We further performed a photostability experiment of FRET lasing with the QD-Cy5 sample. Fixing pump intensity at 176 μJ/mm², we recorded the lasing spectrum and derived lasing and fluorescence intensities from different spectral regions over 49 consecutive excitation pulses (Fig. 2.12(A) and (B)). After 49 excitation pulses, fluorescence intensity experienced a decrease of less than 20% while a 50% decrease was recorded for lasing emission. This result is consistent with the non-linear nature of laser mechanism.[83] The relatively rapid photo-bleaching of Cy5 laser emission is due to the high excitation intensity used in the experiment. In contrast, when a lower excitation intensity (36.7 μJ/mm²) was applied, significantly improved photostability was observed (Fig. 2.12(C) and (D)). In practice, the laser does not need to be operated in high excitation intensity for biosensing. In fact, single pulse excitation at an intensity slightly above the threshold is sufficient.

2.4.3 Theoretical analysis and discussion

In general, the equations for the acceptor laser are given as follows: [84]

$$\frac{dn_d}{dt} = I_p \sigma_{d,a}(N_d - n_d) - \frac{n_d}{\tau_d} - k_F n_d \qquad (2.13)$$

$$\frac{dn_a}{dt} = k_F n_d - \frac{n_a}{\tau_a} \qquad (2.14)$$

$$\frac{dq_a}{dt} = \frac{c}{m}\sigma_{a,e}(\lambda_L)n_a - \frac{c}{m}\sigma_{a,a}(\lambda_L)(N_a - n_a) - \frac{q_a}{\tau_{cavity}} \qquad (2.15)$$

where n_d and n_a are the donor and acceptor concentration in the excited state, respectively. N_d and N_a are the total concentration for the donor and acceptor, respectively. q_a is the photon number density in the cavity emitted by the acceptor. τ_d, τ_a, and τ_{cavity} are the lifetime for the donor, the acceptor, and the photons in the cavity mode. τ_{cavity} is related to the empty cavity Q-

factor, Q_0, by $\tau_{cavity} = \dfrac{Q_0 \lambda}{2\pi c}$. c is the light speed in vacuum. k_F is the energy transfer rate from the donor to the acceptor. $\sigma_{d,a}$, $\sigma_{a,e}$, and $\sigma_{a,a}$ are the donor absorption cross section, the acceptor emission cross section, and the acceptor absorption cross section, respectively. I_p is the pump intensity. m is the refractive index of the cavity mode. λ_L is the lasing wavelength. Eqs. (2.13) and (2.14) describe the donor and acceptor concentrations in the excited state, respectively, whereas Eq. (2.15) describes the number density of photons inside the cavity. Under the steady-state condition, we have

$$n_d = \frac{I_p \sigma_{d,a}}{I_p \sigma_{d,a} + 1/\tau_d + k_F} N_d \qquad (2.16)$$

$$n_a = \tau_a k_F n_d \qquad (2.17)$$

$$\sigma_{a,e}(\lambda_L) n_a - \sigma_{a,a}(\lambda_L)(N_a - n_a) - \frac{2\pi n}{Q_0 \lambda_L} = 0 \qquad (2.18)$$

Eq. (2.18) leads to the threshold condition for the acceptor concentration, $n_{a,th}$, which is

$$\gamma_{th} = \frac{n_{a,th}}{N_a} \approx \frac{\sigma_{a,a}(\lambda_L) N_a + 2\pi m /(Q_o \lambda_L)}{N_a \sigma_{a,e}(\lambda_L)}. \qquad (2.19)$$

For the case where QDs are used as the donor, Eq. (2.13) may need to be modified to reflect multi-exciton excitation and extremely fast relaxation processes of multi-excitons,[85,86] which are on the order of tens to hundreds of pico-second, shorter than the energy transfer time ($1/k_F$) of a few nano-second. To further understand the energy transfer between the QD donor and the dye acceptor, we chose QDot 655 and Alexa Fluor 680 (AF680) as another donor/acceptor pair. Based on the spectrum shown in Fig. 2.13, the Förster distance of QDot 655-Cy5/QDot 655-AF680 pair can be calculated as 8.2 nm/7.9 nm, which means QD-Cy5 has
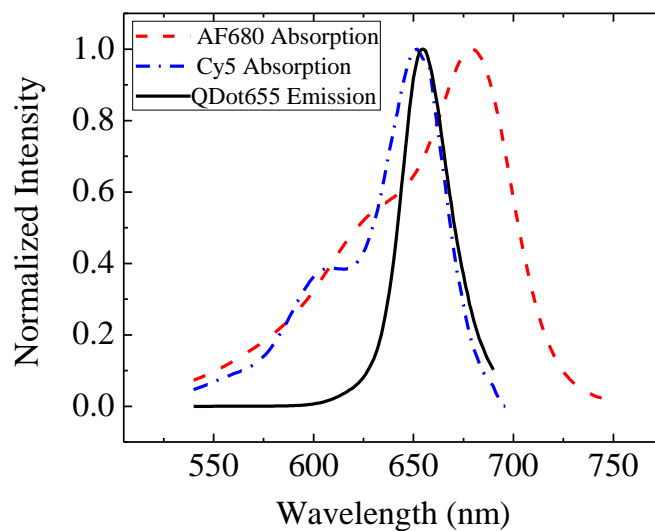
Figure 2.13 Emission/absorption spectrum for QDot 655, Cy5, and AF680.
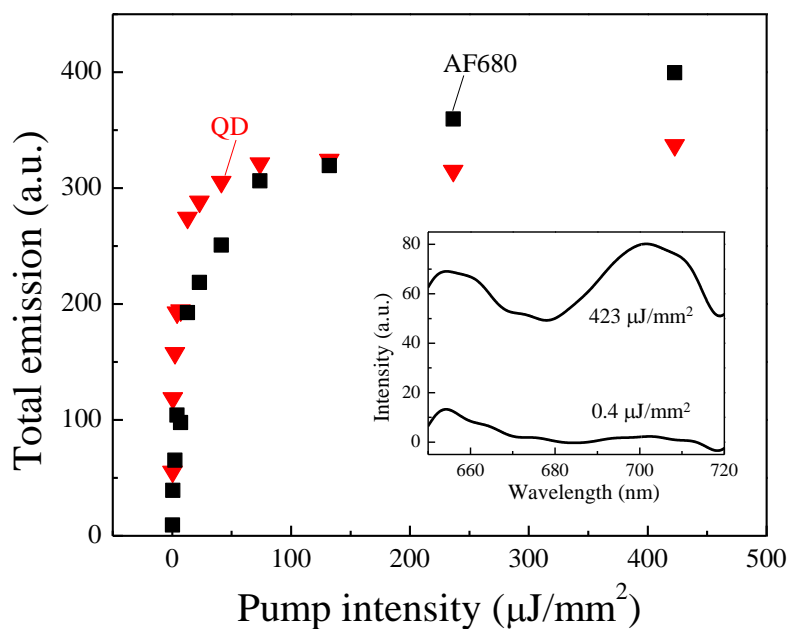
Figure 2.14 Spectrally integrated fluorescence of QD and AF680 from QD-AF680 conjugates for various pump intensities at 450 nm. Each data point is recorded under single pulse excitation. Spectral integration takes place in the range of 650 – 655 nm for QD emission and of 700 – 705 nm for AF680. Inset: emission spectra of QD-AF680 conjugation at different pump intensities. Spectral curves are smoothed with a low pass filter with a cutoff at 0.1 Hz.

higher intrinsic FRET transfer rate than QD-AF680. The difference is mainly due to the smaller spectral overlap between QDot 655 and AF680. Therefore, only distinct fluorescent peaks of the donor and the acceptor were observed in the QD-AF680 pair using exactly the same experimental conditions as in the QD-Cy5 case, as plotted in the inset of Fig. 2.14, which allows us to study the energy transfer between the QD donor and dye acceptor without interference from the acceptor laser emission.

Fig. 2.14 plots the fluorescence from both QDot 655 and AF680 measured simultaneously with various pump intensities. Initially, the fluorescence from both QDot 655 and AF680 increases concomitantly and is linearly proportional to the pump intensity, indicating that more QDs are excited through direct excitation and more AF680 are excited through FRET. Between 10 and 100 μJ/mm^2, the QD emission starts to show certain degree of saturation, *i.e.*, its intensity still grows with the increased pump intensity, but with a smaller slope. Accordingly, the AF680 emission has a similar pattern of saturation. When the pump intensity is above 100 μJ/mm^2, the QD emission completely levels off, suggesting that no more photons can be emitted by the QDs, despite the increased pump intensity. Meanwhile, the AF680 increases with a very slow slope. This slight increase in AF680 emission results from the small direct excitation of AF680 at 450 nm pump whereas the emission of AF680 through the energy transfer from the QDs should completely saturate, as suggested by the QD emission. Indeed, after the correction for the emission from the direct excitation, the AF680 emission exhibits the corresponding saturation behavior that follows that in the QD emission (Figure 2.15). Direct excitation expressed as $I_{direct} = AN_{AF680}\sigma_{AF680}(450nm)q_{AF680}$is removed from the AF 680 emission in the corrected emission peak. In the formula, A is the system collection coefficient. N_{AF680} is the

total concentration of AF680. σ_{AF680} and q_{AF680} are the absorption cross section and quantum yield, respectively. A can be derived from the slope of the QD emission.
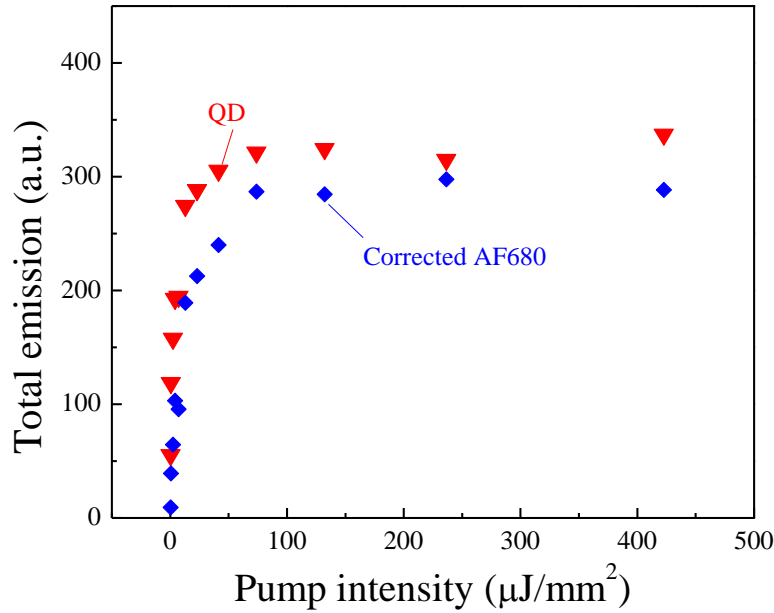
Figure 2.15 Fluorescence intensity of AF680 in QD-AF680 sample corrected for direct excitation in QD-AF680 sample.

The detailed microscopic mechanism of FRET using QDs as the donor can be understood as follows. Upon excitation of multiple excitons, they relax very rapidly down to biexciton and then single exciton through the non-radiative recombination.[85,86] As those relaxation processes are very fast in comparison with the radiative decay rate, they do not contribute to photon generation. The QD fluorescence emission in Fig. 2.14 comes mainly from biexciton and single exciton, whose radiative decay rates are comparable to the corresponding non-radiative rates. Both biexciton and single exciton are able to transfer excitation energy to the acceptor dye.[80] The energy transfer efficiency for biexciton and single exciton can be written as $\tau_{FRET}^{-1}/(\tau_{FRET}^{-1} + \tau_x^{-1})$, where τ_x is the biexciton (x=2) and single exciton (x=1) lifetime and τ_{FRET} is the energy transfer time. However, since the biexciton lifetime (<2 ns) [80] is much shorter

than that of single exciton (~34 ns), and the energy transfer time for biexciton and single exciton is similar [80], the emission from AF680 comes mainly from the energy transferred from single excitons. The same argument is valid for the QD-Cy5 system, whose energy transfer time is 4.4 ns. Consequently, n_d in Eq. (2.14) should refer to the concentration of single excitons. At high pump intensity (>100 μJ/mm²), we can assume that the concentration of single excitons is the same as the QD concentration. At relatively low pump intensity (<100 μJ/mm²), the fractional single exciton concentration can be deduced by comparing the AF680 fluorescence at low pump intensity with the saturation fluorescence. Based on the above discussion, for the QD-Cy5 conjugates, the lasing threshold of 14 μJ/mm² corresponds to n_d of 2 μM (=3.3 μM x 0.6, where 0.6 is the ratio of AF680 fluorescence between 14 μJ/mm² and 100 μJ/mm²). Using τ_a = 1 ns for Cy5 and k_F = (4.4 ns)$^{-1}$ in Eq. (2.17), we arrive at n_a = 0.45 μM and γ =n_a/N_a=1.6%. At high pump intensity, the Cy5 laser emission saturates beyond 100 μJ/mm², consistent with the QD saturation behavior obtained by fluorescence measurement using QD-AF680.

To further examine the γ value, we performed the laser measurement using Cy5-DNA under exactly the same condition as in the QD-Cy5 case, except that the pump wavelength was moved to 500 nm where Cy5 has much higher absorption than at 450 nm. Fig. 2.16 shows that the lasing emission can be achieved with a threshold of approximately 13 μJ/mm². For direct excitation, the concentration of Cy5 at the excited state can be calculated by

$$n_a = \frac{I_p \sigma_{a,a}(500nm)}{I_p \sigma_{a,a}(500nm) + 1/\tau_a} N_a.$$

(2.20)

Using $\sigma_{a,a}$ = 0.31x10^{-16} cm² at 500 nm, τ_a = 1 ns, and I_p = 6.5x10^{14} cm^{-2} ns^{-1}, we have $\gamma = n_a/N_a$ = 2.0%, which has the same level of Cy5 excitation as in the QD-Cy5 conjugates. Furthermore, in Eq. (2.19), using $\sigma_{a,e}$ = 2.5x10^{-16} cm², Q_0 = 2x10^6, λ_L = 730 nm and ignoring the first term (*i.e.*,

$\sigma_{a,a}N_a$, as it is small compared to the second term related to the cavity loss), we obtain the lasing threshold condition of $n_{a,th} = 0.41$ μM and $\gamma_{th} = 1.4\%$.

From our experimental result and theoretical analysis, we conclude that there are two major strategies to achieve a FRET laser with QD as the donor. The first one is to increase the FRET energy transfer rate k_F (see Eq. (2.17)). This can be fulfilled by (1) choosing a good FRET pair that the emission band of QD has significant overlap with the acceptor absorption band; (2) carefully tuning the distance between the core of the quantum dots and the acceptor to enable sufficient energy transfer; (3) increasing the labeling ratio. The second strategy is to suppress the non-radiative Auger recombination rate of multi-exciton states of QDs to enable FRET from higher-order exciton states. For this purpose, QDs with better surface chemical designs or type II QDs can be used [87-90] to further exploit the large absorption cross section of QDs in FRET lasing.
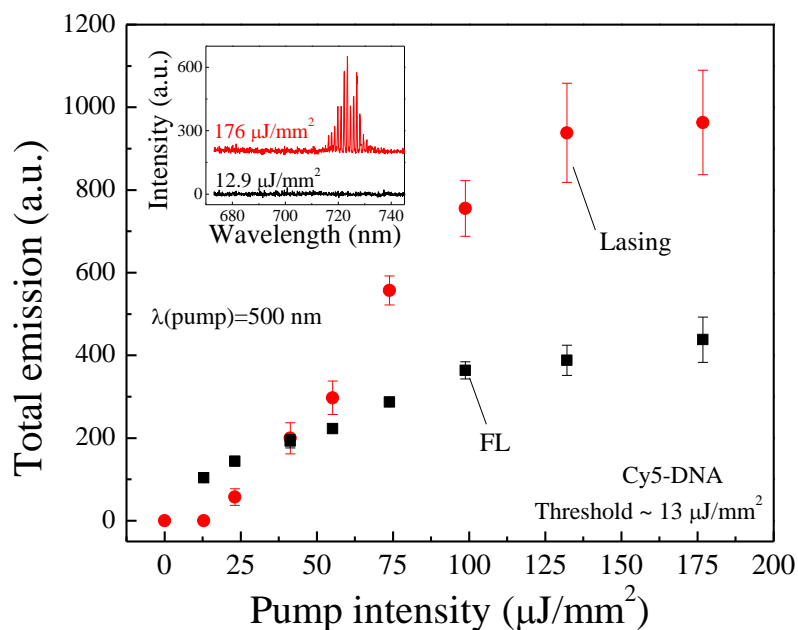
Figure 2.16 Spectrally integrated emission versus pump intensity for Cy5 when pumped at 500 nm. Spectral integration takes place in the range of 715-735 nm for lasing and 680-700 nm for fluorescence (FL). Inset: emission spectrum of Cy 3 pumped at 176 μJ/mm². The lasing threshold for Cy5 is approximately 13 μJ/mm². Concentration of Cy5 was 30 μM. Experimental conditions were the same as in Fig. 2.11.

In summary, we investigated the capability of QDs as the donor for optofluidic FRET laser operation and successfully achieved lasing from acceptor molecules in a QD-Cy5 system when excited at 450 nm where Cy5 has negligible absorption by itself, thus significantly extending the excitation spectral range for the acceptor. The lasing threshold was approximately 14 μJ/mm^2. The power-dependent fluorescence and laser studies suggest that the excitation of the acceptor comes mainly from the energy transferred from single excitons in QDs. We further reveal the similarities and dissimilarities between organic dyes and QDs as the donor and point out the methods to improve the optofluidic FRET laser performance when using QDs as the donor.

2.5 **Conclusion**

In this chapter, experimental exploration of FRET lasers using different biological/biochemical molecules as gain medium is shown. Corresponding theoretical analysis is presented addressing the specific properties of the material used. A more general theoretical analysis of the FRET laser can be found in Ref. 84. By setting up a set of rate equations for the donor and acceptor molecules as well as photon numbers corresponding to donor and acceptor lasing wavelength respectively, this paper numerically simulated the dynamics of a FRET laser system and revealed that intra-cavity detection can result in a 100x enhancement of the FRET signal by carefully choosing the optical cavity Q factor and the excitation intensity. The lasing characteristics of the tetrahedron-based FRET laser was also simulated in this paper, showing agreeing results with the experiment. The protein FRET laser can also be verified through the model provided. Combining the simulation and the experimental results, we foresee a great potential in ultra-sensitive biochemical analyses and bio-controlled lasers using the FRET optofluidic laser scheme.

CHAPTER 3: **Optofluidic biolasers with a single molecular layer of gain**

3.1 **Introduction**

      To date, nearly all optofluidic lasers are demonstrated with the gain medium dispersed in bulk solution. Consequently, the entire lasing mode present in liquid interacts with the gain medium. For example, for the optofluidic lasers based on Fabry-Pérot cavities,[4,91,92] liquid droplets[13,83] and distributed feedback cavities,[93] up to 90% of the lasing mode is interacting with the gain medium. For those based on evanescently coupled ring resonators and photonic crystals, the entire evanescent field (characteristic decay length of approximately 100 nm) resides in the gain medium. Accordingly, bio-control of and bio-analysis with the optofluidic laser need to be accomplished in bulk solution.

      In this chapter, optofluidic lasers with a single molecular layer of gain medium placed at the interface of a solid substrate and liquid is presented. The motivation behind this work is three-fold.

      First, lack of precise control of the gain medium position when gain molecules are distributed in bulk solution may significantly deteriorate the lasing performance. For example, in the evanescently coupled ring resonator case, only 0.1-1% of gain molecules in bulk solution participates in lasing action. The rest simply contributes to the fluorescence background that affects the quality of the laser emission spectrum or the sensitivity of the bioanalysis.[6,7,65,93] Intentionally placing the gain medium only at the cavity surface in this case will enable maximal

light-matter interaction, which will not only improve the lasing efficiency and threshold, but also reduce fluorescence background and enable better control of the laser.

Second, the optofluidic laser has been used for bioanalysis,[2,6,7,61,65] which complements the conventional fluorescence based technologies. There are two generic schemes in fluorescence based detection - bulk solution detection (such as detection with molecular beacons[94] and intercalating dyes,[95] in which biomolecules move freely in bulk solution) and surface detection (such as detection and analysis with microbeads,[96] in which biomolecules are immobilized or captured on a solid/liquid interface). While the optofluidic laser has been quite successful in bulk solution based detection,[6,7,65] its surface based detection capability has not been explored. Demonstration of an optofluidic laser with a single molecular layer on the solid/liquid interface would be a critical step towards a variety of studies analogous to those using fluorescence.

Third, the laser with a single molecular layer of gain, which is similar to a semiconductor laser such as a VCSEL (vertical-cavity surface-emitting laser) that consists of a single quantum-well layer as the gain medium,[97,98] is fundamentally interesting, as it provides a means to ultimately test the capability and limit of a laser. Indeed, lasing from a thin fluorophore-doped film coated on the resonator surface using various coating methods (*e.g.*, spin-, dip-, or drop-coating) has recently been demonstrated.[99-101] However, those methods result in a coating thickness of approximately 100 nm, equivalent to hundreds of molecular layers. Lasing from a single molecular layer of gain has never been realized.

As a brief overview, using surface immobilization biochemistry, a single layer (or even a sub-layer) of gain molecules was attached on the surface of an optical fiber, whose circular cross section serves as a ring resonator (Fig. 3.1(A)). The whispering gallery modes (WGMs) supported by the ring resonator interact with the gain molecules and provide the optical feedback

for lasing through evanescent wave coupling. Strong lasing emission from enhanced green fluorescent protein (eGFP) and dye-labeled bovine serum albumin (BSA) was obtained with a surface density of approximately 10^{12} /cm^2. It was also shown that the lasing emission can be controlled by the energy transfer mechanism via DNA hybridization on the fiber surface.
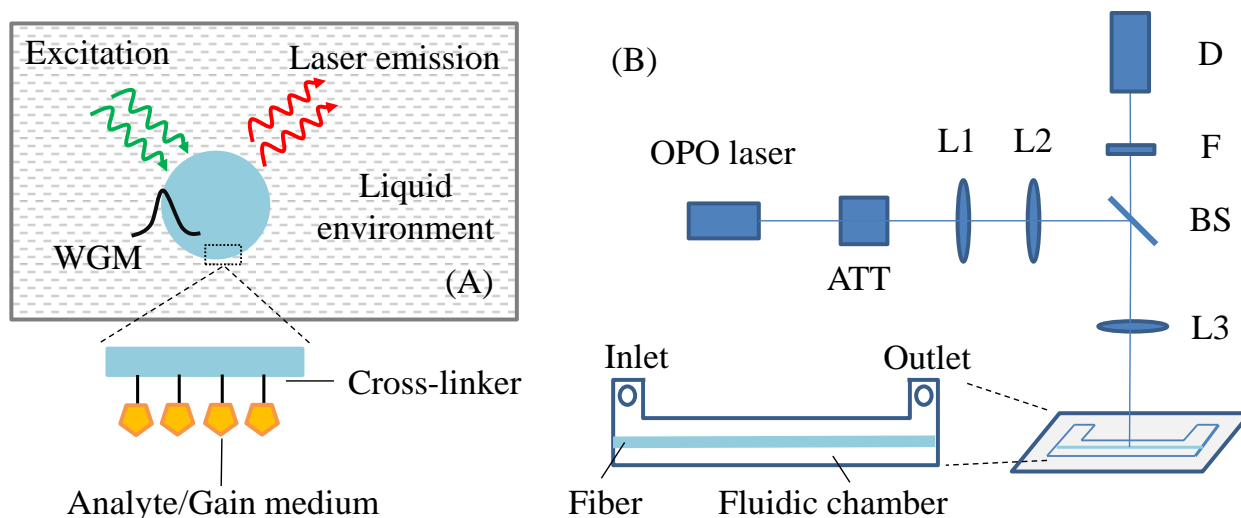
Figure 3.1 (A) Cross-sectional view of the ring resonator laser in the liquid environment. WGM: whispering gallery mode. Inset, illustration of a single molecular layer of gain medium attached on the fiber surface through cross-linking chemistry. (B) Schematic of the experimental setup. OPO: optical parametric oscillator; ATT: attenuator; L1/L2/L3: lenses; BS: beam splitter; F: filter; D: detector. Inset, top view of the fluidic chamber. Chamber dimension: 35 mm ×3 mm × 0.5 mm.

3.2 Experimental

3.2.1 The surface modification for molecule binding

An optical fiber (SMF-28, 125 μm in diameter) was chosen to serve as the ring resonator in this work due to its easy preparation, predictable WGM evanescent field distribution near the surface and consistent quality along the axis.[102] The Q-factor of this type of ring resonator exceeds 10^6.[25] To functionalize the ring resonator surface, the fiber was first sonicated in acetone, ethanol and deionized (DI) water in series, each for 15 minutes. Then the cleaned fiber was immersed in HCl/ethanol (v:v=1:1) for 30 minutes. After rinsed in DI water and dried under air

flow, the fiber was silanized with (3-aminopropyl)-trimethoxysilane (3-APTMS, 5% in methanol) for 30 minutes and rinsed with ethanol. Finally, the fiber was cured at 110 °C overnight and stored in a refrigerator at 4 °C for future use. For subsequent attachment of a single layer of gain molecules on the fiber surface, the silanized fiber was activated with freshly prepared homofunctional amine-to-amine cross-linker bis(sulfosuccinimidyl) suberate (BS^3) (0.1 mg/mL in phosphate-buffered saline (PBS)) for 30 minutes and rinsed with PBS before incubation with the molecules of interest.

3.2.2 The optical setup

The optofluidic laser setup is illustrated in Fig. 3.1(B). The fluidic chamber was made of PDMS (Polydimethylsiloxane). It had an inlet/outlet for liquid delivery. The fiber was suspended inside the chamber with no contact with the chamber wall. A confocal setup was used to excite the ring resonator with a pulsed optical parametric oscillator (OPO) (repetition rate: 20 Hz, pulse width: 5 ns) and collect the laser emission. The emission light was sent to an Horiba iHR 550 spectrometer for analysis.

3.3 Results

3.3.1 Lasing from a single layer of GFPs

The lasing capability of a single layer of eGFP on the surface was first demonstrated. The eGFP sample was purchased from BioVision. Each eGFP has a molecular weight of 32.7 kDa, a shape of cylinder with a length of 4.2 nm and diameter of 2.4 nm and a single emission center. The BS^3 activated fiber was inserted into the chamber, which was later filled with 1 μM eGFP in PBS. After 30 minutes of incubation, which covalently bound eGFP molecules to the resonator surface (inset of Fig. 3.2(A)), 1 mL PBS solution was flowed through the chamber to wash away

the unbound molecules. As a result, only those eGFPs that were cross-linked by BS^3 remain on the surface and formed a single or an even sub-layer (considering only partial surface coverage) of gain molecules.
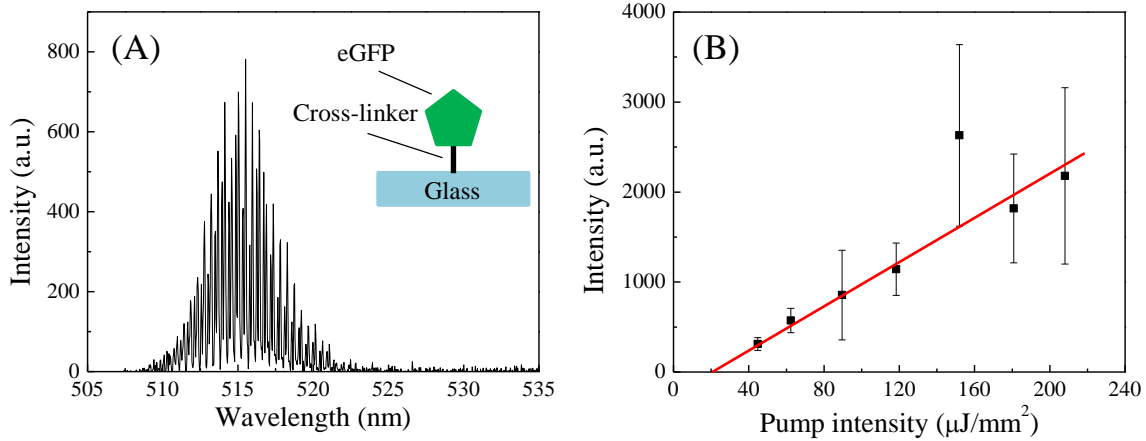
Figure 3.2 Lasing characteristics of a single layer of eGFP. (A) Lasing spectrum. Pump intensity is approximately 120 μJ/mm^2 per pulse. Excitation wavelength: 488 nm. (B) Spectrally integrated eGFP laser output as a function of pump intensity. Spectral integration takes place between 507 nm and 542 nm. Lasing threshold is approximately 23 μJ/mm^2 per pulse. Solid line is the linear fit above the threshold. Error bars are obtained with 3 measurements.

Figure 3.2(A) shows the eGFP lasing spectrum with multiple lasing peaks due to the multi-mode nature of the WGMs. As nearly all gain molecules participate in the lasing action, the fluorescence background is negligible. The lasing threshold derived from Fig. 3.2(B) is approximately 23 μJ/mm^2. These results demonstrate that even a single (or sub-) layer of gain molecules is sufficient for lasing. The lasing threshold is on par with that for the bulk solution based optofluidic laser using much higher concentrations of eGFP (typically >10 μM).[3,4]

Theoretical analysis is carried out to understand the laser process. Lasing threshold can be written as:

$$I_{th} = \frac{\gamma}{\Gamma - \gamma},$$ (3.1)

where Γ is the fraction of gain molecules that participate in lasing action ($\Gamma = 1$ in the eGFP case). γ is the fraction of gain molecules in the excited state at the threshold,

52

$$\gamma = \frac{A_1}{A_2} = \frac{2\pi m_1 L}{\lambda_0 \eta Q_0 \sigma_e(\lambda_0)A}, \qquad\qquad (3.2)$$

where A_1 is the surface density of the excited molecules. A is the total surface density. η is the fraction of mode energy in the evanescent field. $\sigma_e(\lambda_0)$ is the eGFP emission cross section at lasing wavelength. m_1 is the effective refractive index of the circulating optical mode, Q_0 the quality factor of the cavity mode. L is the penetration depth of the evanescent field. Thus, A/L is the effective bulk solution concentration. The surface density of eGFP for a fully packed surface is about $10^{13}/cm^2$. Considering the steric hindrance issues, the surface density of eGFP is estimated to be on the order of $10^{12}/cm^2$, which is similar to the maximal surface coverage of proteins cross-linked on a ring resonator surface obtained in optical label-free measurement. Assuming 100 nm as the evanescent field penetration depth, the effective local concentration of eGFP (*i.e.*, *A/L*) can be calculated to be approximately 170 μM. Therefore, despite low concentration (1 μM) used in the experiment, surface immobilization process results in a much higher local concentration, which is critical for laser operation. Accordingly, $\gamma = 4.3\%$, similar to that obtained by other dye laser systems (~1%-10%). [17,25]

3.3.2 Lasing from dye-labeled BSA through specific binding

In the above experiment, the eGFPs were attached to the surface non-specifically. It was also demonstrated that the lasing can be achieved from a single layer of molecules attached to the surface specifically. To achieve specificity, anti-BSA and dye-labeled BSA (Alexa Fluor®-488) (both from Life Technologies) were used. The BS^3 activated fiber was first incubated with 3 μM anti-BSA PBS solution for 30 minutes. After rinsing by PBS buffer, 1 μM BSA was injected into the chamber and incubated for another 30 minutes. Finally, the fiber was rinsed by and filled with PBS buffer before laser tests. Figure 3.3(A) is the lasing spectrum of a control fiber on

which BSA molecules were cross-linked non-specifically as in the eGFP case. Figure 3.3(B) shows the lasing spectrum of specifically bound BSA through anti-BSA. Strong laser emission is observed in both cases. However, specifically bound BSA requires approximately ten times higher pump intensity to achieve the same emission intensity. The difference can be accounted for by the reduced coverage of gain medium on the surface due to multiple immobilization steps, steric hindrance, and non-functional anti-BSA on the surface. Based on the theoretical analysis, we can compare Fig. 3.3(A) and (B) to estimate the BSA/anti-BSA binding. The coverage of BSA through anti-BSA binding is calculated to be 14% of that through direct non-specific crosslinking as shown in the theoretical analysis section.
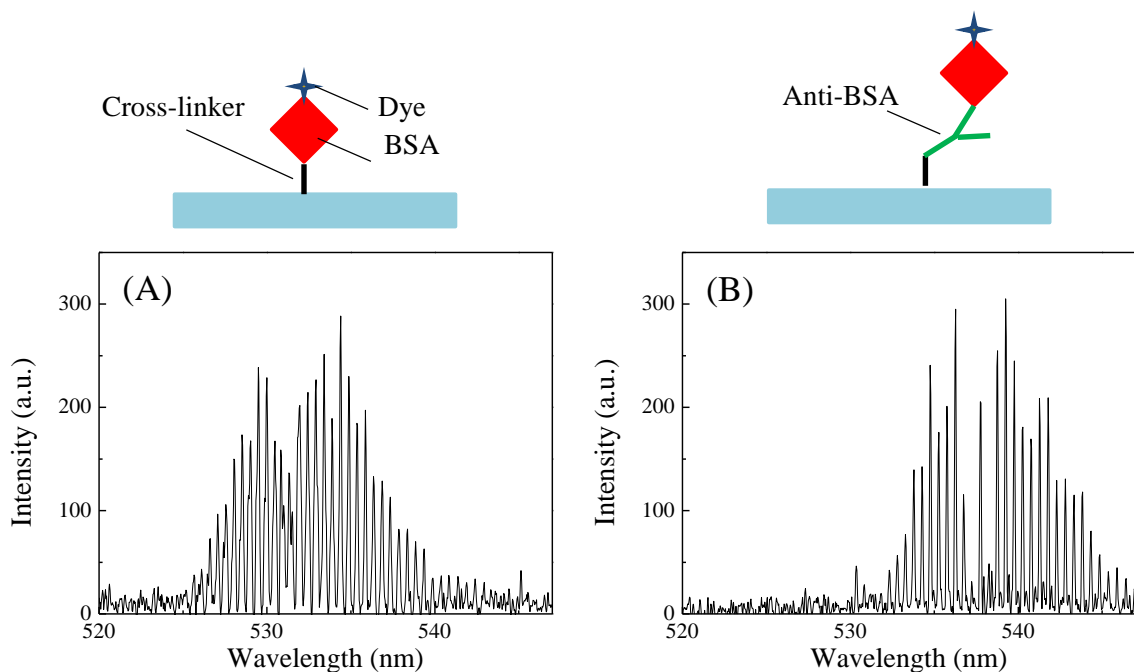
Figure 3.3 Lasing spectra from Alexa Fluor®-488 labeled BSA. (A) BSA is immobilized on the ring resonator surface using a cross-linker. Pump intensity: 100 μJ/mm^2 per pulse. Excitation wavelength: 488 nm. (B) BSA is immobilized on the ring resonator surface via binding with anti-BSA. Pump intensity: 1000 μJ/mm^2 per pulse. Excitation wavelength: 488 nm. Cartoons above the figures illustrate the corresponding immobilization schemes.

3.3.3 FRET modulated lasing

It was further demonstrated that lasing through a single layer of gain medium can not only be achieved but also be tuned by the fluorescence resonance energy transfer (FRET) mechanism as in the bulk solution case,[5,6] which is critical to biological and biomedical applications, as well as photonic devices. DNA was used for this demonstration due to its simple and robust hybridization mechanism. Two 40 bases long single-stranded DNA sequences were purchased from Integrated DNA Technologies. One was designated as probe DNA, which was biotinylated at the 5' end and labeled with Cy3 (donor) at the 3' end. The other was designated as the target DNA, which was complementary to the probe DNA and labeled with Cy5 (acceptor) at the 5' end (Table 3.1). The DNA stock solutions were prepared by dissolving the corresponding samples in 500 µL 1X TAE (Tris-Acetate-EDTA)/12.5mM $MgCl_2$, which were further diluted in subsequent experiments. As in the previous experiments, the fiber was activated by BS^3 first. Then 0.5 mg/mL streptavidin in PBS was introduced into the chamber and incubated with the fiber for 30 minutes, followed by sequential PBS, DI water and TAE/$MgCl_2$ buffer rinsing. Finally, 1 µM probe DNA solution was injected and incubated for 30 minutes before TAE/$MgCl_2$ buffer rinsing. Through the well-known biotin-streptavidin interaction, the probe DNA and hence Cy3 molecules were attached to the ring resonator surface.

Figure 3.4(A) shows the typical Cy3 lasing spectrum, as expected. Then, 10 nM target DNA solution was injected into the chamber and incubated for 20 minutes, followed by TAE/$MgCl_2$ rinsing. Due to the hybridization of the probe and target DNAs, a fraction of Cy3 molecules on the surface were brought to close proximity of Cy5, resulting in highly efficient (nearly 100%) energy transfer between Cy3 and Cy5 that quenches Cy3 emission. As shown in Fig. 3.4(B), the laser emission from Cy3 is significantly reduced compared to Fig. 3.4(A),
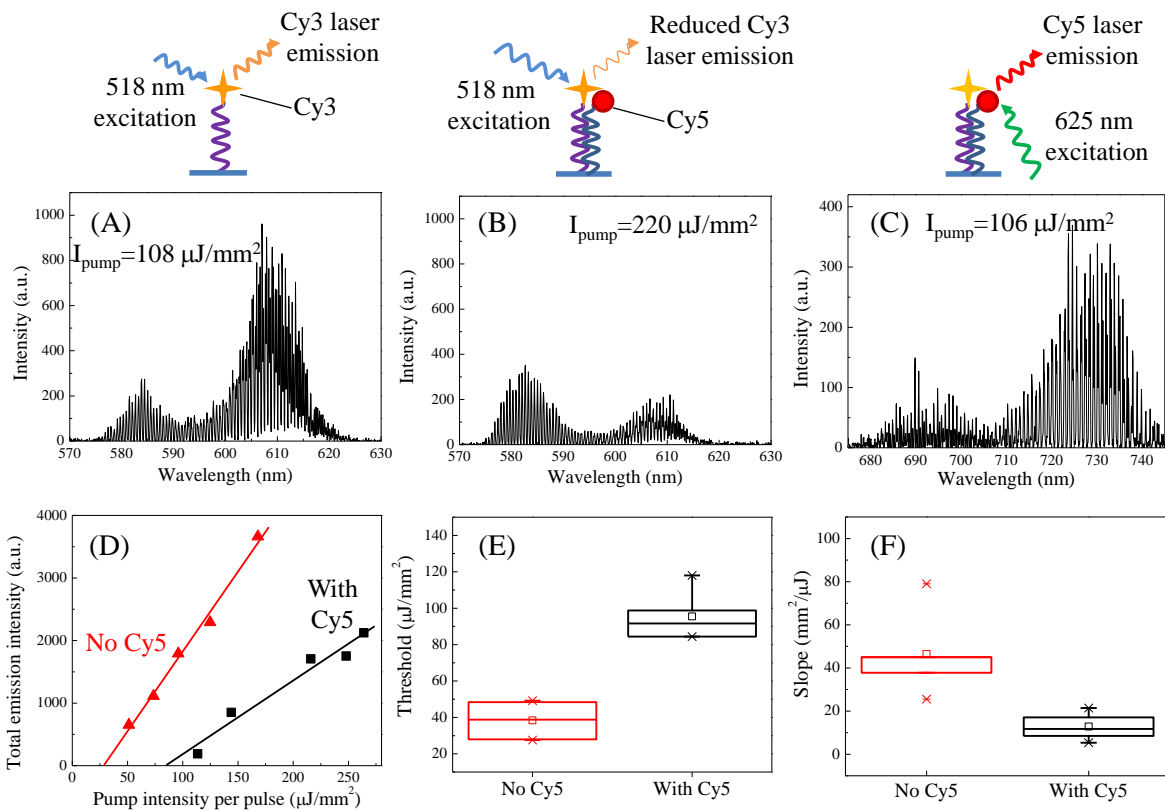
Figure 3.4 Comparison of donor (Cy3) laser emission in the absence and presence of acceptor (Cy5). (A) Laser emission from Cy3 in the absence of Cy5. Pump intensity: 108 μJ/mm^2 per pulse. Excitation wavelength: 518 nm. (B) Laser emission from Cy3 in the presence of Cy5. Pump intensity: 220 μJ/mm^2 per pulse. Excitation wavelength: 518 nm. (C) Laser emission from Cy5. Pump intensity: 106 μJ/mm^2 per pulse. Excitation wavelength: 625 nm. Cartoons above the (A)-(C) illustrate the corresponding immobilization schemes. (D) Spectrally integrated Cy3 laser output as a function of pump intensity in the absence (triangles) and presence (squares) of Cy5. Spectral integration takes place between 563 nm and 637 nm using the laser emission spectra similar to those shown in (A) and (B). Solid lines are the curve fit above the respective thresholds, showing a threshold of 28 μJ/mm^2 and 84 μJ/mm^2, and a lasing slope of 25 mm^2/μJ and 12 mm^2/μJ, respectively, for Cy3 laser in the absence and presence of Cy5. (E) and (F) Lasing threshold and slope obtained with the corresponding curves similar to those plotted in (D). Error bars are generated with 5 measurements.

Probe DNA	5' - Biotin - AC AAC AAA GAA CAA ATA TAC ATA TAT GAT ATA ACA ACA AA - Cy3 - 3'
Target DNA	5' - Cy5 - TT TGT TGT TAT ATC ATA TAT GTA TAT TTG TTC TTT GTT GT -3'

Table 3.1 Modifications and sequences of the 40-base long single-stranded DNAs

56

despite doubled pump intensity. For further Cy3 lasing suppression, 50 nM Cy5-labeled target DNA was introduced. No Cy3 lasing could be observed even with the pump intensity as high as 1000 μJ/mm². The presence of the target DNA (and hence Cy5) on the surface can be directly verified by Cy5 lasing in Fig. 3.4(C) when Cy3 lasing is suppressed. Quantitative comparison of Cy3 lasing characteristics before and after hybridization with the 10 nM target DNA is plotted in Fig. 3.4(D). Significant differences in lasing threshold and efficiency are evident (Figs. 3.4(E) and (F)), attesting to the tuning capability of the laser with a single layer of gain on the surface. Based on the 3 times difference in Cy3 lasing threshold before and after 10 nM target DNA incubation, it can be calculated that 64% of the immobilized probe DNA is hybridized with the target DNA as shown later.

3.4 **Theoretical study**

3.4.1 Theoretical framework

Population inversion condition states that at the lasing threshold the round-trip emission should be equal to the sum of the round-trip cavity loss and the round-trip loss caused by molecular absorption.

Referring to Fig. 3.5, the cavity round-trip energy loss is determined by:

$$L_{cavity} = I \cdot \frac{2\pi m_1}{\lambda_0 Q_0} \cdot (2\pi R) = [\int \varepsilon_0 \varepsilon(r,\theta,z) E^2(r,\theta,z) r dr d\theta dz] \cdot \frac{2\pi m_1}{\lambda_0 Q_0} \cdot (2\pi R), \quad (3.3)$$

where I is the total energy in the WGM. $\varepsilon(r,\theta,z)$ and $E(r,\theta,z)$ are the dielectric constant and WGM electric field. R and m_1 is the resonator radius and resonator effective refractive index, respectively. λ_0 is the lasing wavelength in vacuum. Q_0 is the resonator Q-factor. Assuming that the dielectric constant and the electric field have only radial dependence, Eq. (3.3) becomes:

$$L_{cavity} = I \cdot \frac{2\pi n_1}{\lambda_0 Q_0} \cdot (2\pi R) = [2\pi \int \varepsilon_0 \varepsilon(r) E^2(r) r dr \cdot \int dz] \cdot \frac{2\pi n_1}{\lambda_0 Q_0} \cdot (2\pi R), \quad (3.4)$$

The round-trip energy loss due to molecular absorption is given by:

$$L_{absorption} = 2\pi R \int \varepsilon_0 \varepsilon(r) E^2(r) \rho(r,\theta,z) \sigma_a(\lambda_0) r dr d\theta \cdot \int dz, \quad (3.5)$$

where $\rho(r,\theta,z)$ is the density of molecules. $\sigma_a(\lambda_0)$ is the molecule's absorption cross section at the lasing wavelength. For molecules attached to the resonator surface, we have

$$\rho(r,\theta,z) = A(\theta,z) \cdot \delta(R) = A\delta(R), \quad (3.6)$$

where $A(\theta,z)$ is the molecular surface density. The dependence on θ and z can be removed if we assume a homogenous surface distribution. Similarly, the emission of the molecules can be given as:

$$Emission = 2\pi R \int \varepsilon_0 \varepsilon(r) E^2(r) \rho(r,\theta,z) \sigma_e(\lambda_0) r dr d\theta \cdot \int dz, \quad (3.7)$$

where $\sigma_e(\lambda_0)$ is the emission cross section at the lasing wavelength.

The corresponding population inversion condition for a four-energy-level laser system can be written as:[7,25,70]

$$\eta(A_1/L)\sigma_e(\lambda_0) = \eta(A/L - A_1/L)\sigma_a(\lambda_0) + \frac{2\pi n_1}{\lambda_0 Q_0}, \quad (3.8)$$

where A_1/L is the surface density of the molecules in the excited state normalized to the intensity decay length of the WGM in the liquid, which is the effective concentration of the molecules.

$$\eta = \frac{2\pi R L \cdot \varepsilon_0 (m_2 E_R)^2 \cdot \int dz}{2\pi \int \varepsilon_0 \varepsilon(r) E^2(r) r dr \cdot \int dz} = \frac{(m_2 E_R)^2 R L}{\int \varepsilon(r) E^2(r) r dr} \approx \frac{(m_2 E_R)^2 L}{\int \varepsilon(r) E^2(r) dr}, \quad (3.9)$$

where m_2 is the refractive index of the surrounding liquid. E_R is the WGM electric field at the ring resonator surface. η is the fraction of the WGM energy in the evanescent field.

According to the laser theory, the lasing threshold, I_{th}, is determined by:

$$I_{th} = \frac{\gamma}{\Gamma - \gamma}, \qquad (3.10)$$

where $\gamma = A_1/A$ is the fraction of gain molecules in the excited state at the lasing threshold. Γ is the fraction of gain molecules that participate in lasing action. Referring to Eq. (3.8),

$$\gamma = \frac{\sigma_a(\lambda_0)}{\sigma_a(\lambda_0) + \sigma_e(\lambda_0)}(1 + \frac{2\pi m_1 L}{\lambda_0 \eta Q_0 \sigma_a(\lambda_0) A}) \approx \frac{2\pi m_1 L}{\lambda_0 \eta Q_0 \sigma_e(\lambda_0) A}. \qquad (3.11)$$
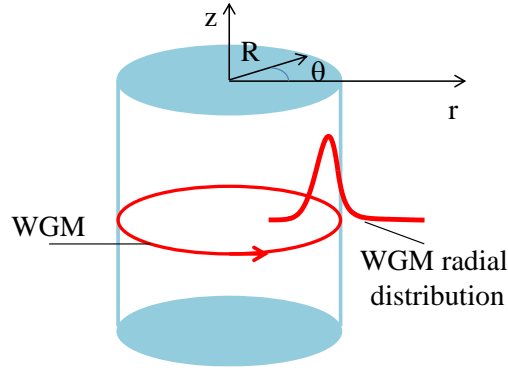
Figure 3.5 Illustration of the WGM and the parameters used in theoretical analysis.

3.4.2 Surface coverage ratio estimation

First, we estimate the BSA surface density ratio between specific and non-specific cases. According to the laser theory, the laser output power, I_{output}, is linearly proportional to the pump intensity, I_{pump}, above threshold:

$$I_{output} \propto I_{pump}/I_{th} - 1 \qquad (3.12)$$

Since the output in Fig. 3.3(A) and (B) is nearly the same and the pump intensity is well above the respective threshold, based on Eqs. (3.10) and (3.12), 10 times difference in the pump intensity leads to:

$$\frac{I_{th,A}}{I_{th,B}} = \frac{\gamma_A}{1-\gamma_A} \bigg/ \frac{\gamma_B}{1-\gamma_B} = 0.1.$$ (3.13)

Subscript A/B denotes the conditions in Fig. 3.3(A)/(B). Note that in Eq. (3.13), we use Γ=1, since all the dye molecules on the surface participate in lasing action. Using γ_A=4.3% obtained by Eq. (3.11) with m_I=1.45, $\lambda_0 = 520$ nm, $\eta Q_0 = 10^5$, $\sigma_e(\lambda_0) = 4 \times 10^{-16}$ cm², and A/L=170 μM, we arrive at $\gamma_A/\gamma_B = A_B/A_A = 0.14$, meaning that through specific binding processes the surface coverage of BSA is 14% of the non-specific case.

Using Eqs. (3.10)-(3.12) we can estimate the fraction of hybridized probe DNA cross-linked on the fiber surface based on the threshold difference. Referring to Fig. 3.4(D), after 10 nM target DNA incubation, Cy3 lasing threshold increases 3-fold. Thus,

$$\frac{I_{th}'}{I_{th}} = \frac{\gamma'}{\Gamma' - \gamma'} \bigg/ \frac{\gamma}{1-\gamma} = 3,$$ (3.14)

where the superscript denotes to the conditions after hybridization. In this case, Γ' is no longer unity after hybridization, since a fraction of Cy3 molecules are completely quenched by Cy5 through FRET and do not participate in lasing action. $\gamma' = \gamma$, considering that the total number of Cy3 molecules on the surface and the cavity loss remain the same and that the Cy5 absorption is negligible. γ is estimated to be 3.7% (using m_I=1.45, λ_0 = 600 nm, $\eta Q_0 = 10^5$, $\sigma_e(\lambda_0) = 4 \times 10^{-16}$ cm², and A/L=170 μM), which leads to $\Gamma' = 36\%$, meaning that 64% of the probe DNA is hybridized with the target DNA.

3.5 **Conclusion and outlook**

In summary, in this chapter, optofluidic lasers with only a single (or even sub-) molecular layer of gain medium are presented. Clean laser emission was observed with virtually no fluorescent background, thanks to well-controlled molecule's positions. In addition, due to the maximal light-matter interaction at the solid/liquid interface and the pre-concentration nature of the surface immobilization, only 1 μM of biomolecules (and hence the fluorophores) was needed to achieve the lasing, 10-1000 fold lower than the typical fluorophore concentration used in bulk solution based optofluidic lasers.[25,38,92,103] Furthermore, the optofluidic laser could be tuned using FRET through biomolecular bindings. Finally, threshold analysis based on the laser theory provides a simple means for us to estimate biomolecule surface coverage.

Since all the gain molecules are accessible from outside in the single layer gain laser, any external stimuli are expected to cause a rapid and drastic change in the laser gain and hence the laser output characteristics. Therefore, the work presented here will lead to the development of novel photonic devices that can be sensitively controlled at the level of a single molecular layer. Meanwhile, the potential of biosensing can also be explored to complement the traditional fluorescence based bioanalysis. Currently, the total number of gain molecules participating in the laser action is about 10 million (assuming a surface area of 1000 μm^2). With further reduction of the resonator dimension and surface using nanophotonic technologies, it may be possible to achieve detection of single molecules, in which changes in only one or a few gain molecules may cause an appreciable change in the laser output characteristics.

CHAPTER 4: **Integrated biological cell lasers**

4.1 **Introduction**

Previous chapters explore the *in vitro* scheme of the optofluidic biolasers, where biomolecules are extracted from its physiological context and re-distributed in an aqueous environment for laser operation and detection. Recent studies have shown that the laser signal can be directly generated with the gain resides in natural biological structures such as cells and tissues. Exploration of such *in situ* biolasers leads to novel applications of biolasers in cell level and tissue level biological studies and biomedical engineering.

As the basic building blocks of complex living organisms, cells are naturally investigated in optofluidic laser context. With intrinsic (fluorescent proteins) or exogenous (dyes) gain medium inside a cell, laser emission could be generated with merits including threshold-gated emission, narrow linewidth, fingerprint spectral patterns, and high sensitivity to dynamic changes of intracellular conditions.[2,14,23,84,104] Thus, cell lasers could have great potential for long-term cell tracking, [21,104] intracellular biomolecular interaction studies, and clinical screening.[2]

Currently, there are two major scenarios for cell lasing studies. In the first scenario, microcavities providing optical feedback for laser operation are located inside living cells. By letting cells intake microbeads (5-10 μm in diameter), Humar *et. al.* and Schubert *et. al.* both observed laser emission from cells.[23,104] Humar *et. al.* also demonstrated that oil droplets injected or naturally present in cells could be used for cell lasers.[23] In these works, microbeads and oil droplets served as ring resonators with high Q whispering-gallery-modes inside cells. This

scenario may encounter intrinsic obstacles for biomedical applications. It either relies on cells to intake relatively large ring resonators (diameter >5 µm), which is time-consuming and of low yield and has potential influence on the biological functions of the cells, or applies to only specific type of cells (such as adipocytes). Researchers are working hard on developing biocompatible and easily absorbed intra-cellular micro-resonators to expedite the practical application of this scheme.[20,21] In the second cell lasing scenario, cells containing gain medium are enclosed within an external cavity, which can be a droplet-based ring resonator[83] or a Fabry-Pérot (FP) cavity formed by two highly reflective mirrors.[4,105,106] Lasing from cells expressing fluorescent proteins or stained with dyes was achieved. This scenario is more versatile and can readily be applied to any type of cells. Compared to the droplet-based ring resonator, the FP scheme has the merit of easy implementation and signal collection. In most cell laser studies with the FP cavity, microbeads slightly larger than a cell (~20 µm in diameter) were mixed with cells to determine the FP cavity length and secure mirror alignment. However, in such a bead-defined FP cavity, cells were randomly spread or float on/near the mirror surface, making it difficult to track and monitor cells in a high throughput and multiplexing manner for an extended duration, which is highly desired in biomedical and biochemical analyses.

Fluorescent proteins and membrane-permeable organic dyes are commonly explored as the laser gain in cell lasing studies. However, how cellular conditions can affect the laser gain and how to interpret lasing characteristics for cell analysis have been rarely discussed.

In this chapter, to explore the potential of biolaser for cell analysis, cell lasers are studied from two perspectives. First, a FRET cell laser based on Sf9 insect cells expressing genetically engineered FRET protein pair is investigated. Second, an integrated cell laser array for high throughput and automated cell laser detection is presented.

4.2 **FRET cell lasers**

4.2.1 Motivation

Optofluidic FRET lasers have been demonstrated both theoretically and experimentally to have great potential in ultra-sensitive biomedical applications. So far, the exploration of FRET lasers is limited to the gain medium in bulk solution.[3,6,36] With the successful demonstration of cell lasers, it is promising to investigate FRET within living cells using the laser approach in order to achieve orders of magnitude signal enhancement over traditional fluorescence-based sensing technology. As a very first step towards this goal, here we experimentally investigated the lasing behaviors of cells expressing fluorescent protein FRET pairs with different energy transfer efficiencies. Numerical simulations are performed to theoretically analyze the impact of FRET on cell lasing.

4.2.2 Experimental

Sf9 insect cells and mCerulean-mCitrine (mCer-mCit) were chosen as the cell host and the fluorescent protein FRET pair, respectively. mCer-mCit is a well-studied fluorescent protein FRET pair with the Forster distance of 5.4 nm. It has been widely used in fluorescence-based biochemical studies to reveal interaction between biomolecules. To investigate the FRET effect on cell lasing, we genetically designed two types of mCer-mCit pairs with either high or nearly zero energy transfer efficiency. In the high-FRET pair, the donor (mCer) is linked to the acceptor (mCit) by a 6-redsidue peptide, resulting in a separation distance around 6 nm and hence a FRET efficiency of 35%. In contrast, the peptide chain in the non-FRET pair is 30 nm long. Sf9 insect cells were transfected with genes encoding the designed FRET pairs to produce the target proteins. Cells were tested 3 days post-transfection.

Fluorescence test (Enspire Multimode Plate Reader) of the cells revealed a 42% energy transfer efficiency between mCer and mCit in the high-FRET pair (Fig. 4.1(A)), corresponding to a separation distance of 5.7 nm between the donor and the acceptor, which is in good agreement with our design. For lasing tests, Sf9 cells in their culture medium were placed inside a Fabry-Perot (FP) cavity formed by a pair of dielectric-coated mirrors. The mirrors had high reflectivity in the 530-550 nm range and two transparent windows at 465 nm (for pump) and 565 nm (for fluorescence monitoring). The FP cavity was mounted on a 3D translation stage to allow the pump laser beam to scan across the mirror for testing of multiple cells. Each cell was pumped by a 5-ns pulsed optical parametric oscillator. An objective lens was used to excite and collect signal from the cell. The focal spot together with the cell under excitation was imaged by a monochromic CCD to monitor the excitation laser beam focus and precisely manipulate the position of the cell, so that identical optical alignment conditions for excitation and collection can be maintained from cell to cell. An Horiba iHR550 spectrometer was used to record emission from each cell.
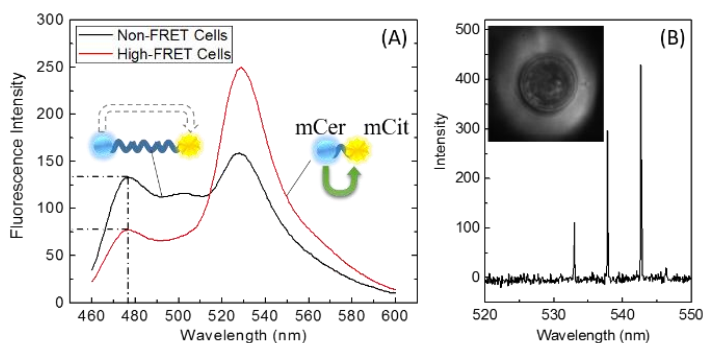
Figure 4.1 (A) Fluorescence spectrum of high-FRET and non-FRET cells. Inset: cartoons showing the structure of high- and non-FRET pairs inside each group of cells. (B) Lasing spectrum of a high-FRET cell. Inset: CCD image of the focal spot and the cell under investigation.

4.2.3 Results

The lasing characteristics of each individual cell were investigated under various pulse energies. Emission spectrum was recorded for each excitation pulse. Lasing signal was

distinguished from the featureless background and random noise by its sharp emission peaks and a specific emission pattern for a certain cell (Fig. 4.1(B)). We derived the concentration of FRET pairs inside each cell by measuring the 566 nm fluorescence intensity under 14 μJ/mm^2 465 nm excitation and normalizing it to the size of the cell, with the highest concentration measured set to 220 μM justified by later simulation results. The concentration of the high-FRET cells was further corrected by a factor of 1.50 due to the fluorescence enhancement by the FRET effect.

Both high-FRET and non-FRET cells were capable of lasing in the 530-550 nm range when excited at 465 nm. Fig. 4.2 shows the statistical results of the cell lasing performance of each group with a pump fixed at 260 μJ/mm^2. In the concentration range of (60, 120 μM), cells in both groups can lase with similar probability. There is no significant difference in lasing performance between high-FRET and non-FRET cells. These results suggest that the system variations in the current setup might block the effect of energy transfer between the donor and the acceptor in high-FRET cells on their lasing performance
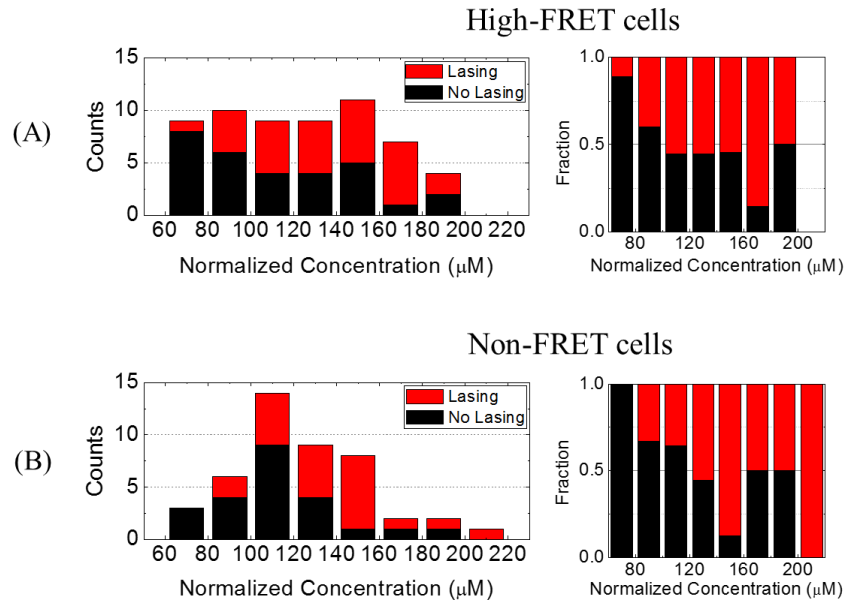
Figure 4.2 The population lasing performance of (A) high-FRET cells and (B) non-FRET cells

Numerical simulation was performed to better understand the experiment results. The lasing performance of a living cell expressing mCer-mCit pair in a FP cavity with either 0% or 42% FRET was modeled by the rate equations established previously.[84] Two practical facts were taken into account: (1) direct excitation of the acceptor mCit at 465 nm and (2) contribution of mCer to the lasing at the mCit band due to the overlap of the emission spectrum of the donor and the acceptor (Fig. 4.1(A)). A Q factor of 1.2e5 was used. And cell scattering loss of 15 cm^{-1} was taken into consideration. The simulation results show that photon density of a specific cavity mode increases dramatically beyond certain pump intensity, indicating lasing occurrence. With 42% FRET, a living cell of a fixed concentration of fluorescent protein pair (120 μM) has a lasing threshold of 180 μJ/mm^2, in comparison with 330 μJ/mm^2 in the non-FRET case. Thus, the FRET effect inside a cell with 120 μM FRET pairs can be identified by lasing occurrence when pump between 180-330 μJ/mm^2 (Fig. 4.3(A)). Monte Carlo simulation was also carried out to account for the variations in the experiments (Fig. 4.3(B)). It is shown that a normally distributed cell scattering coefficient with a mean value of 15 cm^{-1} and a 10% variance will make cell lasing become random events under 260 μJ/mm^2 excitation. In the concentration range of (80, 120 μM), 33% high FRET cells lase in contrast to 9% of non-FRET cells.
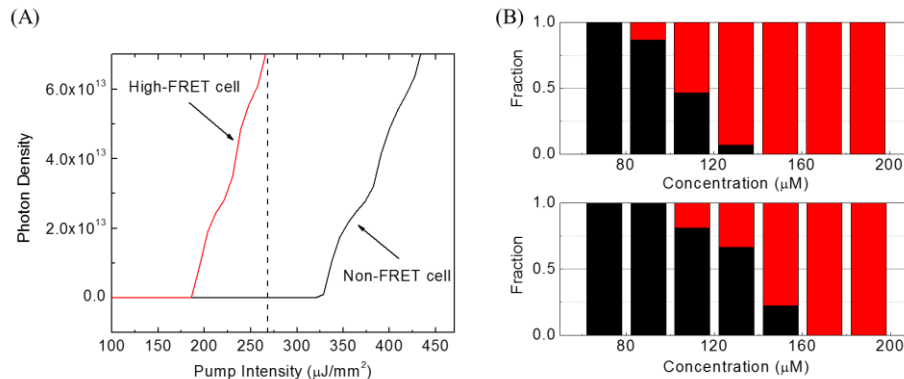
Figure 4.3 (A) Numerical simulation results of the lasing characteristics of high-FRET and non-FRET cells. (B) Monte Carlo simulation results of the lasing performance of high-FRET and non-FRET cells with a fixed pump intensity of 260 μJ/mm^2.

4.2.4 Discussion and conclusion

From the experimental observation and numerical simulation, we conclude that there should be factors other than the fluctuation of system variables (pump intensity, collection coefficient, cell scattering loss and local Q factor) that account for the similar lasing performance of the non-FRET and high-FRET cell groups. Indeed, confocal images of the non-FRET and high-FRET cells show that fluorescent proteins have drastically different distribution inside these two type of cells. Fig. 4.4 shows the confocal images of a typical high-FRET cell and a non-FRET cell. While fluorescent proteins distribute more homogeneously inside the high-FRET cell, an enlarged nucleus with no protein distribution is clearly seen in the non-FRET cell. Thus, given the same number of fluorescent proteins inside each cell and assuming similar cell size, the non-FRET cell will have higher local concentration, which can compensate for its relative low FRET efficiency and result in similar lasing threshold as the high-FRET cell.
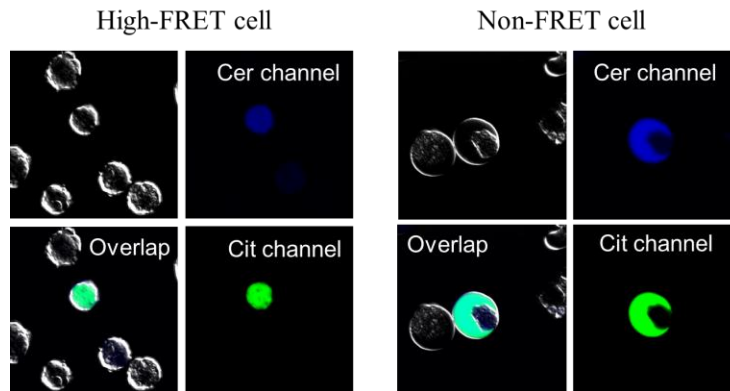
Figure 4.4 Confocal image of a typical high-FRET (left) cell and a typical non-FRET (right) cell. If the overall fluorescence intensity is the same, non-FRET cells tend to have higher local concentration due to enlarged nuclei.

Our results suggest several challenges in future exploration of FRET cell lasers: (1) There is no control of the expression level of protein FRET pairs inside a living cell. Naturally, the concentration of protein FRET pairs inside a transfected cell ranges from a few nanomolars to several hundred micromolars. This results in difficulties in quantification of FRET efficiency

since the emission intensity is concentration-dependent. Besides, to achieve lasing with a few hundred micromolar fluorescent proteins inside living cells is challenging, given the relative low quantum yield of fluorescent proteins and additional scattering loss introduced by the cell structure. (2) The genetically engineered cells can have morphologies that are significantly different from normal cells, which should be carefully characterized since laser emission is very sensitive to any cause of optical difference. (3) The FRET protein pair concentration required to achieve lasing in current setup is extremely high from physiological point of view. There is a high possibility that proteins will form clusters inside cells. This will result in ultra-high local concentration of FRET proteins. Basal FRET will occur due to the reduced inter-molecular distance even for protein pairs that are designed to have negligible FRET, which will cause false signal.

Optimizing the local Q factor and integrating the state-of-the-art microfluidic technologies will benefit the FRET cell laser analysis and enable monitoring of real-time FRET changes induced by external stimuli. The non-linear nature of laser designate the FRET cell laser to be a novel tool for monitoring subtle biochemical activities inside living cells. A wide range of scientific and clinical applications are, thus, promising.

4.3 **An integrated microwell array platform for cell lasing analysis**

4.3.1 Motivation

While lasing from single cells opens up a new perspective for biochemical analysis, the current cell-based lasing technologies are facing difficulties when a large number of cells need to be tested at single cell resolution. No automated and high-throughput detection using the laser approach has been demonstrated up to date.

Meanwhile, a microwell array is an attractive platform for cell level study nowadays, with a potential of high throughput and automation detection. It is capable of capturing and isolating cells and is compatible with imaging and subsequent molecular analysis,[107-110] thus providing information ranging from cell morphology to genomics and proteomes down to the single cell level. Microwells are also suitable for long-term monitoring of individual cells for their metabolic activities and response to external stimuli. [111]

In this section, a work that demonstrated an integrated microwell platform for cell lasing study using the FP cavity scheme is presented. Microwell arrays were fabricated on top of a highly reflective mirror to capture/locate cells. Lasing from cells in the microwells was achieved and characterized. The microwells provide physical addresses for cells, enabling cell tracking and long-term monitoring during laser interrogation. It was further shown that the integrated microwell array cell lasing platform is compatible with automated detection and suitable for high throughput long term monitoring, which will bridge the biolaser technology with practical applications.

4.3.2 Experimental

Fabrication of microwell array

Microwell arrays were fabricated in biocompatible negative photoresist SU-8 on the surface of dielectric mirrors using standard soft lithography to locate and support cell lasing in this work. 1" × 1" dielectric mirrors were obtained from Evaporated Coatings, Inc. (Willow Grove, PA, USA). The mirrors were designed to have a reflection band in 510 nm – 550 nm (R>99.5%) and a transmission band in 460 nm – 480 nm (T >90%). The arrays consisted of microwells with a depth of 25 µm and a diameter of 35 µm. To access wells more easily during experiments, every 10 × 10 wells were grouped into a sub-array in the design. The spacing between wells within a sub-array was 65 µm and the spacing between sub-arrays was 500 µm. The microwell fabrication procedures are described as follows. The mirrors were first cleaned by solvent ultrasonication (sonicated in acetone, ethanol and de-ionized water sequentially) and oxygen plasma treatment. Then, they were dehydrated at 150 °C for 15 minutes right before a 25 µm thick SU-8 2025 (MicroChem Corp., USA) layer was spin-coated on top. After soft-baking the SU-8 coated mirrors for 3 minutes at 65 °C and 8 minutes at 95 °C, a contact lithography tool Karl Suss MA 45S was used to UV expose the mirrors through a mask with the microwell array design. The exposed mirrors were subsequently subjected to post-exposure baking at 65 °C for 1 minute and 95 °C for 6 minutes, followed by 8 minutes of development. After rinsing and drying, the SU-8 microwell array on top of the mirror could be clearly seen under a microscope. The microwell arrays were further hard baked at 150 °C for 10 minutes and treated with oxygen plasma to improve hydrophilicity before loading with cells.

Cell preparation

Lasing from cells has successfully been demonstrated with various cell types and gain media over the past few years,[4,83,105,106] showing versatility that can be further explored for biophotonic studies and biochemical analysis. As a model system, in this work, Sf9 insect cells were used and stained with a green DNA dye, SYTO9 (ThermoFisher Scientific, USA) to demonstrate cell lasing in the microwell array platform. SYTO9 is a widely used live cell staining dye that is membrane permeable and turns into the fluorescent state when it binds with DNA/RNA. The DNA/RNA-specific nature of SYTO9 makes the laser gain potentially relevant to the physiological status of cells. For staining, Sf9 insect cells were first washed with HBSS buffer and re-suspended to a concentration of 1×10^6 cells/ml. Then SYTO9 was added to a final
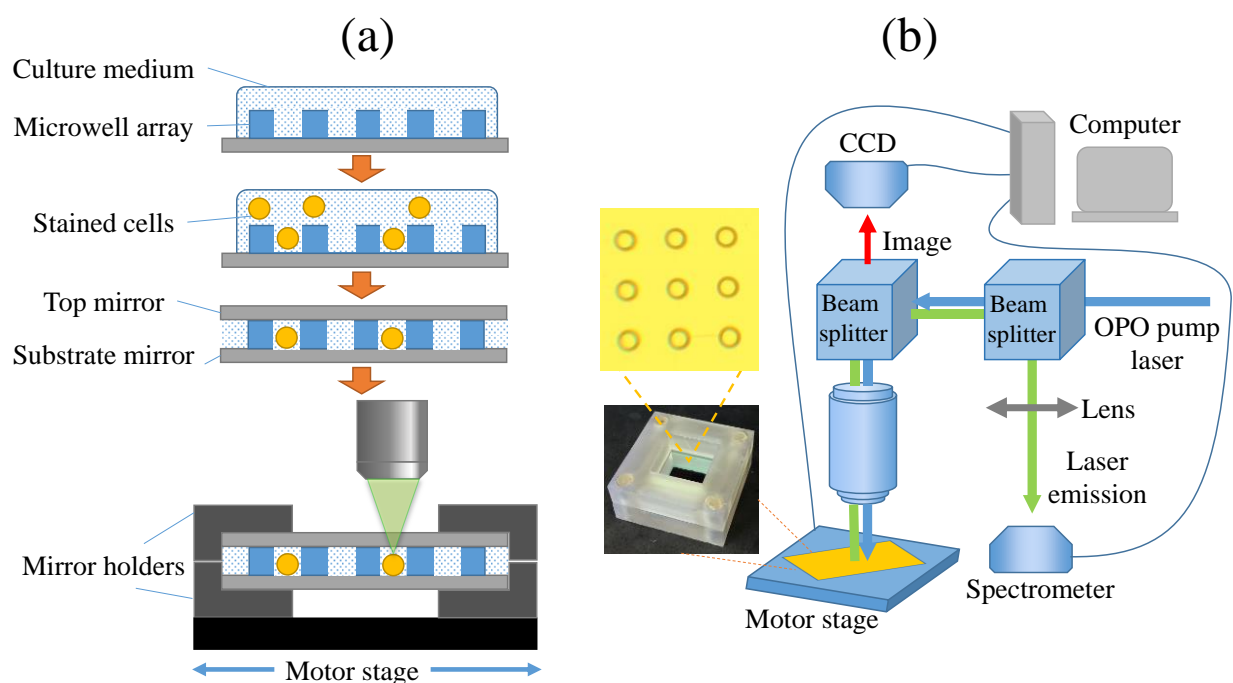
Figure 4.5 (a) Steps for loading cells into the microwell array. (b) Detection system for cell lasing in the microwell array. Inset: photo of the microwell-based FP cavity held in the mirror holder and the microscope view of the microwells.

72

concentration of 25 μM. After 10 minutes of incubation, cells were washed with HBSS to get rid of the excess dyes and re-suspended in the culture medium for their best viability. Fig. 4.5(a) shows the steps of loading the cells into the microwells and subsequent laser excitation/detection. Stained cells were added to the microwell array pre-wetted with the culture medium at a surface density of 400 cells/mm^2 and set still for 5 minutes for them to reach the bottom of the wells. Then the cells not captured by a microwell were removed by a cell culture scraper. Finally, a plane mirror was placed on top of the loaded array, thus forming an FP cavity with the substrate mirror. The mirror-microwell-mirror structure was held by a pair of 3D-printed holders for better mechanical stability and reduced buffer evaporation during the experiment. Note that the Sf9 are suspension cells under the current conditions. Without the confinement of the microwells, those cells could move around in the presence of flow or mechanical disturbance.

Detection system setup

For laser experiments, a typical confocal setup (Fig. 4.5(b)) was used to excite cells in the wells and collect the emission signal. An optical parametric oscillator (OPO) pulsed laser at 475 nm (5 ns pulse width and 20 Hz repetition rate) was used as the excitation source. The excitation spot size was 60 μm in diameter, slightly larger than the well diameter in order to illuminate the entire well homogeneously. The laser emission from cells was collected by an Horiba iHR 550 Spectrometer with the entrance slit set to 0.3 mm in order to collect signal from the entire 35-μm well area of interest. The mirror holder was mounted on a motorized 2D translation stage to precisely position the well of interest under the excitation beam.

4.3.3 Simulation

A diffraction simulation of a Gaussian excitation beam normal to the mirror was conducted (Fig. 4.6), showing that the presence of the microwell structure does not affect the excitation conditions of cells inside a microwell. A Gaussian beam along y-axis is set as the background field with an FWHM of 60 µm and the focal plane at the top interface between the mirror and water (Fig. 4.6(a)). By setting the refractive index of the SU-8 region to be 1.60 and 1.33, the distribution of the scattered field with and without microwell structure was numerically calculated respectively (Figs. 4.6(b) and (c)). The integration of the scattered field energy density over the water domain is 2.45e-19 and 2.60e-19 J/m^3 without and with the SU-8 microwell structure, respectively. The discrepancy is less than 10%, thus we conclude that the microwell structure does not have any significant effect on the excitation profile.
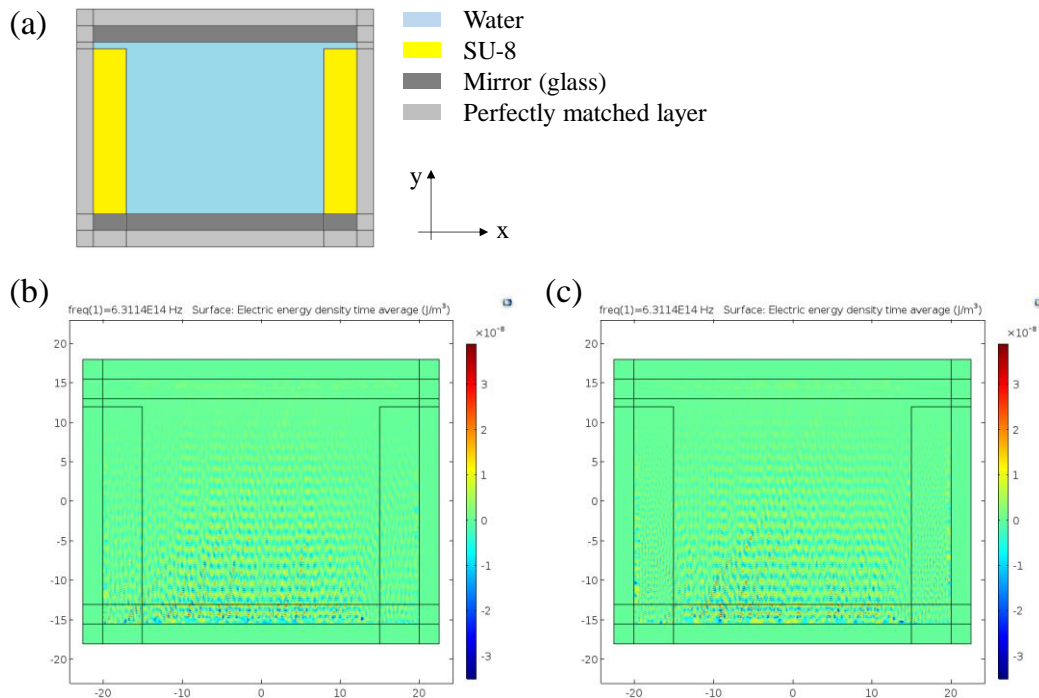
Figure 4.6 (a) The simulation geometry. $n_{water}=1.33$. $n_{mirror}=1.45$. (b) The distribution of the scattered field when there is no microwell structure (the SU-8 domain is set to be the same as the water domain, $n_{SU-8}=1.33$). (c) The distribution of the scattered field when the microwell is present ($n_{SU-8}=1.60$).

4.3.4 Results

Lasing from both suspension and adherent cells in an FP cavity were demonstrated previously, with a typical lasing threshold around 100 $\mu J/mm^2$. However, cells were randomly located on/near the mirror surface in those studies. In this work, SU-8 microwell arrays were used to locate the cells and track the cell lasing performance in an automated and high throughput manner. We first demonstrated and characterized the lasing emission from the captured cells in the microwells. The SU-8 microwell arrays defined the distance between the substrate and the top mirror hence the cavity length. Under the present loading condition (400 cells/mm^2) and considering that there are 100 wells (a 10×10 array) on an area of 1 mm^2, we expected about 40 cells can be captured in 100 wells (total area of 100 wells $\times$ 400 cells/mm$^2 \approx$ 40) and 30 out of them be captured as singlet according to Poisson distribution. Our experimental observation that approximately 30% of the wells were occupied by single cells agreed with the calculation. Lasing from SYTO9-stained cells in the well was achieved, as shown in Fig. 4.7, with a lasing wavelength ranging from 530 nm to 550 nm and a threshold
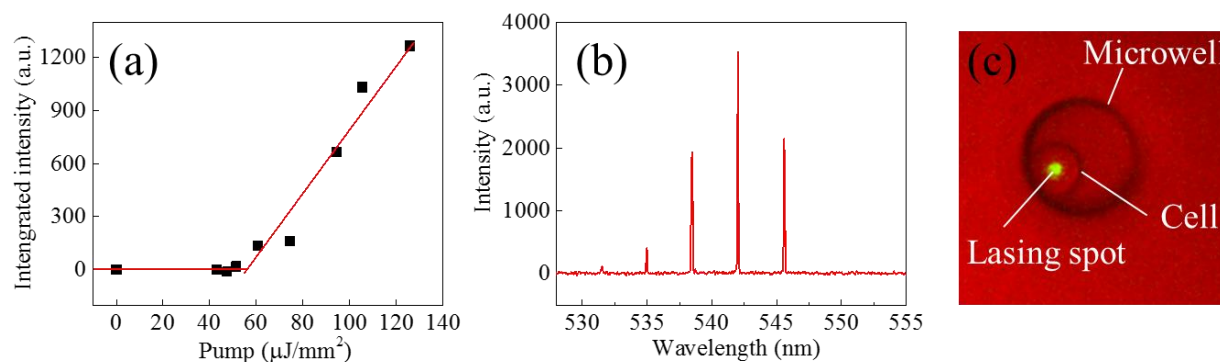
Figure 4.7 Lasing threshold (a) and lasing spectrum (b) of a cell captured in the microwell. (c) CCD image of the lasing cell. The red color results from mirrors rejecting green color in the illumination light coming from the bottom. Fluorescence from the cell is also filtered out by the mirror and therefore only strong lasing signal is detected and shown in the image.

75

around 60 $\mu J/mm^2$. The lasing wavelength was red shifted about 30 nm from the fluorescence maximum of SYTO9, which is typical for dye lasing. The relatively low threshold compared to previously reported cell lasers resulted mainly from the high abundance of DNA stained with SYTO9 in the nuclei. The effective dye concentration was estimated to be on the order of mM given the genome size of Sf9 ($\sim 1.6 \times 10^9$ bp)[112] and the association constant of SYTO9 (1.8×10^5 M^{-1})[113]. The free spectral range (FSR) of the lasing modes was around 3.5 nm, corresponding to a cavity length of 30 μm (assuming the effective refractive index of the cavity is 1.36 in the presence of a cell). The slightly increased cavity length compared to the SU-8 thickness might result from a thin culture medium layer between the SU-8 and the top mirror.

About 30% cells captured in microwells could lase under 130 $\mu J/mm^2$ excitation. Fig. 4.8(a) plots the histogram of the lasing threshold for the lasing cells in the microwells, showing the lasing threshold that could range from 20 $\mu J/mm^2$ to 100 $\mu J/mm^2$. This heterogeneity in the lasing threshold is attributable to different DNA concentrations inside nuclei that depend highly on the size of the nuclei, the cell cycle stages and the polyploidy that generally observed in Sf9 cells due to their chromosome instability. For comparison, the SYTO9 stained cells were also tested in a bead-based FP cavity similar to that in Ref. 4 (bead size 30 μm in diameter in the current work) and a similar percentage of cells (26%) were found to lase under 130 $\mu J/mm^2$ excitation. The histogram of the lasing threshold for the lasing cells is plotted in Fig. 4.8(b) and shows virtually no difference from the microwell case, suggesting that the microwell structures do not have any impact on cell lasing behavior as implicated in the numerical simulation. This is expected since the lasing modes of cells are mainly confined by the mirrors and the cell itself. The confinement of the microwell structure on the lasing modes is negligible, given the

relatively large size of the wells compared to cells and the low reflectivity on the boundary between SU-8 and water.
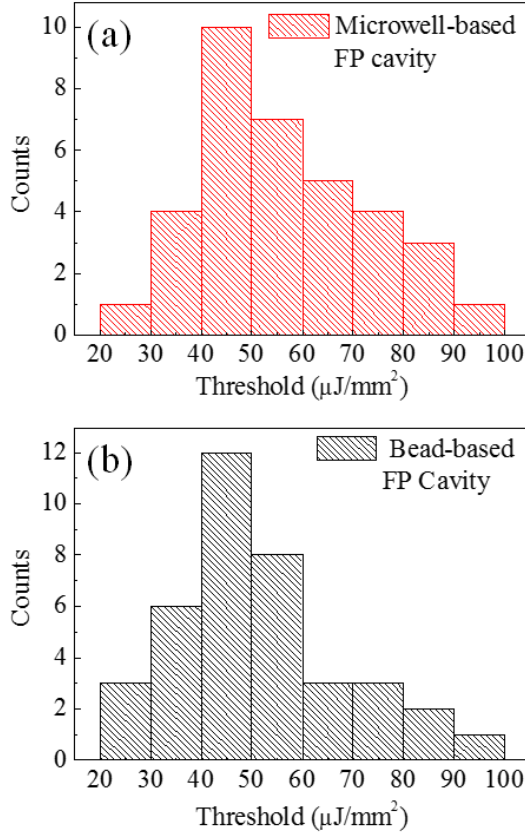
Figure 4.8 Histogram of the lasing thresholds for (a) the cells captured in a microwell array and (b) the cells, along with beads, randomly spread on top of the mirror.

It is known that the cell has a slightly larger refractive index than the surrounding culture medium, which provides the lensing effect for stabilizing the FP cavity and makes lasing insensitive to mirror misalignment (tilt tolerance ~0.5 degree). Consequently, the Q-factor for each microwell is determined mainly by the reflectivity of the mirrors and the optical characteristics of the cell itself (such as gain, absorption and scattering). In our experiment, the empty cavity Q-factor in the absence of a cell is estimated to be over 6×10^4 according to the cavity length of 30 μm and the round-trip loss of <1%. With a cell in presence, the Q-factor

drops to 1×10^4 due to the ~5% round-trip loss from the cell. Therefore, the cell lasing performance (*e.g.*, the lasing threshold or efficiency) can be used to reveal the gain and loss present in a cell, which can vary significantly with cellular conditions such as morphology, cell cycle, metabolic status and polyploidy. Such variations have already manifested themselves in the lasing threshold distribution in Fig. 4.8, highlighting the strong need for the ability to track individual cells and perform highly multiplexed detection on a large cell population.

After lasing measurement, the top mirror was replaced by a transparent cover glass and the conventional fluorescence image of the cells in the well was taken. Thanks to the microwells, the cells residing in the microwells were not disturbed, thus allowing us to compare side-by-side the fluorescence image with the laser image, as illustrated in Fig. 4.9, which verifies that the laser indeed occurred in the heavily stained nucleus region. Further comparison shows that there are specific patterns that could be identified in the laser image. For example, in Figs. 4.9(a) and (b), the cells mainly support (1,1) Ince-Gaussian modes.[4,114,115] In Fig. 4.9(c), the (0,0) mode is supported instead. However, in the fluorescence images all three cells show only one stained
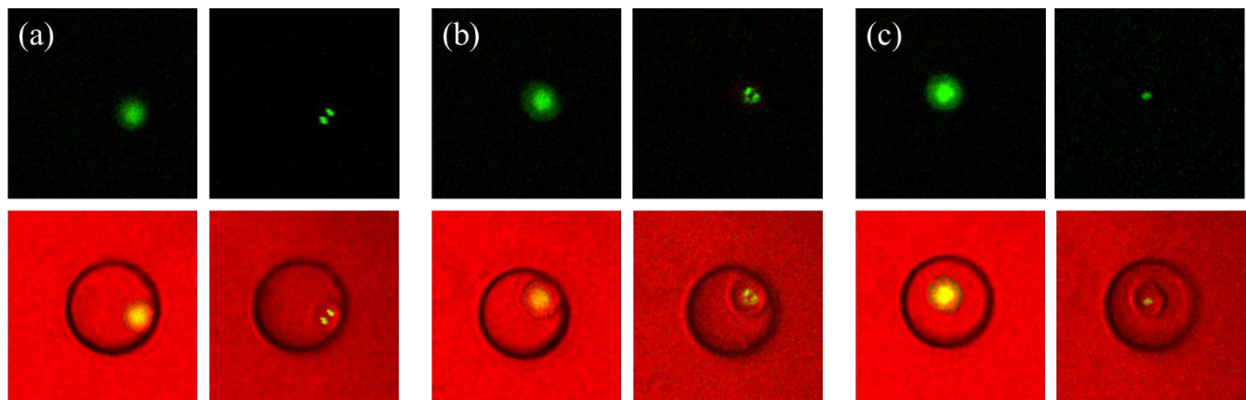
Figure 4.9 (Top row) Fluorescence (left) and lasing (right) image of three different cells (a), (b) and (c) captured in three different microwells. (Bottom row) Corresponding bright field images, where fluorescence (left) and laser emission (right) are superimposed for better visualization and comparison.

nucleus without any details. The difference in laser images could result from a combined effect of the cell morphology and the refractive index[116] and the gain distribution inside a cell, which can vary significantly throughout the cell cycle. Thus, the laser-based detection, with the aid of microwell arrays may provide a new approach for better understanding of cells.

The pre-defined positions of microwells in an array also makes it possible to perform high throughput automatic laser detection. To implement this, a LabView program was used to coordinate the 2D motorized translation stage, the spectrometer and the imaging CCD. The position accuracy of the translation stage was characterized, showing a center-to-center difference of <5 μm between different wells. With a fixed pump intensity at 130 μJ/mm^2, a 10 ×10 well array loaded with SYTO9 stained Sf9 cells was screened and the emission spectrum and the CCD image of each well were collected automatically. It took 5 minutes to screen the whole array in the current setup, which can be further shortened with a more advanced automation system. Fig. 4.10 shows the screening results. The number in the table (Fig. 4.10(a)) represents the peak value of each spectrum. To determine whether a cell is lasing, the cut-off value is set at three standard deviations of the background noise (50 in this example). The highlighted regions in the table indicate there were cells lasing at corresponding microwells. The FSR of the lasing mode was measured to be 3.51 nm across the entire array, which confirms the identical optical condition for all microwells. Together with the CCD image of each microwell, we can study the lasing population and the status of lasing cells statistically. In this example, there were 28 wells occupied by single cells, 10 of which could lase, while 13 wells were occupied by double cells and 8 of the total 26 cells could lase. The overall lasing ratio was 33%, which agreed well with the manually measured results. There was no significant difference in the

(a)

	1	2	3	4	5	6	7	8	9	10
A	48	20	17	36	3838	34	481	31	37	3448
B	30	30	35	31	29	2512	33	39	34	34
C	35	37	631	30	30	33	32	32	4066	29
D	32	39	32	28	29	36	381	32	2402	35
E	29	34	31	29	28	33	39	33	38	694
F	33	28	35	32	3257	37	33	303	33	37
G	32	29	34	31	31	26	4177	31	26	34
H	27	29	41	32	34	33	38	32	29	3443
I	30	8123	34	31	36	36	34	34	31	290
J	198	31	38	1760	34	822	1285	33	31	40

(b)

A10
B6
F5
H10
I2

530   535   540   545

Wavelength (nm)

(c)

A10   B6   F5   H10   I2

Figure 4.10 Results of automatic scanning. (a) Heat map of the lasing array. Data shows the spectrum peak value of each well. The yellow-highlighted boxes denote the microwell that have cell lasing. (b) Sample spectra of lasing wells identified by its row/column number given in the y axis. (c) Corresponding lasing images with illumination light on. OPO excitation=130 μJ/mm^2. CCD exposure time = 100 ms.

lasing ratio between the one-cell-in-a-well and two-cell-in-a-well cases, indicating that lasing behavior of a cell was independent of its neighbor cell.

We further demonstrated that the automatic scanning microwell array enables high throughput time-series monitoring of cell lasing behavior. One cell-loaded array was continuously scanned over 25 minutes and the lasing characteristics (such as spectrum and image) of each cell were tracked. The pump intensity was fixed at 130 μJ/mm^2. There were 55 cells captured in the wells in this case (41 singlets, 7 doublets) and 17 of which could lase at the beginning. Cells with a relatively low lasing intensity ceased to lase gradually during monitoring due to photobleaching of SYTO9. There were 9 cells with identifiable lasing peaks throughout the entire monitoring process, 7 out of which were found to have unchanged lasing patterns in both the spectrum and the CCD image. A representative sample (cell in well E5) is shown in Figs. 4.11(a) and (b). According to Fig. 4.11(a), while the FSR of the cell laser remains virtually the
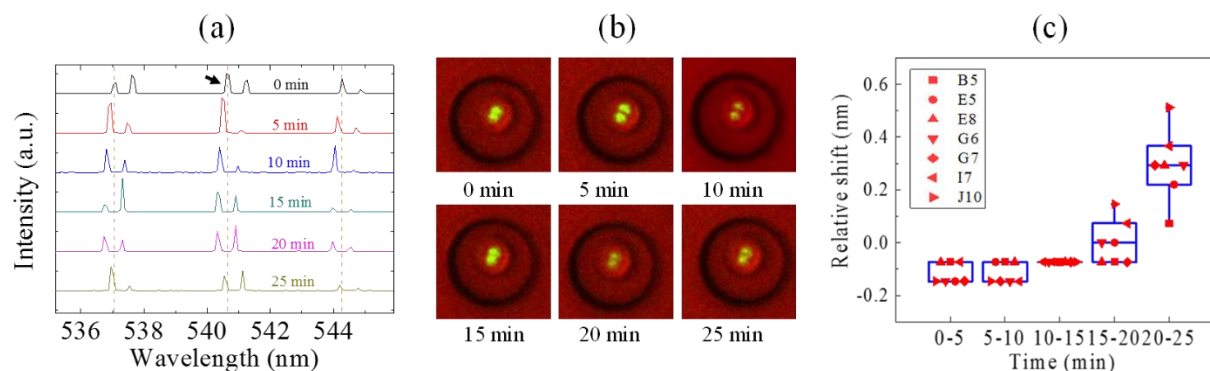
Figure 4.11 (a) Lasing spectra of a cell captured in a microwell (E5) in long term monitoring. OPO excitation = 130 μJ/mm². Curves are vertically shifted for clarity. The arrow indicates the peak whose wavelength was tracked. (b) Corresponding images of the cell, showing that the lasing pattern remained unchanged during the entire 25 minutes of experiment. The green channel is enhanced for better visualization of the lasing modes. (c) Boxplot of the wavelength increment of every 5-minute interval for a lasing peak near 540 nm for 7 cells (in microwells B5, E5, E8, G6, G7, I7 and J10, respectively) on the same array. A positive/negative increment denote a red/blue shift in wavelength.

same through the entire 25 minutes of the experiment, there is a gradual blue-shift of the lasing wavelength between 0 min and 20 min and a reversal trend (red-shift) from 20 min to 25 min. Although the detailed mechanism for the blue- and red-shift are still unclear to us, they occur consistently for all 7 cells under study, as shown in Fig. 4.11(c). We speculate that this systematic drift in our experiment conditions might be caused by buffer evaporation and concomitant salt concentration increase, which change the cavity length and the buffer refractive index. Note that the relatively large variance in the wavelength shift is observed for the 15-20 min and the 20-25 min groups, which is caused by the cells in microwells B5, I7 and J10. Since B5 and I7/J10 were tested at the beginning and at the end of each scan, our relatively slow scanning speed (5 minutes) might not be able to catch up with the systematic change in experimental condition discussed above.

Based on the work in Fig. 4.11, a reference baseline can be established and help identify and analyze cells that have "deviated" or "abnormal" lasing behavior. Fig. 4.12 shows evolving
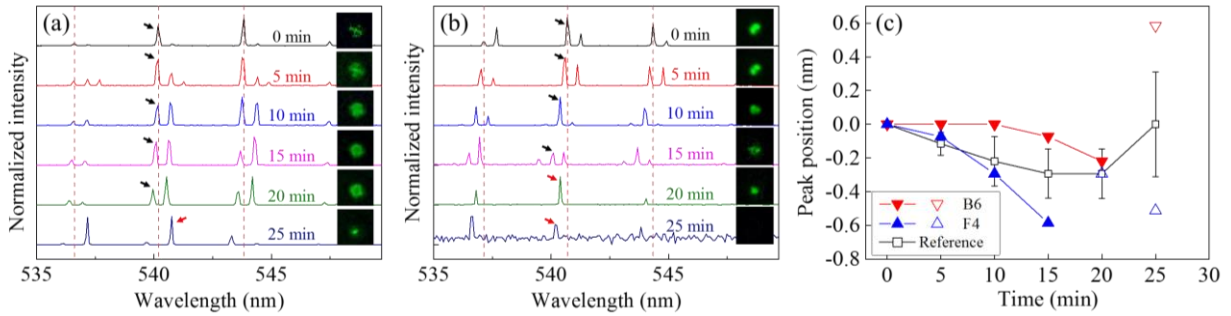
Figure 4.12 Spectra of the cell from microwell B6 (a) and microwell F4 (b) showing evolving lasing patterns during long term monitoring. Arrows mark the peaks that were tracked. Inset: the corresponding lasing patterns extracted from CCD images and enhanced for better visualization. (c) Relative position of the marked peaks in (a) and (b) during monitoring. Black curve corresponds to the reference baseline derived from the 7 cells shown in Fig. 6(c). Error bars show the 95% confidence interval. Hollow symbols correspond to peaks marked by red arrows in (a) and (b), which are likely different modes from those marked by black arrows.

lasing characteristics of the 2 "abnormal" cells from the same microwell array as in Fig. 4.11. For cell B6 in Fig. 4.12(a), the lasing mode shown in lasing images changes from the Ince-Gaussian (2,2) mode to higher order modes and eventually to the (0,0) mode. For cell F4 in Fig. 4.12(b), the initial Ince-Gaussian (1,1) mode rotates 90° and is replaced by the Ince-Gaussian (0,0) mode. Fig. 4.12(c) plots the relative position (with respect to that at 0 min) of a lasing peak marked by arrows in (a) and (b) for both cells. A reference curve derived from Fig. 4.11(c) is also plotted as a benchmark to indicate the collective response of the "normal" cells to the systematic changes. It is obvious that these two "abnormal" cells have a different and opposite response. The lasing modes in B6 cell are more resistant to the systematic changes, and the lasing peaks barely shift before the pattern changes. In contrast, the lasing modes in F4 cell turns out to be more susceptible and shift a relatively large amount before we lose track of the modes. Humar, *et.al.* reported the change in cell lasing patterns by changing the buffer refractive index outside the cell.[106] However, in our case, the change of the effective refractive index (caused by thermal-optic effect and buffer salt concentration) and the cavity length were identical across the

entire array and were verified to be negligible (<0.1%) according to Fig. 4.11, and thus cannot explain the deviations in the lasing behavior of those two cells. Possible reasons could be the dynamic change of cellular geometry, the integrity of nucleus (nucleus may be broken down following apoptosis[117]) and photobleaching of dyes that consequently change the gain profile within the cell. To fully understand the lasing pattern shift, detailed quantification of the cell sizes, the DNA concentration/distribution and the difference in responsiveness of cells to external stimuli (heat, osmotic pressure change, etc.) is essential. On the other hand, the existence of such "abnormal" lasing cells shows the potential of using the lasing cell array to study the inhomogeneity within a cell population.

4.3.5 Discussion

The thermal effect on the microwell-integrated cell lasing array. Given that there is environmental temperature fluctuation during the experiment, the resulting lasing wavelength shift is examined as follows. The dependence of the lasing wavelength λ on temperature can be written as $\frac{\Delta\lambda}{\lambda} = (\frac{1}{n_{eff}}\frac{dn_{eff}}{dT} + \frac{1}{L}\frac{dL}{dT})\Delta T$, where n_{eff} is the effective refractive index, $\frac{dn_{eff}}{dT}$ the thermal-optic coefficient, L the cavity length and $\frac{dL}{dT}$ the linear thermal expansion coefficient. A cell laser cavity consists of mainly water, DNAs and proteins, with an effective thermal-optic coefficient estimated to be $-1\sim4\times10^{-4}$/°C.[118-120] Since SU-8 layer acts as spacer for the laser cavity, the linear thermal expansion coefficient of SU-8 (52×10^{-6}/°C, MicroChem Corp.) is used to estimate $\frac{1}{L}\frac{dL}{dT}$. Thus, given a temperature drift of 1°C, $\left|\frac{\Delta\lambda}{\lambda}\right| < 0.05\%$ and the lasing wavelength shift $\Delta\lambda$ around 540 nm is about 0.2 nm.

We also examine the thermal effect of the pump laser. At 120 µJ/mm² pump fluency, the total energy shone on an area of 2×10^{-4} mm² (the area of a cell) is 2.4×10^{-8} J per excitation

pulse. Typically, less than 10% of the total energy can be absorbed (absorption cross section of dyes at excitation wavelength $\sigma_a \sim 1 \times 10^{-16} cm^2$, dye concentration C ~1 mM, gain medium length L~ 10 μm, thus absorbance A $= \sigma_a CL = 0.06$) and only a fraction that non-radiatively dissipates turns into heat (assume to be 40%, since quantum yield of SYTO9=0.6). The resulting fluctuation in local temperature is estimated to be around 0.3 °C ($\Delta T = \frac{E_{heat}}{C_p m}$, E_{heat} the energy that turns into heat, C_p the specific heat (water: 4.184 J/(g·°C)), m the mass). The lasing wavelength might have a drift of 0.06 nm accordingly. However, no build-up effect is expected under continuous pulse excitation due to the small duty cycle (5 ns/50 ms) of the 20 Hz OPO laser.

The photobleaching effect. Lasing stability of a cell captured in a microwell. The cell was continuously excited for 30 seconds with a pump intensity of 100 μJ/mm². The cell underwent up to 600 excitation pulses during the test, about twice the number of pulses that a cell might receive when it was scanned for 6 times in our work. As shown in Figure 4.13, no wavelength shift is observed in those lasing peaks thus it is justified that the wavelength shift observed in long term monitoring is not due to the photobleaching effect of SYTO9.
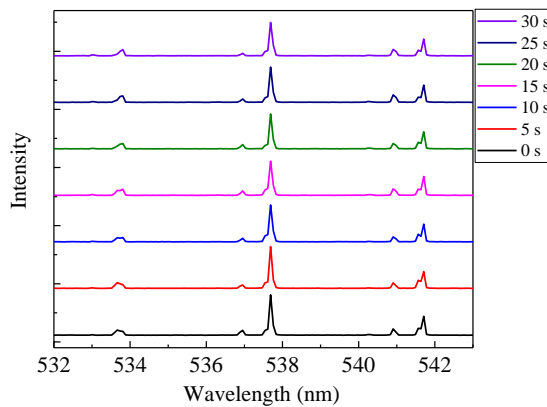
Figure 4.13 Lasing stability of a cell captured in a microwell

The cell, together with its subcellular structures such as the nucleus, is a naturally formed complex optical system. By specifically staining the components inside a cell, a spatially varying gain profile can be achieved in a cell laser system. For example, when the nucleus is specifically stained as in this work, the gain is limited to a region smaller than the cavity formed by the entire cell and the two parallel mirrors. Such a configuration has been shown to favor the operation of high-order Laguerre-Gaussian modes in a stable cavity[121] and has also been utilized in the generation of Ince-Gaussian modes.[122] Similarity can be drawn between the SYTO9 stained Sf9 cells and the lasing system with tightly confined gain profile reported in Ref. 122, since the Ince-Gaussian modes are commonly observed in our work (see Figs. 4.11 and 4.12). Therefore, it is possible to use the laser mode to extract the gain distribution and reconstruct cellular structures/geometries, such as the size and the nuclear-cytoplasmic ratio of the cell.

4.3.6 Conclusion

In summary, we have prototyped and characterized an automated, integrated microwell array platform for systematic and statistic studies of cell lasers. The microwell array does not affect the cell lasing performance, but makes the captured cells more resistant to disturbance, thus allowing us to track individual cells and performing various analyses on them. It further enables the establishment of the reference baseline that represents the collective responses of cells to a change in an overall environment and the identification of rare "abnormal" cells that deviate from a large cell population. The microwell array is readily compatible with other technologies such as hyperspectral imaging,[4] polarization analysis, and temporal profile study.[14] Further integration of microfluidics channels that facilitate cell incubation, drug treatment,[123] and downstream process and analysis[107,110] will open the door to applying the cell lasing approach to single cell analysis and drug screening.

CHAPTER 5: **Summary and outlook**

In this thesis, several integrated optofluidic laser systems are presented that expand the potential for the use of optofluidic lasers in biological/biochemical applications.

Optofluidic FRET lasers based on fluorescent proteins, DNA tetrahedra, and aqueous quantum dots were experimentally demonstrated and characterized. Using the laser approach, small FRET efficiency differences can be detected with up to 100-fold enhancement in detection sensitivity. One step further from the *in vitro* FRET lasers that operate with the FRET pairs dispersed in bulk solution, an *in vivo* FRET laser that uses FRET fluorescent proteins inside living cells was also investigated, providing insights into future development of FRET laser detection schemes for cellular activities.

An optofluidic biolaser was achieved with a single molecular layer of gain on the surface of a fiber. The concentration of gain molecules required for laser operation was significantly reduced from >10 μM to <1 μM using this scheme. Laser tuning through molecule interaction on the surface was also demonstrated. This work provides a novel laser-based detection platform analogous to surface-based fluorescence technologies, introducing plenty of potential applications.

Furthermore, an integrated microwell array platform was developed for high throughput and automatic cell laser detection. Microwells integrated into an FP cavity provide physical addresses to track individual lasing cells and enable long-term monitoring. Cells stained by a DNA dye were studied using this platform. A distribution of lasing thresholds was observed, and

cells with deviated long-term lasing behavior were identified, which indicate the heterogeneity of the cell population. This platform is important for the systematic study of the dependency of cell lasing performance on cellular activities, which is the foundation for future development of laser-based cell analysis schemes.

The application of these biolaser systems to practical biological/biochemical detections is the primary direction for future work.

5.1 **DNA analysis**

Biolasers have been used for differentiating DNA single-nucleotide-polymorphism (SNP) species with a up to 100X sensitivity enhancement as compared to fluorescence technologies.[7,65] In these studies, thin-walled capillaries are used as the resonant cavity, which cannot be mass-produced with consistent optical quality and require high sample concentration (> 50 μM) for laser operation.

On the other hand, the laser scheme, discussed in Chapter 3, with gain molecules concentrated at the surface shows great potential for practical point-of-care DNA analysis. For consistent detection performance, commercially available fibers can be used as the resonant cavity which have very small variations (<1%) in diameter over kilometers of length. By concentrating analytes to the surface of the fiber, it is possible to reduce the required sample concentration to less than 1 μM with a total volume of a few μL.

It has been recently demonstrated that such a fiber-based DNA detection system can differentiate target DNA from irrelevant sequence as well as its SNP by the on/off of laser emission.[124] In this work, DNA intercalating dye, which turns into bright state upon binding with double-stranded DNAs, is used as laser gain medium. No pre-labeling of either the probe or the target DNA strand is required. This system features a digital-like (on/off) detection signal and

ultra-low sample consumption (a few μL of 100 nM analyte); it is promising for point-of-care applications as a result of its compactness and the robustness of optical fibers that serve as high Q and low cost optical cavities.

In the future, this system can be further optimized by integration with microfluidic channels that can help with sample preparation and analysis procedure standardization.

5.2 **FRET biolasers for *in vitro* and *in vivo* molecule interaction analysis**

The experimental and theoretical studies of FRET laser discussed in previous chapters reveal that FRET laser signal can indicate small changes in FRET efficiency with enhanced sensitivity. Thus, FRET lasers are especially suitable for researching molecule interactions that are modulated by stimuli such as messenger molecules and drugs. Upon stimulation, the change of FRET efficiency can be very small due to weak modulation or a small fraction of responsive molecules in the ensemble. With enhanced sensitivity, FRET lasers will have a better chance of picking up on small changes than fluorescence technologies.

The feasibility of using fluorescent proteins for FRET laser is already demonstrated in this dissertation. FRET efficiency is controlled by the length of a peptide link between the donor and acceptor in Section 2.2. In the future, the FRET laser performance can be further characterized by changing the length of the peptide link. Next, interacting protein domains can be fused with fluorescent protein donors and acceptors respectively by genetic engineering. G-protein-coupled receptors (GPCRs) and their corresponding aptamers are examples of interaction protein domains that play an important role in signal pathway studies. GPCRs are involved in many diseases and are the target of approximately 40% of the medicinal drugs in the market.[125,126] For *in vitro* detection, thin-walled capillaries and surface functionalized fibers can both be used as the resonant cavities. For research into the interactions that happen inside living

cells, the integrated microwell array serves as an ideal platform. The interaction can be monitored through measuring the changes of FRET lasing signal under different conditions, such as the type and concentration of the drug used. With enhanced sensitivity for the FRET efficiency change, FRET biolasers are promising for screening drugs that have a small but physiologically relevant difference in efficacy.

5.3 Characterization of lasing performance of nucleus-stained cells

In Section 4.3, by using the integrated microwell array platform, a heterogeneity in lasing performance of cells stained by the DNA dye SYTO9 was observed. The heterogeneity can result from differences in many parameters, including the cell's DNA concentration, chromatin status, and nucleus morphology. Cells in different cell cycles or undergoing apoptosis are supposed to have unique combinations of these parameters. Systematic investigation of the lasing performance of cells under different conditions is very important from both a research and a clinical point of view.

To conduct the investigation, cells can be arrested at certain cell cycles or triggered to programmed cell death (apoptosis) by drug treatment. Alternatively, cells can be sorted using a flow cytometry based on certain criteria (for example, immunofluorescence staining pattern). Next, the cells are fixed, stained with DNA dyes, loaded to the microwell arrays, and scanned for their lasing performance. The lasing threshold, lasing spectrum, lasing spatial distribution, and related cellular conditions (the size, the treatment condition, etc.) should be recorded and analyzed. Once the way the lasing performance of a cell reflects its nucleus status is fully understood, the cell lasing array can be used for discriminating subpopulations of cells (for example, cancer vs normal[127]) and studying drug effects, providing an unprecedented aspect to better examine related clinical problems.

89

Appendix A

The incubation and transfection of Sf9 insect cells

Insect cell (Sf9) Culture Procedure

Insect cells Sf9 can be obtained from ThermoFisher (USA). Cell stock can be established following company provided thawing procedure. Suspension cells are incubated in 125 mL flask with 30 mL SF900-II (ThermoFisher) medium in our lab. A shaking incubator (28 °C, 135 rpm) is used to hold the flasks. Here, steps for maintenance of the cell stock are listed.

1. Wash hands thoroughly and wear gloves. Be sure to spray hands with 70% ethanol (squirt bottles) before handling cell cultures.

2. Retrieve the cell culture stock flask from the 28 °C incubator.

3. Spray and wipe the flask bottom with 70% ethanol before entering the sterile hood.

4. Swirl the flask to resuspend cells that may have settled.

5. Remove ~50-100 μL of cells and place them in a 1.5 mL plastic tube.

6. Outside of the hood, add an equal volume of 1:5 Trypan blue solution to the tube and flick to mix.

7. Wipe clean the haemocytometer and coverslip (drawer below the microscope) with a kim-wipe and 70% ethanol.

8. Place the coverslip over the groove in the surface of the haemocytometer and add 10-12 μL of the cells with trypan blue to the groove. Surface tension should draw the liquid over the surface of the haemocytometer.

9. Count the cells within the pattern of squares using the microscope (100 cells ~ $1x10^6$ cells/mL of culture). Cell culture stock flasks should be maintained between ~$1x10^6$ and $10x10^6$ cells/mL.

10. For normal maintenance of the cell culture stock flask, calculate the volume of cells needed to have $1x10^6$ cells/mL in 30 mL final volume.

11. Remove the excess volume of cells and add the appropriate volume of Sf900-II cell culture media with Antibiotic-Antimycotic (ThermoFisher) to bring the final volume to 30 mL using the large, individually wrapped serological pipets.

12. Return the cells to the 28C incubator.

13. Check cells every 3-4 days.

Insect cell (Sf9) Transfection Procedure

The Sf9 insect cell line is a suitable host for expression of recombinant proteins from baculovirus expression systems. Here, transfection steps with DNA vectors encoding desired fusion protein is described.

Before start:

1. Warm up A/A antibiotic media, media without antibiotics, and OptiMEM (ThermoFisher) to room temperature.

2. Determine which constructs that will be transfected, and determine the amount of DNA needed for the size of transfection that will be performed (15 mL transfections require 2.5 µg; DNA concentration is taken as ng/µL).

3. Collect as many clean, sterile flasks as necessary.

Cell Preparation:

1. Bring the stock culture into the hood as usual and obtain an accurate count of cells

2. $2x10^6$ cells/mL in 15 mL is needed for each transfection. Pipet the appropriate amount of culture into a 15 mL conical tube.

3. Spin the cells down in the centrifuge located in the chemical storage room. Spin at 250g for 3 minutes.

4. Use the vacuum line in the hood and a glass pipet to remove the media.

5. Resuspend the cell pellet with 7 mL of antibiotic free media and add to a clean, sterile flask. Add an additional 7 mL of antibiotic free media to the flask.

6. Split the remaining volume in the stock flask as normal down to $1x10^6$ cells/mL in 30 mL.

7. Return your transfection flasks to the shaker while you prepare the DNA mixture.

DNA Preparation:

1. Bring OptiMEM, the DNA to transfect and the transfection reagent (Escort IV) in the hood.

2. For each transfection, add 600 µL of OptiMEM to two 1.5 mL tubes. Label one for DNA and one for Transfection reagent.

3. Add 2.5 µg of DNA to the tube labeled for DNA and 30 uL of transfection reagent to the tube labeled for transfection reagent. Close the tubes and invert 2-3 times to mix.

4. Add the DNA tube to the transfection reagent tube one drop at a time. Invert the reaction mixture tube 2-3 times to mix.

5. Incubate the reaction mixture 15 minutes in the hood.

6. After 15 minutes, retrieve the transfection flasks from the shaker and add the transfection reaction mixture to the flasks one drop at a time.

7. Return the flasks to the shaker. Protein expression takes approximately 3 days.

General Tips:

1. Wipe down everything that goes into the hood with 70% ethanol.

2. Avoid shocking cells thermally. Warm the cell culture media to room temperature before adding it to cells.

3. The amount of DNA and transfection reagent can be increased to boost the protein expression at individual cell level.

Bibliography

1. S. H. Yun and S. J. J. Kwok, *Nat. Biomed. Eng.*, 2017, **1**, 0008.
2. X. Fan and S. H. Yun, *Nat. Methods*, 2014, **11**, 141 - 147.
3. Q. Chen, X. Zhang, Y. Sun, M. Ritt, S. Sivaramakrishnan and X. Fan, *Lab Chip*, 2013, **13**, 2679-2681.
4. M. C. Gather and S. H. Yun, *Nat. Photon.*, 2011, **5**, 406-410.
5. Q. Chen, H. Liu, W. Lee, Y. Sun, D. Zhu, H. Pei, C. Fan and X. Fan, *Lab Chip*, 2013, **13**, 3351 - 3354.
6. X. Zhang, W. Lee and X. Fan, *Lab Chip*, 2012, **12**, 3673-3675.
7. Y. Sun and X. Fan, *Angew. Chem. Int. Ed.*, 2012, **51**, 1236-1239.
8. Y.-C. Chen, Q. Chen, T. Zhang, W. Wang and X. Fan, *Lab Chip*, 2017, **17**, 538-548.
9. Y.-C. Chen, Q. Chen and X. Fan, *Optica*, 2016, **3**, 809-815.
10. C. P. Dietrich, A. Steude, L. Tropf, M. Schubert, N. M. Kronenberg, K. Ostermann, S. Höfling and M. C. Gather, *Sci. Adv.*, 2016, **2**, e1600666.
11. Y.-C. Chen, Q. Chen and X. Fan, *Lab Chip*, 2016, **16**, 2228-2235.
12. X. Wu, Q. Chen, Y. Sun and X. fan, *Appl. Phys. Lett.*, 2013, **102**, 203706.
13. S. Nizamoglu, M. C. Gather and S. H. Yun, *Adv. Mater.*, 2013, **25**, 5943-5947.
14. J. A. Rivera and J. G. Eden, *Opt. Express*, 2016, **24**, 10858-10868.
15. W. Lee, H. Li, J. D. Suter, K. Reddy, Y. Sun and X. Fan, *Appl. Phys. Lett.*, 2011, **98**, 061103.
16. C. Vannahme, F. Maier-Flaig, U. Lemmer and A. Kristensen, *Lab Chip*, 2013, **13**, 2675-2678.
17. S. Lacey, I. M. White, Y. Sun, S. I. Shopova, J. M. Cupps, P. Zhang and X. Fan, *Opt. Express*, 2007, **15**, 15523-15530.
18. S. Cho, M. Humar, N. Martino and S. H. Yun, *Phys. Rev. Lett.*, 2016, **117**, 193902.
19. Y. Wei, X. Lin, C. Wei, W. Zhang, Y. Yan and Y. S. Zhao, *ACS Nano*, 2017, **11**, 597-602.
20. V. D. Ta, S. Caixeiro, F. M. Fernandes and R. Sapienza, *Adv. Opt. Mater.*, 2017, **5**, 1601022.
21. M. Schubert, K. Volckaert, M. Karl, A. Morton, P. Liehm, G. B. Miles, S. J. Powis and M. C. Gather, *Sci. Rep.*, 2017, **7**, 40877.
22. Y. Choi, H. Jeon and S. Kim, *Lab Chip*, 2015, **15**, 642-645.
23. M. Humar and S. Hyun Yun, *Nat. Photon.*, 2015, **9**, 572-576.
24. H.-J. Moon, Y.-T. Chough, J. B. Kim, K. An, J. Yi and J. Lee, *Appl. Phys. Lett.*, 2000, **76**, 3679-3681.
25. H.-J. Moon, Y.-T. Chough and K. An, *Phys. Rev. Lett.*, 2000, **85**, 3161-3164.
26. M. J. Lohse, S. Nuber and C. Hoffmann, *Pharmacol. Rev.*, 2012, **64**, 299-336.
27. G. B. Kim and Y.-P. Kim, *Theranostics*, 2012, **2**, 127-138.
28. Y. Wang, L. Bao, Z. Liu and D.-W. Pang, *Anal. Chem.*, 2011, **83**, 8130-8137.
29. J. Hohlbein, T. D. Craggs and T. Cordes, *Chem. Soc. Rev.*, 2014, **43**, 1156-1171.

30.   L. M. S. Loura and M. Prieto, *Front. Physiol.*, 2011, **2**, 82.

31.   W. Becker, *J. Microsc.*, 2012, **247**, 119-136.

32.   V. G. Kozlov, V. Bulovic, P. E. Burrows, M. Baldo, V. B. Khalfin, G. Parthasarathy, S. R. Forrest, Y. You and M. E. Thompson, *J. Appl. Phys.*, 1998, **84**, 4096-4108.

33.   R. L. Armstrong, R. G. Pinnick, J. G. Xie and T. E. Ruekgauer, *Opt. Lett.*, 1992, **17**, 943-945.

34.   S. R. I. M. I. Savadatti, N. N. Math, and A. D. Mulla, *J. Chem. Soc. Faraday Trans.*, 1986, **82**, 2417-2422.

35.   C. M. V. C. E. Moeller, and A. H. Adelman, *Appl. Phys. Lett.*, 1971, **18**, 278-280.

36.   Y. Sun, S. I. Shopova, C.-S. Wu, S. Arnold and X. Fan, *Proc. Natl. Acad. Sci.*, 2010, **107**, 16039-16042.

37.   S. I. Shopova, J. M. Cupps, P. Zhang, E. P. Henderson, S. Lacey and X. Fan, *Opt. Express*, 2007, **15**, 12735-12742.

38.   S. I. Shopova, H. Zhu, X. Fan and P. Zhang, *Appl. Phys. Lett.*, 2007, **90**, 221101-221101-221101-221103.

39.   R. P. Bhattacharyya, A. Remenyi, B. J. Yeh and W. A. Lim, *Annu. Rev. Biochem.*, 2006, **75**, 655-680.

40.   B. Geiger, J. P. Spatz and A. D. Bershadsky, *Nat. Rev. Mol. Cell Biol.*, 2009, **10**, 21-33.

41.   S. Sivaramakrishnan and J. A. Spudich, *Proc. Natl. Acad. Sci.*, 2011, **108**, 20467-20472.

42.   N. C. Seeman, *Nature*, 2003, **421**, 427-431.

43.   A. V. Pinheiro, D. Han, W. M. Shih and H. Yan, *Nat. Nanotechnol.*, 2011, **5**, 763-772.

44.   S. J. Tan, M. J. Campolongo, D. Luo and W. Cheng, *Nat. Nanotechnol.*, 2011, **6**, 268-276.

45.   T. Tørring, N. V. Voigt, J. Nangreave, H. Yan and K. V. Gothelf, *Chem. Soc. Rev.*, 2011, **40**, 5636-5646.

46.   N. Y. Wong, H. Xing, L. H. Tan and Y. Lu, *J. Am. Chem. Soc.*, 2013, **135**, 2931–2934.

47.   R. P. Goodman, I. A. T. Schaap, C. F. Tardin, C. M. Erben, R. M. Berry, C. F. Schmidt and A. J. Turberfield, *Science*, 2005, **310**, 1661-1665.

48.   R. P. Goodman, M. Heilemann, S. Doose, C. M. Erben, A. N. Kapanidis and A. J. Turberfield, *Nat. Nanotechnol.*, 2008, **3**, 93-96.

49.   C. Zhang, M. Su, Y. He, Y. Leng, A. E. Ribbe, G. Wang, W. Jiang and C. Mao, *Chem. Commun.*, 2010, **46**, 6792-6794.

50.   H. Pei, N. Lu, Y. Wen, S. Song, Y. Liu, H. Yan and C. Fan, *Adv. Mater.*, 2010, **22**, 4754-4758.

51.   Y. Wen, H. Pei, Y. Shen, J. Xi, M. Lin, N. Lu, X. Shen, J. Li and C. Fan, *Sci. Rep.*, 2012, **2**, 867.

52.   H. Pei, L. Liang, G. Yao, J. Li, Q. Huang and C. Fan, *Angew. Chem. Int. Ed.*, 2012, **51**, 9020-9024.

53.   H. Özhalıcı-Ünal and B. A. Armitage, *ACS Nano*, 2009, **3**, 425-433.

54.   C. M. Erben, R. P. Goodman and A. J. Turberfield, *Angew. Chem. Int. Ed.*, 2006, **45**, 7414-7417.

55.   J. Li, H. Pei, B. Zhu, L. Liang, M. Wei, Y. He, N. Chen, D. Li, Q. Huang and C. Fan, *ACS Nano*, 2011, **5**, 8783-8789.

56.   N. Mitchell, R. Schlapak, M. Kastner, D. Armitage, W. Chrzanowski, J. Riener, P. Hinterdorfer, A. Ebner and S. Howorka, *Angew. Chem. Int. Ed.*, 2009, **48**, 525-527.

57.   A. Kuzyk, R. Schreiber, Z. Fan, G. Pardatscher, E.-M. Roller, A. Högele, F. C. Simmel, A. O. Govorov and T. Liedl, *Nature*, 2012, **483**, 311-314.

58. G. P. Acuna, F. M. Möller, P. Holzmeister, S. Beater, B. Lalkens and P. Tinnefeld, *Science*, 2012, **338**, 506-510.
59. A. J. Mastroianni, S. A. Claridge and A. P. Alivisatos, *J. Am. Chem. Soc.*, 2009, **131**, 8455-8459.
60. W. Yan, L. Xu, C. Xu, W. Ma, H. Kuang, L. Wang and N. A. Kotov, *J. Am. Chem. Soc.*, 2012, **134**, 15114–15121.
61. X. Fan and I. M. White, *Nat. Photon.*, 2011, **5**, 591-597.
62. H. Schmidt and A. R. Hawkins, *Nat. Photon.*, 2011, **5**, 598-604.
63. D. Psaltis, S. R. Quake and C. Yang, *Nature*, 2006, **442**, 381-386.
64. C. Monat, P. Domachuk and B. J. Eggleton, *Nat. Photon.*, 2007, **1**, 106-114.
65. W. Lee and X. Fan, *Anal. Chem.*, 2012, **84**, 9558 - 9563.
66. T. Wienhold, F. Breithaupt, C. Vannahme, M. B. Cristiansen, W. Dorfler, A. Kristensen and T. Mappes, *Lab Chip*, 2012, **12**, 3734-3739.
67. A. E. Siegman, *Lasers*, University Science Books, Sausalito, CA, 1986.
68. S. Lacey, I. M. White, Y. Sun, S. I. Shopova, J. M. Cupps, P. Zhang and X. Fan, *Opt. Express*, 2007, **15**, 15523-15530.
69. H.-J. Moon, Y.-T. Chough and K. An, *Phys. Rev. Lett.*, 2000, **85**, 3161-3164.
70. Z. Li and D. Psaltis, *Microfluid. Nanofluid.*, 2008, **4**, 145-158.
71. M. Kazes, D. Y. Lewis, Y. Ebenstein, T. Mokari and U. Banin, *Adv. Mater.*, 2002, **14**, 317-321.
72. J. Schäfer, J. P. Mondia, R. Sharma, Z. H. Lu, A. S. Susha, A. L. Rogach and L. J. Wang, *Nano Lett.*, 2008, **8**, 1709-1712.
73. Y. Wang, K. S. Leck, V. D. Ta, R. Chen, V. Nalla, Y. Gao, T. He, H. V. Demir and H. Sun, *Adv. Mater.*, 2015, **27**, 169-175.
74. A. Kiraz, Q. Chen and X. Fan, *ASC Photonics*, 2015, **2**, 707-713.
75. D. M. Willard, L. L. Carillo, J. Jung and A. V. Orden, *Nano Lett.*, 2001, **1**, 469-474.
76. S. Wang, N. Mmedova, N. A. Kotov, W. Chen and J. Studer, *Nano Lett.*, 2002, **2**, 817-822.
77. I. L. Medintz, A. R. Clapp, H. Mattoussi, E. R. Goldman, B. Fisher and J. M. Mauro, *Nat. Mater.*, 2003, **2**, 630-638.
78. C.-Y. Zhang, H.-C. Yeh, M. T. Kuroki and T.-H. Wang, *Nat. Mater.*, 2005, **4**, 826-831.
79. A. R. Clapp, I. L. Medintz and H. Mattoussi, *Chem. Phys. Chem.*, 2006, **7**, 47-57.
80. J. Xiao, Y. Wang, Z. Hua, X. Wang, C. Zhang and M. Xiao, *Nat. Commun.*, 2012, **3**, 1170.
81. I. L. Medintz, H. T. Uyeda, E. R. Goldman and H. Mattoussi, *Nat. Mater.*, 2006, **4**, 435-446.
82. R. C. Somers, M. G. Bawendi and D. G. Nocera, *Chem. Soc. Rev.*, 2007, **36**, 579-591.
83. A. Jonas, M. Aas, Y. Karadag, S. Manioglu, S. Anand, D. McGloin, H. Bayraktar and A. Kiraz, *Lab Chip*, 2014, **14**, 3093-3100.
84. M. Aas, Q. Chen, A. Jonas, A. Kiraz and X. Fan, *IEEE J. Sel. Top. Quantum Electron.*, 2016, **22**, 1-15.
85. H. Htoon, J. Hollingsworth, R. Dickerson and V. Klimov, *Phys. Rev. Lett.*, 2003, **91**, 227401.
86. V. I. Klimov, *Annu. Rev. Phys. Chem.*, 2007, **58**, 635-673.
87. Y. S. Park, A. V. Malko, J. Vela, Y. Chen, Y. Ghosh, F. García-Santamaría, J. A. Hollingsworth, V. I. Klimov and H. Htoon, *Phys. Rev. Lett.*, 2011, **106**, 187401.

88. A. M. Dennis, b. D. Mangum, A. Piryatinski, Y.-S. Park, D. C. Hannah, J. L. Casson, D. J. Williams, R. D. Schaller, H. Htoon and J. A. Hollingsworth, *Nano Lett.*, 2012, **12**, 5545-5551.

89. W. K. Bae, Y.-S. Park, J. Lim, D. Lee, L. A. Padilha, H. McDaniel, I. Robel, C. Lee, J. M. Pietryga and V. I. Klimov, *Nat. Commun.*, 2013, **4**, 2661.

90. Y.-S. Park, W. K. Bae, L. A. Padilha, J. M. Pietryga and V. I. Klimov, *Nano Lett.*, 2014, **14**, 396-402.

91. Q. Kou, I. Yesilyurt and Y. Chen, *Appl. Phys. Lett.*, 2006, **88**.

92. B. Helbo, A. Kristensen and A. Menon, *J. Micromech. Microeng.*, 2003, **13**, 307.

93. Z. Li and D. Psaltis, *IEEE J. Sel. Top. Quantum Electron.*, 2007, **13**, 185-193.

94. S. Tyagi and F. R. Kramer, *Nat. Biotech.*, 1996, **14**, 303-308.

95. L. Zhou, L. Wang, R. Palais, R. Pryor and C. T. Wittwer, *Clin. Chem.*, 2005, **51**, 1770.

96. S. Brenner, M. Johnson, J. Bridgham, G. Golda, D. H. Lloyd, D. Johnson, S. Luo, S. McCurdy, M. Foy, M. Ewan, R. Roth, D. George, S. Eletr, G. Albrecht, E. Vermaas, S. R. Williams, K. Moon, T. Burcham, M. Pallas, R. B. DuBridge, J. Kirchner, K. Fearon, J.-i. Mao and K. Corcoran, *Nat. Biotech.*, 2000, **18**, 630-634.

97. M. C. Larson, M. Kondow, T. Kitatani, Y. Yazawa and M. Okai, *Electron. Lett.*, 1997, **33**, 959-960.

98. W. Li, T. Jouhti, C. S. Peng, J. Konttinen, P. Laukkanen, E.-M. Pavelescu, M. Dumitrescu and M. Pessa, *Appl. Phys. Lett.*, 2001, **79**, 3386-3388.

99. V. Bulović, V. G. Kozlov, V. B. Khalfin and S. R. Forrest, *Science*, 1998, **279**, 553.

100. A. Rose, Z. Zhu, C. F. Madigan, T. M. Swager and V. Bulovic, *Nature*, 2005, **434**, 876-879.

101. U. Bog, T. Laue, T. Grossmann, T. Beck, T. Wienhold, B. Richter, M. Hirtz, H. Fuchs, H. Kalt and T. Mappes, *Lab Chip*, 2013, **13**, 2701-2707.

102. A. Boleininger, T. Lake, S. Hami and C. Vallance, *Sensors*, 2010, **10**, 1765 - 1781.

103. Z. Li, Z. Zhang, T. Emery, A. Scherer and D. Psaltis, *Opt. Express*, 2006, **14**, 696-701.

104. M. Schubert, A. Steude, P. Liehm, N. M. Kronenberg, M. Karl, E. C. Campbell, S. J. Powis and M. C. Gather, *Nano Lett.*, 2015, **15**, 5647-5652.

105. S. Nizamoglu, K.-B. Lee, M. C. Gather, K. S. Kim, M. Jeon, S. Kim, M. Humar and S.-H. Yun, *Adv. Opt. Mater.*, 2015, **3**, 1197-1200.

106. M. Humar, M. C. Gather and S.-H. Yun, *Opt. Express*, 2015, **23**, 27865-27879.

107. J. Yuan and P. A. Sims, *Sci. Rep.*, 2016, **6**, 33883.

108. S. M. Schubert, S. R. Walter, M. Manesse and D. R. Walt, *Anal. Chem.*, 2016, **88**, 2952-2957.

109. A. Morimoto, T. Mogami, M. Watanabe, K. Iijima, Y. Akiyama, K. Katayama, T. Futami, N. Yamamoto, T. Sawada, F. Koizumi and Y. Koh, *PLoS ONE*, 2015, **10**, e0130418.

110. A. J. Hughes, D. P. Spelke, Z. Xu, C.-C. Kang, D. V. Schaffer and A. E. Herr, *Nat. Methods*, 2014, **11**, 749-755.

111. P. Zhang, J. Zhang, S. Bian, Z. Chen, Y. Hu, R. Hu, J. Li, Y. Cheng, X. Zhang, Y. Zhou, X. Chen and P. Liu, *Lab Chip*, 2016, **16**, 2996-3006.

112. V. Bernal, N. Carinhas, A. Y. Yokomizo, M. J. T. Carrondo and P. M. Alves, *Biotechnol. Bioeng.*, 2009, **104**, 162-180.

113. S. M. Stocks, *Cytometry*, 2004, **61A**, 189-195.

114. M. Karl, C. P. Dietrich, M. Schubert, I. D. W. Samuel, G. A. Turnbull and M. C. Gather, *J. Phys. D: Appl. Phys.*, 2017, **50**, 084005.

115. M. A. Bandres and J. C. Gutiérrez-Vega, *Opt. Lett.*, 2004, **29**, 144-146.
116. P. Y. Liu, L. K. Chin, W. Ser, H. F. Chen, C. M. Hsieh, C. H. Lee, K. B. Sung, T. C. Ayi, P. H. Yap, B. Liedberg, K. Wang, T. Bourouina and Y. Leprince-Wang, *Lab Chip*, 2016, **16**, 634-644.
117. S. Elmore, *Toxicol. Pathol.*, 2007, **35**, 495-516.
118. Y. H. Kim, S. J. Park, S.-W. Jeon, S. Ju, C.-S. Park, W.-T. Han and B. H. Lee, *Opt. Express*, 2012, **20**, 23744-23754.
119. S. Hong, W. Jung, T. Nazari, S. Song, T. Kim, C. Quan and K. Oh, *Opt. Lett.*, 2017, **42**, 1943-1945.
120. H. Yilmaz, A. Pena-Francesch, R. Shreiner, H. Jung, Z. Belay, M. C. Demirel, S. K. Ozdemir and L. Yang, *ACS Photonics*, 2017, DOI: 10.1021/acsphotonics.7b00310.
121. C. J. Flood, G. Giuliani and H. M. van Driel, *Opt. Lett.*, 1990, **15**, 215-217.
122. U. T. Schwarz, M. A. Bandres and J. C. Gutiérrez-Vega, *Opt. Lett.*, 2004, **29**, 1870-1872.
123. Z. Zhang, Y.-C. Chen, Y.-H. Cheng, Y. Luan and E. Yoon, *Lab Chip*, 2016, **16**, 2504-2512.
124. W. Lee, Q. Chen, X. Fan and D. K. Yoon, *Lab Chip*, 2016, **16**, 4770-4776.
125. J. P. Overington, B. Al-Lazikani and A. L. Hopkins, *Nat. Rev. Drug Discov.*, 2006, **5**, 993-996.
126. D. Filmore, *Mod. Drug Discovery*, 2004, **7**, 24-28.
127. Y.-C. Chen, X. Tan, Q. Sun, Q. Chen, W. Wang and X. Fan, *Nat. Biomed. Eng.*, 2017, DOI: 10.1038/s41551-017-0128-3.